Cellular Functional Architecture of the Human Cone Photoreceptor Mosaic

By

William Scott Tuten

A dissertation submitted in partial satisfaction of the

requirements for the degree of

Doctor of Philosophy

in

Vision Science

in the

Graduate Division

of the

University of California, Berkeley

Committee in charge:

Professor Austin Roorda, Chair
Professor Susana Chung
Professor Gerald Westheimer

Fall 2014

Cellular Functional Architecture of the Human Cone Photoreceptor Mosaic

© 2014

by William Scott Tuten

Abstract

Cellular Functional Architecture of the Human Cone Photoreceptor Mosaic

by

William Scott Tuten

Doctor of Philosophy in Vision Science

University of California, Berkeley

Professor Austin Roorda, Chair

Chromatic and high-acuity aspects of vision are mediated by cone photoreceptors, which sample the image relayed by the eye's optics and transduce it into the neural signals that give rise to perception. Our understanding of how individual cones function has largely been gleaned from *in vitro* electrophysiological preparations, which allow the experimenter to stimulate single receptors while simultaneously recording their outputs. Building upon these findings requires investigating how signals arising from single sensory input neurons are handled downstream by the nervous system, up to and including the perceptual stage. With these goals in mind, the tools to approach these questions *in vivo* must be developed.

The challenges associated with studying the perceptions arising from single sensory receptors are not trivial—doing so requires an ability to visualize and repeatedly stimulate the receptor of interest, which can be difficult when it is situated within a densely packed array of similar cells that is itself contained within a sensory organ. The eye, however, represents a unique case because the receptor layer can be visualized directly through the transparent cornea and lens. The fidelity of this view is diluted only by optical imperfections in the refractive components of the eye. Advances in ocular imaging that have taken place over the past 20 years now make it possible to overcome these imperfections and image individual photoreceptors *in vivo*. The series of experiments described in this document involve the development of methods to overcome these obstacles, the application of this technology to study single-cone-driven perception in healthy subjects, and the translation of these tools to the clinical realm, where cone structure and function were studied with micron-scale resolution in patients with retinal disease.

TABLE OF CONTENTS

LIST OF FIGURES

LIST OF ABBREVIATIONS

AMD	Age-related macular degeneration
AO	Adaptive optics
AOM	Acousto-optic modulator
AOMP	Adaptive optics microperimetry
AOSLO	Adaptive optics scanning laser ophthalmoscope (or ophthalmoscopy)
a.u.	Arbitrary units
BCVA	Best-corrected visual acuity
CCD	Charge coupled device
CHM	Choroideremia
D	Diopters
DAC	Digital-to-analog converter
dB	Decibels
ELM	External limiting membrane
ETDRS	Early Treatment of Diabetic Retinopathy Study
EZ	Ellipsoid Zone
FA	Fluorescein angiography
FH	Family history
FT	Fourier transform
FWHM	Full-width half-maximum
HRZ	Hyporeflective zone
HSWS	Hartmann-Shack wavefront sensor (or sensing)
Hz	Hertz
IR	Infrared
IS	Inner segment
L-/M-/S-	L-, M-, and S-cones, respectively
LC	Light capture
LCA	Longitudinal chromatic aberration
LGN	Lateral geniculate nucleus
LOA	Limits of agreement
MacTel	Macular telangiectasia
MEMS	Micro-electromechanical system
MH	Macular hole
MP1	Nidek microperimeter
MR	Manifest refraction
MTF	Modulation transfer function
OCT	Optical coherence tomographer (or tomography)
OS	Outer segment
OTF	Optical transfer function
PMT	Photomultiplier tube
PRLF	Preferred retinal locus of fixation
PSF	Point spread function
PTF	Phase transfer function

PTOS   Posterior tip of the outer segment
RD   Retinal detachment
ROI   Region of interest
RP   Retinitis pigmentosa
SD   Standard deviation
SD-OCT   Spectral domain optical coherence tomographer (or tomography)
SLD   Superluminescent diode
SLO   Scanning laser ophthalmoscope (or ophthalmoscopy)
STGD   Stargardt disease
TCA   Transverse chromatic aberration

ACKNOWLEDGEMENTS

"Instruction does much, but encouragement everything."

— J. W. von Goethe

There is a lengthy list of people to whom I am indebted for their kindness and generosity over the years. Chief among them is my wife, Amy, who supported my decision to move across the country and pursue my doctoral studies without a moment's hesitation. I cannot imagine accomplishing half of what I've done without her love and encouragement. I am also grateful to my family—my parents, siblings, and grandparents—who instilled in me an appreciation for the value of education, although I am willing to admit that a solid quarter-century as a student is perhaps taking that ideal to the extreme.

My early professional and academic development was shaped by many individuals who deserve gratitude and acknowledgement: Lynn Olzak and Andy Fischer, for kindly providing my first exposures to vision science; Donald Mutti, whose mentorship during my master's studies and exemplary work as a clinician-scientist cemented my decision to pursue a career in optometric research; Karla Zadnik, for encouraging me to head west; Christine Wildsoet, for allowing me to spend a few months in her lab and for demonstrating that finding success as a scientist and being good-natured are not mutually exclusive pursuits.

Lastly, I would like to thank the colleagues and collaborators with whom I have had the opportunity to interact over the past 5-plus years as a member of the Roorda laboratory. Foremost, of course, is Austin Roorda. Austin is a first-rate mentor and a model scientist whom we would all do well to emulate—I suspect I will be benefitting from my association with him for years to come. None of the clinical studies included in this document would have been possible without the efforts our enthusiastic collaborator, Jacque Duncan. I have been privileged to work closely on experiments involving single-cone psychophysics with Wolf Harmening, Lawrence Sincich, and Ramkumar Sabesan, all of whom I consider scientific mentors and, more importantly, friends. I thank Pavan Tiruveedhula for solving virtually all of the technical issues I encountered (or created for myself) without as much as a single roll of the eyes. I would also like to thank the Roorda laboratory members who fostered a happy work environment during my time in Berkeley: Ethan Rossi, Kaccie Li, Johnny Tam, Adam Hickenbotham, Nicole Putnam, Christy Sheehy, Kavitha Ratnam, Ally Boehm, Brandon Lujan, Silvestre Manzanera, David Merino, and Bhavna Antony. Finally, I am indebted to my dissertation committee members, Susana Chung and Gerald Westheimer, for the advice and support they provided as I prepared this document.

CHAPTER 1 – Imaging and Stimulating the Retina with Adaptive Optics Scanning Laser Ophthalmoscopy

1.1 Introduction

1.1.1 Optical Quality of the Eye: a Historical Overview

The optical apparatus of the eye serves an important function: it relays photons emitted by, or reflected from, physical objects in the world onto the retina, which in turn initiates of a cascade of neural events that eventually give rise to visual perception. It can be argued, therefore, that the eye resides at the intersection of the psychological and physical worlds, and its optical fidelity has consequently been the subject of much scientific attention since at least the early 19th century (for a historical overview, see (Westheimer, 2006)).

As a neurosensory organ, the human eye stands testament to the power of evolution. To function properly as an optical device, it must (1) possess refractive components made of transparent, physiologically-viable tissues capable of forming an image, and (2) feature a photo-transductive surface positioned at precisely the right plane to receive the relayed image in crisp focus. In its resting state, the adult eye is equipped with about 60 diopters (D) of refractive power, two-thirds of which is derived from the cornea, with the crystalline lens contributing the remainder. During infancy, the axial length of the eye is around 17 mm, and by age 6 it has increased to its mature size of roughly 22 mm (Larsen, 1971). Considering that an over- or under-growth of the eye on the order of 300 microns during development can result in a clinically meaningful refractive error of ± 1.00 D, it is remarkable that this process results in emmetropia as frequently as it does (Vitale et al., 2008).

Despite the attributes outlined above, it has been recognized for some time that the eye's optics are far from perfect, and that these shortcomings may impact our perceptual experience. Individuals reliant on spectacles or contact lenses for clear vision are familiar with the blur associated with the most common of the eye's optical imperfections: defocus and astigmatism, the so-called low-order aberrations. The former arises from a mismatch of the refractive power and axial length of the eye, while the latter stems from meridional differences in surface curvature of the cornea and lens. The first efforts to correct for low-order aberrations date back at least 2000 years, involving the use of transparent minerals or glass to shift the focal point of the eye (Rubin, 1986). By the 15th century, Florentine spectacle merchants were flourishing as they exported spherical corrective lenses across Europe (Ilardi, 2004). A concomitant understanding of the optical workings of the eye, however, remained beyond reach until the early 17th century, when Kepler (and later Scheiner) demonstrated that the retinal image is inverted (Williams and Porter, 2006). Around 200 years later, Thomas Young gave the first thorough account of astigmatism (Young, 1801), and the development of sphero-cylindrical lenses by Sir George Biddell Airy shortly thereafter finally enabled its correction. Thus, the practice of prescribing refractive correction by specifying three parameters—sphere, cylinder, and axis—was born, and remains essentially unchanged to this day.

While standard refractive corrections have been successful in compensating for low-order aberrations, it has been appreciated for some time that the optical state of the conventionally-corrected eye is less than perfect. In his seminal writings on physiological optics, Hermann von Helmholtz noticed that, when viewing a point source, asymmetric irregularities in the observed image were evident (Helmholtz, 1924). His account was perhaps the first description of what we have come to term high-order monochromatic aberrations:

> *"The monochromatic aberrations in the optical system of the eye are not, like the spherical aberration of glass lenses, symmetrical about an axis. They are much more unsymmetrical and of a kind that is not permissible in well constructed optical instruments…Suppose the object is a very small luminous point (for example, a pinhole in a piece of opaque black paper illuminated from behind), which is situated rather farther from the eye than the greatest distance of accommodation; so that its image on the retina will be indistinct. In place of the bright point, what is seen is not a circular spot, as in the case of a telescope out of focus, but a star-shaped pattern with from four to eight irregular points or rays, which is usually different in the two eyes, and different also for different individuals."*

—— Helmholtz, 1924 (p. 189)

Considering the form of the image on the retina is of critical importance because, for those interested in elucidating the neural underpinnings of vision, a common tactic is to present a real-world stimulus that can be well characterized in physical terms (e.g. a spot of light of a given size, wavelength, and irradiance) and measure the response—either physiological or perceptual—it evokes. The stimulus-response relationship is then used to infer properties of the visual system; however, one must take caution at this stage to distinguish between objects in the physical world (so-called *distal stimuli*) and the corresponding images of these objects made available for processing by the retina (*proximal stimuli*). Without insight into the nature of how the former is transformed into the latter, one runs the risk of mistakenly assigning a neural or perceptual basis to phenomena whose origins may be purely optical.

With this in mind, investigations into the optical quality of the eye—and, by extension, the nature of the retinal image itself—become necessary. A reasonable first approach to solving this problem is to adopt psychophysics as a tool for validating estimates of retinal light spread. In the first half of the 20th century, this process generally involved probing spatial vision with some fine feature, such as high-contrast gratings (Shlaer, 1937) or extremely narrow lines (Hecht and Mintz, 1939), and attempting to reconcile performance on a given task (e.g. alignment or detection) with a model of light spread based on diffraction theory and known estimates of chromatic aberration (Hartridge, 1918). Unfortunately, such efforts necessarily require assumptions about the retina's detecting and/or resolving capacity, otherwise the problem would, in essence, contain two free parameters and not yield a unique solution. Since our understanding of retinal processing remains incomplete, it is difficult to imagine these early psychophysical approaches could converge on an estimate of retinal light spread that was not

potentially conflated with some neurosensory aspect of vision. Instead, a preferred approach to this problem would be one in which the optical component of the visual system is divorced from its neural and perceptual counterparts.

The next major advance on this front grew out of linear systems theory, which rose to prominence after the Second World War. Any system can be considered linear if it obeys the principles of superposition and shift-invariance; in simple terms, its response to any complex object can be predicted if the response to a fundamental object, known as an "impulse", is known. The performance of a linear optical system can therefore be fully characterized by assessing its ability to image an infinitesimally small spot of light. This image is termed the point spread function (PSF) and has a striking conceptual resonance with the subjective sketches of point images presented by Helmholtz in his treatise (Helmholtz, 1924). The PSF, which exists in the spatial domain, has an equivalent representation in the Fourier domain—the optical transfer function, itself made up of amplitude (modulation transfer function, or MTF) and phase components (phase transfer function, or PTF). A schematic of the relationship between these concepts is presented in Figure 1.1.
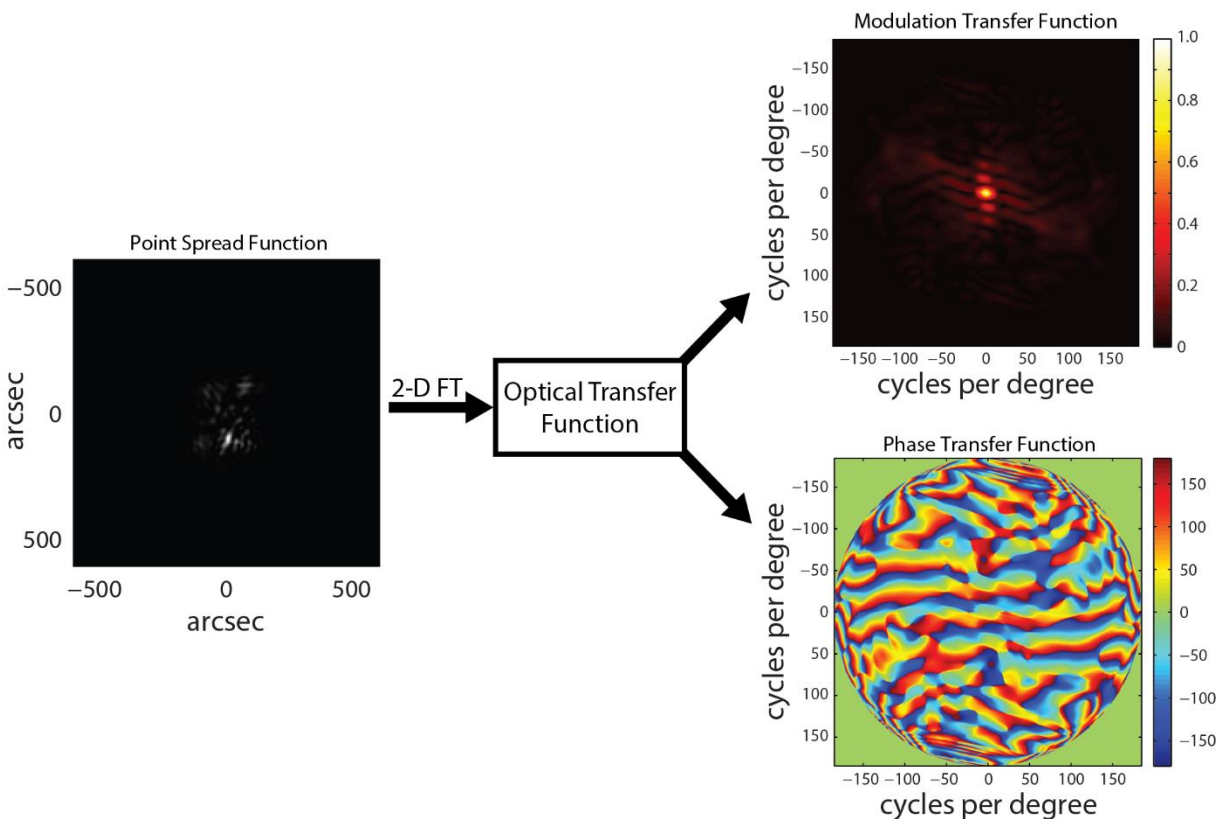
Figure 1.1| Representing the point spread function (PSF) in the Fourier domain. The PSF (left panel) belongs to the author of this report and was obtained over a 5.6 mm pupil using a Hartmann-Shack wavefront sensor; low-order terms (defocus and astigmatism) have been set to zero to better visualize the high-order aberrations. The optical transfer function (OTF) was computed from the 2-dimensional Fourier transform (FT) of the PSF. The amplitude component of the OTF, the modulation transfer function (upper right panel), conveys how contrast is relayed by an optical system as a function of spatial frequency; the phase transfer function is plotted in the lower panel.

While the Fourier framework represented a paradigm shift in how vision scientists considered the optical performance of the eye, measuring the point spread function objectively remained fraught with technical hurdles. At the time, obtaining direct measurements of the reflected image of a point source emerging from the eye would have been difficult owing to the relatively low reflectance of the fundus (between 0.1% and 10%, depending on wavelength (Van Norren and Tiemeijer, 1986)) and the poor sensitivity of photographic film. For man-made optical systems, a common solution was to measure line-spread functions, which boosted signal-to-noise ratios and permitted mathematical recovery of the PSF, provided one adopted the assumption that the system was radially symmetric (Marchand, 1964). The first direct measures of line spread functions were collected in the living eye in 1955 by Flamant, who acquired photographs of slits projected onto the retina through an ophthalmoscope and extracted line spread functions by deconvolution of the captured double-pass images (Flamant, 1955). The line spread approach to characterizing the optical quality of the eye was further refined in later studies employing more sophisticated detection techniques (Krauskopf, 1962; Westheimer and Campbell, 1962; Campbell and Gubisch, 1966; Gubisch, 1967), and the modulation transfer functions they yielded agreed reasonably well with those estimated by comparing conventional contrast sensitivity functions to those measured with laser-generated interference fringes, which are not subject to degradation by the optical imperfections of the eye (Campbell and Green, 1965).

Although the line spread estimates that emerged from the work of the 1950s and 1960s afforded a clearer picture of the overall optical quality of the eye, their primary limitation was that the optical transfer functions they produced were necessarily unidirectional, unable to convey any radial asymmetries in the wave aberration of the eye (van den Brink, 1962). In the subsequent decades, the quest for a more complete account of the ocular high-order monochromatic aberrations led to the development of new methods for capturing the eye's two-dimensional wavefront, including a substantially improved version of Tscherning's aberroscope (Howland and Howland, 1977; Walsh et al., 1984), psychophysical approaches relying on alignment of stimuli entering through various parts of the pupil (Campbell et al., 1990; Webb et al., 1992; He et al., 1998), and objective laser ray tracing across the pupil (Navarro et al., 1998). While all of these techniques permitted measurement of local deviations across the entrance pupil of the eye, each had their disadvantages: the psychophysical variants were relatively labor-intensive and susceptible to subject error, and their objective counterparts often suffered technical shortcomings that limited their sensitivity and accuracy (Yoon, 2006).

1.1.2 Optical Quality of the Eye: Current Measurement and Correction Techniques

The current state-of-the-art in ophthalmic wavefront measurement and correction has its origins in astronomy. Upon considering the well-known problem that images of stars collected from ground-based telescopes are diluted by random turbulences in the earth's atmosphere, Babcock had the prescience to make the following observation:

"If we had a means of continually measuring the deviation of rays from all parts of the mirror, and of amplifying and feeding back this information so as to correct locally the figure of the mirror in response to the schlieren pattern, we could expect to compensate both for seeing and for any inherent imperfections of optical figure."

— Babcock, 1953

In a single sentence, the complete conceptual framework for adaptive optics was laid out (Babcock, 1953). The principles of adaptive optics are relatively straightforward—the idea is to devise some means of measuring the wavefront passing through an optical system and then use this information to drive a compensatory element placed elsewhere in the path. With regard to the former, the first breakthrough occurred when Shack and Platt modified Hartmann's method of using an aperture grid to sub-sample the deviations in the wavefront by instead inserting an array of tiny lenses, which generated a pattern of focused spots on a screen positioned at their focal point (Shack and Platt, 1971). A completely flat wavefront imaged through this lenslet array would yield a perfectly rectilinear array of spots, each located along the optic axis of the lens through which it passed. By contrast, an aberrated beam would result in deviations from this expected pattern, with the magnitude of each shift proportional to the local slope of the imperfect wavefront. The first implementation of Hartmann-Shack wavefront sensing (HSWS) in the human eye was demonstrated by Liang and colleagues (Liang et al., 1994). Aided by a science-grade charge coupled device (CCD), their method enabled a fast and reliable assessment of the eye's optical quality, and HSWS was used in subsequent studies at the University of Rochester to provide the most complete structural and temporal characterization of the wave aberration in the normal eye (Liang and Williams, 1997; Hofer et al., 2001; Porter et al., 2001).

The second necessary component for a functioning adaptive optics system is an optical element capable of compensating for high-order aberrations. A deformable mirror, which adopts a shape that cancels the phase errors of the aberrated wavefront, is an intuitive choice to fulfill this requirement, although other methods have been proposed, including liquid crystal spatial light modulation (Vargas-Martin et al., 1998) and custom phase-correcting plates (Burns et al., 2002). The first successful implementation of a deformable mirror in astronomy took place in 1977, when Hardy and colleagues used wavefront error measures from a shearing interferometer to drive a 21-zone piezoelectric mirror in closed-loop (Hardy et al., 1977). In vision, open-loop correction of low-order aberrations—defocus and astigmatism—led to modest gains in the resolution of a laser tomographic scanner (Dreher et al., 1989), but nearly another decade passed before the first truly closed-loop AO system for the eye was demonstrated in David Williams' lab at the University of Rochester (Liang and Williams, 1997; Liang et al., 1997). When integrated into a flood-illuminated ophthalmoscope, adaptive optics enabled Williams and colleagues to take advantage of the larger numerical aperture offered by larger pupils, resulting in the first reliable images of the cone photoreceptor mosaic and marked improvements in visual acuity and contrast sensitivity to stimuli projected along the same optical path (Liang et al., 1997; Roorda and Williams, 1999, 2002; Yoon and Williams, 2002).

5

1.1.3   The Development of Adaptive Optics Scanning Laser Ophthalmoscopy

While early-generation adaptive optics ophthalmoscopes offered the first views of the *in vivo* photoreceptor mosaic, their capacity for probing many structural and functional aspects of vision remained somewhat limited. On the structural side, low frame rates of CCDs (<10 Hz) available at the time impeded the study of dynamic visual processes, such as photopigment bleaching and retinal hemodynamics; only recently have newer-generation, high-speed CCDs been incorporated to overcome these problems (Rha et al., 2006; Bedggood and Metha, 2012a, b, 2013). With regard to function, the ability to correct high-order aberrations with adaptive optics armed the first flood-based systems with the resolution that, in theory, made possible the stimulation of individual cones; however, an inability to measure and compensate for ever-present fixational eye movements, as well as to correct for the effects of chromatic dispersion, meant that the earliest attempts at AO-driven single-cone psychophysics were unable to target specific retinal loci, instead relying on collecting data across thousands of trials and using statistical inference to link psychophysical performance to the imaged retinal structure (Hofer et al., 2005a; Makous et al., 2006).

These limitations served as motivation for the incorporation of adaptive optics into another imaging modality: the scanning laser ophthalmoscope (SLO). The SLO was invented in 1980 by Robert Webb, and its core principles are shared with those of the scanning laser microscope, in which a focused imaging beam is scanned across a sample in a raster pattern, with the returning light sensed continuously by a photon detector whose output is used to generate an image pixel by pixel at video rates (Webb et al., 1980). Placing a confocal pinhole immediately before the detector in plane conjugate with the retina allows out-of-focus light to be rejected, further improving contrast and axial resolution (Webb et al., 1987). The clinical applications of SLO were recognized almost immediately, when it was suggested that the imaging raster could be modulated directly to generate stimuli which could be used to measure visual acuity and perimetric sensitivity at retinal locations encoded directly in the SLO images (Mainster et al., 1982).

A critical feature of any SLO is that the eye acts as the objective, serving to focus the scanned beam onto the retina. Because of this, the monochromatic aberrations of the eye set an upper limit to the resolution any SLO can achieve, no matter how well it is designed. Seeking to harness the full potential of the SLO modality, Roorda and colleagues were the first to demonstrate an SLO equipped with adaptive optics (Roorda et al., 2002). The initial adaptive optics scanning laser ophthalmoscope (AOSLO) enabled the compensation of the eye's high-order monochromatic aberrations via a 37-actuator deformable mirror, thereby minimizing the size the imaging spot delivered into, and emerging from, the eye. A better-focused imaging beam in turn allowed better utilization of a small confocal pinhole (50-80 μm), resulting in an *en face* imaging system which boasted unmatched lateral and axial resolutions of 1.9 and 33 microns, respectively (Zhang and Roorda, 2006; Roorda, 2010). Subsequent improvements on the initial incarnation of AOSLO included incorporating newer-generation deformable mirrors (Zhang et al., 2006), adding multiple imaging and stimulation wavelengths (Grieve et al., 2006), and optimizing system design to permit resolution of the smallest cells in the photoreceptor

layer, foveal cones and rods (Dubra and Sulai, 2011; Dubra et al., 2011; Merino et al., 2011). Since its inception, AOSLO has come into widespread use as a tool to study photoreceptor structure directly in a variety of outer retinal diseases (Wolfing et al., 2006; Duncan et al., 2007; Roorda et al., 2007; Carroll et al., 2010; Duncan et al., 2011b; Duncan et al., 2011a; Talcott et al., 2011; Carroll et al., 2013), and has been used as a psychophysical apparatus capable of correlating visual function directly with retinal structure (Rossi et al., 2007; Rossi and Roorda, 2010; Tuten et al., 2012; Harmening et al., 2014). The specifics of using AOSLO for retinal imaging and visual psychophysics are described in the next section of this chapter.

1.2 Methods

1.2.1 High-resolution Retinal Imaging with AOSLO

A schematic layout of a multi-wavelength AOSLO is shown in Figure 1.2. In the first wave of experiments reported in this document (see Chapter 4), the imaging source was an 840 nm broadband superluminescent diode (SLD; Superlum, Carrigtwohill, Ireland); in subsequent experiments (Chapters 2 and 3), infrared light filtered from a broadband supercontinuum light source (SuperK Extreme, NKT Photonics A/S, Birkerød, Denmark) was used in its place. In either case, an image is collected by scanning a focused infrared spot across the retina in a raster pattern using an analog-driven resonant scanner (Electro-Optics Products Corp., Flushing Meadows, NY) in combination with a galvanometric scanner (Cambridge Technology Inc., Lexington, MA). In the studies described in this document, raster scanning amplitudes were set so that AOSLO images were square, spanning anywhere from 1.0° (≈ 290 µm) to 2.1° (≈ 610 µm) of visual angle. The light emerging from the eye is descanned by the scanning elements as it returns along the path of the beam, and the ocular monochromatic aberrations encoded therein are monitored with a custom-built Hartmann-Shack wavefront sensor and corrected dynamically with a 140 actuator, 5.5 µm stroke MEMS deformable mirror (Boston Micromachines, Cambridge, MA, USA). Because the aberrometry beacon is scanned across the imaging field and the wavefront sensor samples at a maximum rate of 24 Hz, the measured wavefront represents a spatio-temporal average of the error for that patch of retina.

A photomultiplier tube (PMT; Hamamatsu, Japan) records the intensity of the reflected IR light. A confocal pinhole, placed in a plane conjugate to the photoreceptor layer, resides in front of the PMT to reject out-of-focus light. Pixel location is assigned using positional information from the scanning mirrors, allowing high resolution retinal videos to be reconstructed over time by a frame grabber at a frame rate of 30 Hz. Each frame comprises 512 by 512 pixels, which are digitized at rate of 20 MHz (pixel clock: 50 nanoseconds). Thus, for a 0.60° raster size, the average individual pixel corresponds to 4.21 arcsec (0.35 microns); for a 2.1° raster, a single pixel subtends 14.8 arcsec (1.23 microns; on the order of a foveal cone diameter (Curcio et al., 1990)) of visual angle.

7
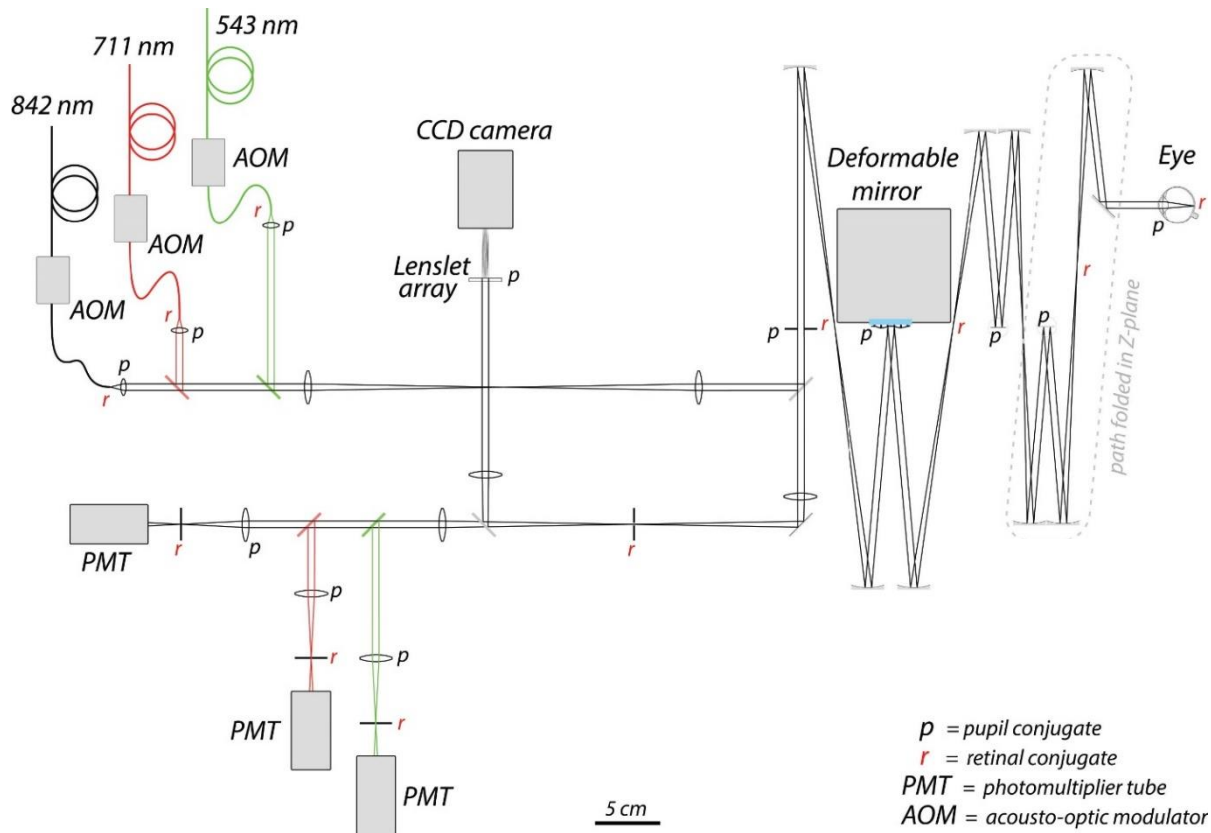
Figure 1.2| Schematic of the multi-wavelength AOSLO used for these studies. (Figure courtesy of Lawrence C. Sincich, University of Alabama at Birmingham.) Three independent stimulation channels are combined and aligned to travel coincident along the common optical path of the system (black lines), and light emerging from the eye can be separated and collected in three independent, wavelength-matched imaging channels.

1.2.2 Stimulus Calibration

The test stimulus is generated using either a second SLD (Chapter 4; λ = 680 nm) or fiber-coupled light filtered from the supercontinuum source (Chapters 2 and 3). In either case, the stimulus source is introduced into the light delivery arm of the AOSLO and is aligned to travel coincident to the imaging beam along the main optical path of the system. Because an infrared light source is used for wavefront sensing and correction, the vergence of the stimulus light source as it enters the system must be adjusted to compensate for the longitudinal chromatic aberration (LCA) of the eye, which population data suggests is relatively consistent between individuals (Atchison and Smith, 2005). The fidelity of LCA correction is confirmed by imaging the photoreceptor layer simultaneously with the stimulus and infrared light; when LCA is properly corrected, the photoreceptor mosaic is in sharp focus in both images. The ability to Image in the stimulus channel is also an important step for measuring and compensating for the effects of transverse chromatic aberration (TCA), the details of which are described in Section 1.2.4 of this chapter.

The timing and intensity of the stimulus light source is controlled by an analog-driven high-speed acousto-optic modulator (AOM; Brimrose Corp, Baltimore, MD, USA), allowing custom stimulus patterns to be presented to the retina in a pixel-by-pixel fashion. The AOM operates by diffracting the incoming light into multiple orders, with the magnitude of the diffraction depending on the voltage with which it is driven. When the AOM receives a maximum voltage, the first-order deflection is aligned such that light coupling into the AOM output fiber is maximal, thereby delivering the most light into the optical path; when lower voltages are used to drive the AOM, the amount of light entering the system decreases. The voltage-response curve of the AOM used to control the stimulus luminance is non-linear. To generate a look-up table, a linear set of voltages from a 14-bit digital-to-analog converter (DAC) is used to drive the AOM, and the radiant flux at the pupil plane is measured using an optical power meter (1830-C, Newport Corporation, Irvine, CA) at each step (Figure 1.3A). While the DAC putatively offers 14-bit (= 16,384 levels) modulation, the linearization process restricts this operational range; for the studies described in this document, the stimulus intensity was modulated over a range of 10^3 linearized steps, equivalent to a 30 dB range of modulation.

There are two important consequences to using an AOM to modulate our stimulus. The first is that some light will always scatter into the first-order direction, even when no voltage is sent to the AOM. The resulting leak must be measured to determine its contribution to the luminance of the raster, and its unavoidable presence renders truly dark-adapted psychophysics with AOSLO impossible. Secondly, because the stimulus is generated pixel-by-pixel by the scanned laser, the actual amount of time the retina is exposed to the stimulus beam is a fraction of the nominal stimulus duration. The true stimulus duration is the sum of the number of pixels comprising the stimulus multiplied by the product of the number of frames over which the stimulus is presented and the time attributed to each pixel. Although the subject perceives the stimulus as continuous, this fact is also considered when calculating retinal illuminance.

The last factor that must be taken into account when calibrating an AOSLO stimulus arises from the nonlinear scanning geometry of the resonant scanner. Because each image pixel represents the light collected over a fixed 50 nanosecond window, the retinal size of an image pixel depends on velocity of the scanning mirror during that period. In the case of the high-speed resonant scanner, its highest and lowest scan velocities are at the center and edges of the raster, respectively. Thus, the edges of the imaging field (where less retina is spanned during a pixel) appear stretched while its center appears relatively minimized (Figure 1.3B). A square calibration grid placed at the retinal plane of a model eye can be used to measure these field distortions, and a look-up table can be generated that enables the "de-sinusoiding" of the unprocessed images, thereby rendering them square (Poonja et al., 2005). A complication arises, however, during psychophysical tasks where stimuli of prescribed angular subtense may be delivered anywhere within the raster, as is the case when targeted locations on an always moving retina are selected for testing (see next section). To maintain a fixed angular size, these stimuli must be pre-distorted depending on where they will be delivered within the raster. This is accomplished by adjusting the number of stimulus pixels (i.e., the duration of the stimulus) along the fast-scan dimension. Moreover, for tasks where stimulus luminance is also important

(e.g., increment thresholds), the subtle timing manipulations that afford a proper spatial rendering of the stimulus require a commensurate adjustment of stimulus intensity to ensure that the number of photons delivered per stimulus remains as prescribed (Figure 1.3C).
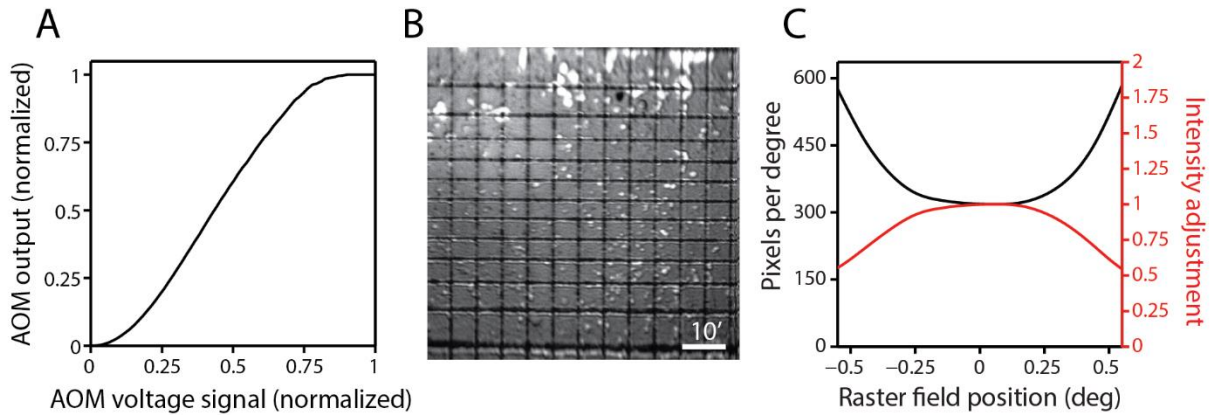
Figure 1.3| Stimulus calibration for AOSLO-based psychophysics. **A)** AOM voltage-response function. **B)** AOSLO scanning distortions. Each square in the calibration grid subtends 0.10 degrees. The variable speed of the sinusoidal vertical scanner causes distortions along its scan path, unlike the linear horizontal scanner**. C)** Adjustments required to present stimuli of fixed angular size and intensity across the raster field. The black line shows image scaling, in pixels per degree, across the vertical dimension of the image in **B**; when considered against the right-side (red) scale, the black line also represents the relative timing adjustments (i.e., number of pixels) required to render stimuli of fixed angular subtense, as described in the text. The red line indicates relative intensity adjustments required to offset the timing manipulations needed to maintain angular fidelity.

1.2.3   Real-time Eye Tracking and Targeted Stimulus Delivery

The eye is always moving, even during periods of concentrated fixation, and these excursions occur on a scale that generally exceeds that of individual photoreceptors. The biological imperatives for fixational eye movements are numerous, including directing our attention toward objects of interest, permitting the inspection of fine detail, and preventing the fading induced by rapid neural adaptation (for an overview, see (Martinez-Conde et al., 2004)). Nevertheless, the peripatetic quality of the eye poses a significant challenge for the psychophysicist attempting to link visual function to retinal structure at the scale of the individual receptor.

A distinct advantage of AOSLO over other adaptive optics stimulation systems is its capacity to track retinal motion with high speed and fidelity. Because AOSLO images are collected via raster scanning at video rates, the movement of the retina can be retrieved by examining the shifts, compressions, expansions, and other distortions of image structure that occur both within an individual frame as well as from one frame to the next (Stevenson and Roorda, 2005). This is achieved by generating a reference frame to which subsequent image information can be registered. Since AOSLO image data is sensed and assembled continuously (i.e., pixel-by-

pixel), the temporal resolution of eye tracking may exceed the nominal frame rate by cross-correlating subdivided blocks of image data (i.e. strips) to the reference frame as they stream in, rather than waiting for the entire frame to be assembled before applying the registration algorithm. The AOSLO eye tracking approach was first applied to off-line analyses (Stevenson and Roorda, 2005; Vogel et al., 2006), and subsequent algorithmic and hardware improvements enabled its online implementation in "real-time" (Arathorn et al., 2007; Yang et al., 2010).

High-speed retinal eye tracking with AOSLO serves two purposes. First, it generates a motion-corrected retinal video from which simple averaging across frames produces retinal images with improved signal-to-noise ratios. Second, the eye tracking algorithm output can be used to deliver stimuli to selected retinal loci. The accuracy of this process depends on a number of factors, including image quality, imaging field size, the magnitude and frequency of fixational eye movements, and the short delay associated with arming the AOM to deliver the stimulus. Nonetheless, adaptive optics-corrected stimuli can be delivered to a normally-fixating eye with a precision as small as 0.15 arcmin (Arathorn et al., 2007; Yang et al., 2010), about half the diameter of a foveal cone. It is worth noting here that although eye movements occurring during the acquisition of a particular reference frame will lead to contaminated eye traces and a distorted motion-corrected video, these artifacts do not affect the accuracy or precision of the stimulus delivery approach described in this document. Finally, because pixel position and time are coupled in raster-based imaging, a white digital cross corresponding to the center of the stimulus can be written onto the video frame at the pixel location corresponding to the moment in time when the AOM was triggered to deliver the stimulus, resulting in an unambiguous record of where the stimulus was delivered on the retina, the effects of transverse chromatic aberration notwithstanding (see next section).

1.2.4   Measurement and Correction of Transverse Chromatic Aberration

Combining high-order monochromatic aberration correction with high-speed retinal tracking enables diffraction-limited stimuli to be delivered to the retina with single-cone precision using AOSLO. The final obstacle to developing a system capable of reliably and repeatedly stimulating single receptors in the retina is the chromatic aberration of the eye. As described in the previous section, targets selected for stimulation are imaged and tracked in the infrared imaging channel. However, it is often desirable for psychophysical experiments to probe the retina with shorter, more visible wavelengths. Doing so introduces experimental uncertainty because, even if the imaging and stimulation beams are perfectly aligned as they enter the eye, dispersion in the ocular media with cause them to deviate on their journey to the retina with a magnitude exceeding the size of a single cone (Atchison and Smith, 2005).

Methods for measuring and compensating for chromatic aberrations with AOSLO have been reported previously by our group (Harmening et al., 2012). By collecting independent images in the infrared and stimulation channels, the relative shift in the two beams can be computed by cross-correlating the retinal structure contained in each image. Compensating for TCA involves accounting for this relative shift by adjusting the timing of delivery between the two channels. TCA measurement can be validated in the fovea by comparing image-based values with those

produced from a hyperacute, psychophysical alignment task; objective and subjective measures of TCA collected concurrently show good agreement (Harmening et al., 2012). Validation can also be achieved objectively by delivering a TCA-corrected stimulus of sufficient intensity to obtain simultaneous infrared and stimulus channel images—if TCA is properly accounted for, the structures imaged by the visible stimulus will align with those found around the retinal location selected for tracking in the infrared image (Figure 1.4).
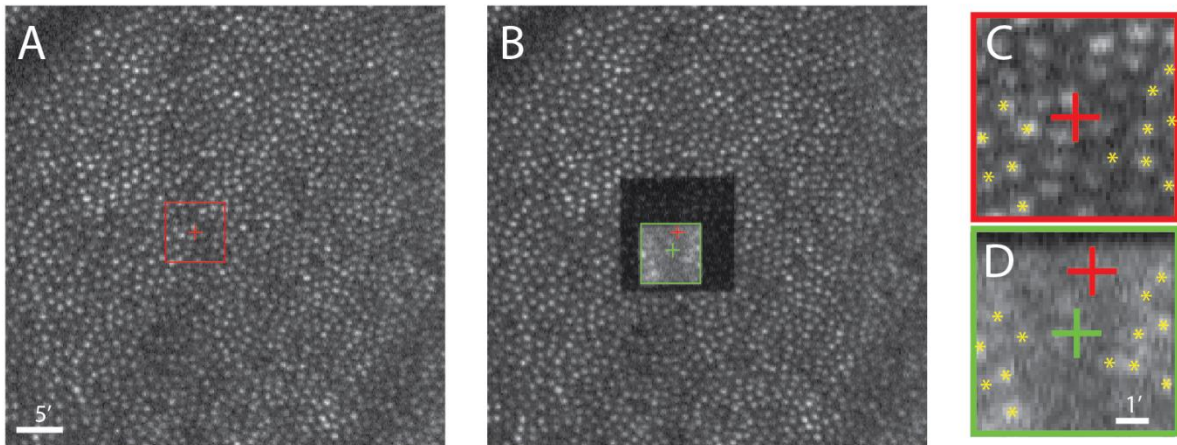
Figure 1.4| Objective validation of TCA measurement and correction. **A)** Infrared imaging frame with the retinal target marked by the red cross. **B)** Registered image during which a TCA-corrected stimulus is delivered. The stimulus is centered on the green cross, and the offset from red corresponds to the timing adjustment applied to correct for TCA. The intensity of the stimulus was sufficient to yield an image in the stimulus channel; the infrared imaging beam was switched off in the center of the frame to enhance the visibility of this image. **C, D)** Comparison of the retinal structure sampled by the infrared (**C**) and stimulus (**D**) beams shows good cone-to-cone alignment (yellow asterisks), despite the disparity in image quality between the two channels.

1.3   Summary

Over the past 200 years, vision scientists have endeavored to characterize the optical quality of the eye and understand how it may serve to shape visual perception. The advent of techniques to assess the complex aberration structure of the eye has led to the development of methods—adaptive optics—that permit its correction. The result is a new generation of ophthalmoscopes that provide unique and unprecedented views into the living eye—glimpses in which individual cells can be resolved. Engineering advances in eye tracking and stimulus delivery allow researchers to harness the improved resolution offered by adaptive optics, making it possible to study vision one cell at a time. The methods described in this chapter are the result of 20 years of hard-earned progress in adaptive optics ophthalmoscopy, and Chapters 2 and 3 will describe our efforts to apply these tools to study percepts elicited by single-cone stimulation. The final two chapters cover the translation of this technology to the clinical setting, where the relationship between retinal structure and function was studied on the cellular scale in patients with a variety of outer retinal diseases, including retinitis pigmentosa, age-related macular degeneration, and macular telangiectasia.

CHAPTER 2 – Revealing a Microscopic Sensitivity Gradient in the Parafoveal Cone Mosaic

2.1 Abstract

In humans, experimental access to single sensory receptors is difficult to achieve, yet it is crucial for learning how the signals arising from each receptor are transformed into perception. By combining adaptive optics microstimulation with high-speed eye tracking, it is shown that photopic retinal function can be probed at the level of the individual cone photoreceptor in living eyes. Classical psychometric functions were obtained from cone-sized microstimuli targeted to single photoreceptors. Revealed psychophysically, the cone mosaic manifests a variable sensitivity to light across its surface that accords with a simple model of cone light capture. Because this microscopic grain of vision can be detected on the perceptual level, it confirms the expectation that parafoveal photoreceptors are sensorially individualized *in vivo*. These results provide the first empirical evidence that the repeated stimulation of single cones is possible with adaptive optics, despite the obstacles posed by optical aberrations, scatter introduced by ocular tissues, and incessant fixational eye movements.

2.2 Introduction

Every sensory system has evolved tissue containing an array of specialized neurons to detect and transduce particular physical stimuli. Much of our knowledge about how each type of sensory neuron works has been learned in dissected preparations, which offer precise control over experimental conditions. To understand the next important step—how the signals that arise from single sensory neurons are handled downstream by the nervous system—an *in vivo* approach is unavoidable. The challenge here is that stimulation of individual neurons is difficult when they sit within an array of similar receptors, with the array itself hidden inside a sensory organ. The eye offers one exception to this situation, with the cornea and lens affording a view of the retina that is only obscured by imperfections in the optics of the cornea and crystalline lens. Recent advances in ocular imaging now make it possible to overcome these imperfections and image individual photoreceptors in the living retina (Williams, 2011). We have taken advantage of this unique access to directly probe photopic vision at the scale of its elementary input cell, the cone photoreceptor.

In humans, photopic vision begins with the roughly 5 million cone photoreceptors that line the back of the retina (Curcio et al., 1990). Understanding how perception is mediated by any one of these cones is hampered primarily by the eye's aberrations (Liang et al., 1997), and secondarily by fixational eye motion that constantly translates any visual stimulus over many cones (Rolfs, 2009). Nonetheless, key insights about single cone function have been learned via techniques that bypass the optics of the eye. For instance, using interference fringes, investigators have found that cones appear to integrate light over a Gaussian aperture that is smaller than a cone diameter (MacLeod et al., 1992; Chen et al., 1993). These psychophysical findings are drawn from stimulation of large patches of retina, pooling signals from hundreds of cones. Thus it remains unclear if perception is ultimately constrained by the light capturing properties of single cones, by downstream retinal circuitry that pools signals, or both.

Here we use an adaptive optics scanning laser ophthalmoscope (AOSLO) that allows simultaneous retinal imaging and psychophysics to be conducted with an optical resolution approaching the diffraction limit (Roorda et al., 2002; Yang et al., 2010). Combined with real-time retinal tracking to compensate for eye motion (Yang et al., 2010), we aimed to confine light delivery to individual cones in order to assess the contribution of single photoreceptors to visual perception. If the light collecting aperture of an individual cone is well modeled by a two-dimensional Gaussian function, then stimuli should be most easily seen when delivered to the cone's center, and less so when displaced from the center. Physiological support for this idea has already been found in primate retinal ganglion cells (Field et al., 2010; Li et al., 2014) and in neurons in the lateral geniculate nucleus (Sincich et al., 2009), where neural responses peak when stimuli land on the center of a cone. Our findings suggest that such micron-scale positional sensitivity is indeed preserved up to the perceptual level. With this psychophysical approach to studying single cone function, the neural underpinnings of vision can now be probed at the elementary level of the photoreceptor.

2.3   Methods

2.3.1   Adaptive Optics Scanning Laser Ophthalmoscope Imaging and Stimulation

We used a multi-wavelength adaptive optics scanning laser ophthalmoscope (AOSLO) for imaging the cone mosaic (Roorda et al., 2002; Grieve et al., 2006). The details of imaging and conducting psychophysics with an AOSLO have been described elsewhere (Rossi et al., 2007; Rossi and Roorda, 2010; Tuten et al., 2012). The light source was a super-continuum laser (SuperK Extreme, NKT Photonics A/S, Birkerød, Denmark) whose output was band pass filtered to provide an infrared (IR) imaging wavelength of 842±25 nm, and a visible green stimulation wavelength of 543±11 nm that minimized the sensitivity difference between long- and medium-wavelength sensitive cones (L and M, respectively). For imaging, a focused spot from the infrared beam was raster scanned across the retina, and the high-order aberrations encoded in the beam emerging from the eye were measured with a Hartmann-Shack wavefront sensor. The wavefront error of the eye was computed and used to drive a 144-actuator, 5.5 µm stroke deformable MEMS mirror (Boston Micromachines Corp, Cambridge, MA) into a compensatory shape which corrected the wavefront on its way into, and out of, the eye. The returning light was sensed continuously by a photomultiplier tube (PMT) located behind a confocal pinhole conjugate with the retina. The voltage output of the PMT combined with positional signals from the scanning mirrors was used to render a 512 × 512 pixel imaging video at 30 frames per second.

Independent 10-bit modulation of the imaging and stimulus channels was achieved by passing them through dedicated acousto-optic modulators (AOM) capable of operating at up to 50 MHz prior to their entry into the scanning and corrective portions of the optical path. High-speed switching allows custom adaptive optics-corrected stimuli to be delivered to the retina—pixel by pixel—in correspondence with the acquired image. Stimulus delivery to selectable locations was achieved by real-time stabilization of fixational eye movements (Arathorn et al.,

14

2007; Yang et al., 2010). Because pixel position and time are linked in scanning systems, a digital marker was placed in the retinal video on the pixel location corresponding to the time of AOM-triggered stimulus delivery. This mark could be retrieved during analysis and served as a record of stimulus location with respect to the photoreceptor mosaic imaged in the infrared channel, the effects of chromatic dispersion notwithstanding (see next section). All imaging and psychophysical testing was conducted using a 5.6 mm system pupil and 1.28° imaging field (~400 image pixels per degree of visual angle).

2.3.2 Chromatic Dispersion Correction in a Multi-wavelength AOSLO

The multi-wavelength nature of our psychophysical apparatus renders it susceptible to the effects of chromatic aberration: even if the imaging and stimulus beams of our system are perfectly aligned as they enter the eye, chromatic dispersion within the eye itself will cause them to come to a focus in different axial planes (longitudinal chromatic aberration, or LCA) and at different locations in the transverse plane (transverse chromatic aberration, or TCA). LCA has been shown to be relatively consistent between individuals (Atchison and Smith, 2005), and can be compensated by adjusting the relative vergences of the fiber optic point sources as they enter the system. The fidelity of LCA correction can be confirmed by recording interleaved images from the IR and green channels; when LCA is properly compensated, both images are in focus at the same time. The remaining individual differences in LCA between subjects were accounted for by prioritizing focus to maximize sharpness in the green stimulation channel.

Unlike LCA, the direction and magnitude of TCA is more idiosyncratic, and will in part depend on the position of the imaging and stimulation beams relative to the eye's entrance pupil. Since it is difficult to infer chromatic offsets on the retina solely from pupil position, we employed an objective method for measuring TCA from the recorded retinal videos directly (Harmening et al., 2012). Individual TCA compensation offsets used in the experiments ranged from -15 to +20 pixels in x and y dimension in the image, corresponding to shifts of up to 13 μm on the retina, which is greater than the cone diameter for all eccentricities tested in this study. One consequence of using an image-based measure of TCA is that a significant amount of light (~50,000 cd/m^2) is required in the green channel to capture a retinal image. Because these light levels are too high to run threshold psychophysics in parallel, TCA measurements were restricted to the beginning and end of each testing session. Subjects were allowed 15 minutes to re-adapt before testing commenced, and a bite-bar was used to quell pupil motion relative to the instrument beams in the intervening period TCA measurement differences between before and after an experiment were much smaller than typical cone diameters (mean in both x and y image dimensions: 1.4 pixels). Because this difference was close to the noise limit of repeated TCA measurements, and because TCA could not be monitored during the experiment, we assumed TCA to be constant in the calculation of light delivery. Sessions where TCA shifted more than one-half of a cone diameter (~4 pixels, ~2.9 μm) between the two TCA measurements were excluded from all analyses.

2.3.3 Subjects and Psychophysical Procedures

Subjects were 4 adults (one female, three males) with normal color vision. Mydriasis and cycloplegia were achieved by instilling one drop of 1% tropicamide and 2.5% phenylephrine 15 minutes prior to testing. Informed consent was obtained from each subject and all experimental procedures adhered to the tenets of the Declaration of Helsinki. Retinal stimulation sites were chosen on a roughly horizontal meridian, 2.5°-5.5° temporally from the fovea. Eccentricity was taken from a large montage of scaled AOSLO images that included the fovea (Figure 2.1B), and measured as the distance from the cone of interest to the subject's preferred retinal locus (plotted from a 5 sec episode of fixation on a small flashing target). At each test eccentricity, high-resolution images of the vasculature were generated using an AO-based technique (Tam et al., 2010), and test sites were chosen from capillary-free regions to avoid screening by blood vessels (Figure 2.1D).
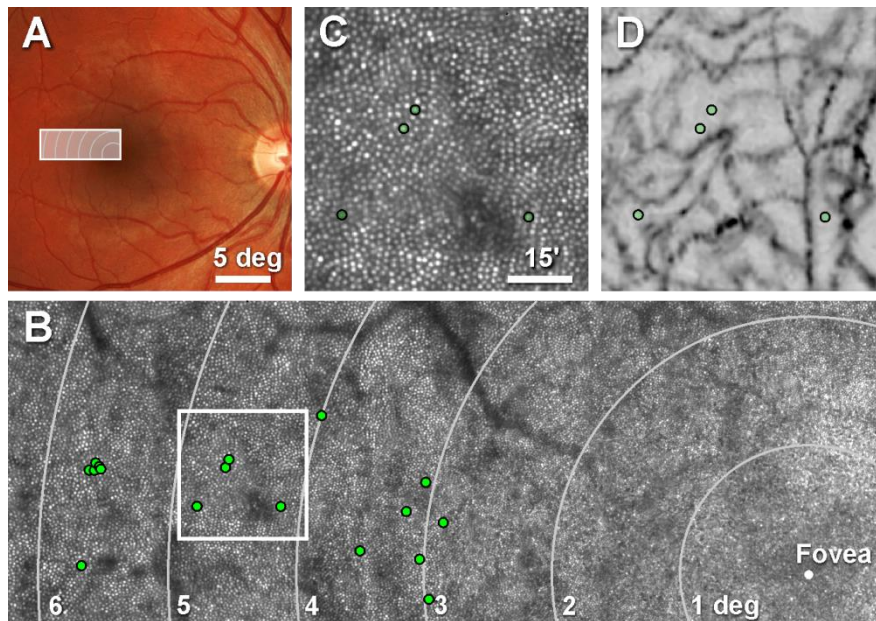
Figure 2.1| Selection of cones for targeted microstimulation. **A)** Right eye fundus photograph of Subject 2, with outlined area indicating where cones were selected for testing. **B)** Cone-resolved retinal montage of AOSLO images, with stimulation sites marked (green circles). Meandering dark structures are shadows cast by large retinal blood vessels. **C)** Field of cones from the outline in **B**, with 4 tested cones indicated. **D)** Vascular perfusion maps of the same region imaged in **C**, illustrating that stimulation sites were not situated under normally invisible capillaries (see Methods).

Visual sensitivity was assessed using an increment threshold approach. Throughout this study, light intensity values are expressed in arbitrary units (a.u.), between 0 and 1, where 0 corresponds to stimulation that contained only the constant 1.28° background field. A value of 1 corresponds to the background field plus the maximum available light intensity created by modulation of the smaller test stimulus on the retina. In radiometric terms, this value of 1 was

16

typically about 15 nW incident on the cornea. For a 3 × 3 pixel stimulus presented for one frame, this equaled about 4.27 log quanta at the cornea. Residual light leak through the green channel AOM produced a background field of ~4.3 cd/m², equaling about 4100 rhodopsin isomerizations per second (Geller and Sieving, 1993), which effectively eliminated any rod contribution to the visual response (Aguilar and Stiles, 1954; Tamura et al., 1991). The background light produced about 2.74 log quanta incident on the cornea for an area comparable in size and time to the stimulus. Thus, if a threshold was measured to be 0.5 a.u., the stimulus contained about 17 times more photons per unit time than the background field covering the same stimulus area. The task required fixation on a small external spot produced by a bright LED. While fixating, subjects reported seeing or not seeing a small green stimulus square flashed during one video frame, accompanied by an audible cue. Stimulus edge length ranged from 3 pixels up to 9 pixels in the scanning raster (3.9-9.2 μm FWHM on the retina), with 90% of tests performed with either 3 or 5 pixel squares. Due to the scanning nature of the AOSLO, stimulus light was delivered very briefly, during a time span of ~120 μs for a 3 × 3 pixel stimulus for example. Occasionally, after an experiment began, subjects reported never seeing a stimulus (possibly due to targeting an S cone); when this occurred, a new cone was selected for study.

In one experiment, we used a method of constant stimuli to derive thresholds from complete psychometric functions (n=140 trials). For each test location, 7 predefined and equally spaced stimulus intensities were presented 20 times in a randomly interleaved order, and the subjects responded in a yes-no paradigm. Subject responses for all intensity levels were used to construct psychometric functions by fitting a four-parameter logarithmic function to the data by using a maximum likelihood criterion with non-restricted intervals for lapse and guess rates (Palamedes function PAL_PFML_FIT, (Prins, 2013)); Thresholds for these experiments were defined as the stimulus intensity where the function inflects. In all other experiments, we used a self-paced, yes-no Bayesian staircase algorithm to measure threshold after 22 trials at one location, with threshold of seeing set to 50% (Watson and Pelli, 1983; King-Smith et al., 1994). Trials were randomly interleaved, with the stimulus placed either on a cone or in the space directly adjacent to it (referred to as gap condition throughout this chapter). For one experiment, patterned stimuli were generated at locations corresponding to multiple cones (2, 3, or 5 cones). The gap condition in this experiment was the same pattern shifted along a single vector to place stimuli in the multiple gaps next to the targeted cones (Figure 2.7).

2.3.4   Data Analysis and Cone Modeling

We examined the effect of stimulus position on light capture in a model cone mosaic while varying two parameters: cone aperture size and defocus (Figure 2.8). Model arrays of cones were generated corresponding to retinal eccentricities of 3.0° and 5.5° (the bounds of our testing, roughly) using cone spacing measures from the literature (Curcio et al., 1990) and assuming perfect hexagonal packing (Figure 2.8A, top). The profile of each cone's light-collecting aperture was represented by a 2-dimensional Gaussian whose full-width at half-maximum was a fixed fraction of the inner segment diameter for that eccentricity (Hirsch and Curcio, 1989). Excitation of higher order modes due to off-center stimulation might cause the

cone acceptance aperture to be non-Gaussian but a complete model is not well defined and is beyond the scope of this chapter. After blurring by a given amount of defocus, an image of our stimulus was convolved with a two-dimensional Gaussian function with a standard deviation equal to the average standard deviation of stimulus delivery for our entire pool of data (28 arcsec). Next, the resulting stimulus representation was filtered by the model cone array as its position was varied along the horizontal meridian or a 30° oblique; for each location, the summed intensity in the filtered image represents the amount of light integrated into the cone array. Light capture (LC) as a function of stimulus position was plotted (Figure 2.8A, bottom) and the light capture ratio, defined as LC_{max}/LC_{min}, was calculated. Figure 2.8B shows the light capture ratio as a function of stimulus defocus for a single cone aperture scaling factor (0.48). Light capture ratios across a range of aperture scaling factors and defocuses are shown in Figure 2.8C for the 3.0° and 5.5° eccentricities. The limits of our stimulus sizes were taken into account by using the smallest stimulus square (3 pixels) for the 3° eccentricity and the most frequently used of the larger stimuli (7 pixels) for the 5.5° eccentricity model calculation.

To facilitate comparison with our experimental data, our model adopts the following assumptions: (1) threshold is reached when some fixed amount of light is captured by the photoreceptor mosaic; (2) within a local patch of retina, each cone has the same inner segment diameter (and, thus, light acceptance profile); (3) each cone exhibits equal sensitivity to the green stimulus viewed upon the green background; and (4) the responses of adjacent cones sum linearly in the parafovea. On the basis of these assumptions, the light capture ratio represents the maximum gap/cone threshold ratio one might expect for a given set of aperture scaling and defocus parameters. The average threshold ratio for all data was then plotted as contour lines, defining our estimate of residual optical defocus for a range of aperture scaling factors (Figure 2.8C).

To account for light absorption based on actual stimulus delivery (Figure 2.9), the following model was used. For each trial in a given psychophysical staircase, the precise location of the stimulus relative to the local cone mosaic could be determined by searching for the digital mark in the simultaneously recorded retinal video, and these locations could be plotted onto a reference image comprising registered frames from each trial video, with the spread of locations representing stimulus delivery errors. The effects of blur were modeled by convolving our stimulus with point spread functions for the diffraction-limited case. The cumulative light distribution over the course of the staircase was computed by stacking these convolved stimulus profiles at the delivery location for each trial and scaling by the total number of trials (Figure 2.2E). The cumulative light distribution over the 22 trials was then filtered by the model of the cone mosaic, with the intensity in the resulting image summed to estimate the amount of light coupled into the photoreceptors (Figure 2.8B). For this analysis, a cone aperture scaling factor of 0.48 was used, which falls within the bounds of the data in Figure 2.8C and is supported by previous psychophysical studies (MacLeod et al., 1992).

To enable comparison across data collected at various parafoveal eccentricities, we normalized our light capture estimates and threshold data to their respective mean cone and gap values at each test site. After normalizing to these means, thresholds were plotted as a

18

function of estimated capture for all four subjects for a range of residual blur levels (0.0-0.1D) derived from Figure 2.8C. The resulting graph for a mean blur condition of 0.056 D is shown in Figure 2.9C. Because we expect variance in both our measures of light capture and increment threshold, we computed an orthogonal regression fit to the data. The resulting fit explains how much of the variance in the data can be explained by a linear model of light capture wherein all cones have equal weights. Because cones are known to have different weights (Field et al., 2010; Li et al., 2014), we estimated how much of the remaining variance may be due to cones with variable weights using a Monte Carlo simulation. Light capture was computed as before, except each cone weight was drawn from a distribution that varied by between zero and 50% SD from a mean cone weight of 1. The variance of these data, computed from a fit where all cone weights were equal, was then averaged over 500 simulations. This yielded an estimate of the variance that could be caused by cone weight variability alone, and is shown in Figure 2.10.

2.4   Results

2.4.1   Cone-sized Microstimulation

To conduct psychophysical testing on identified photoreceptors, several technical hurdles need to be overcome, including (1) the cones must be visualized at the microscopic level, (2) the retinal vasculature ought to be avoided, as it tends to shadow and uncontrollably scatter light, (3) the effects of chromatic aberrations have to be taken into account, and (4) ever-present eye motion must be counteracted so that stimuli land on the same retinal location on every trial. In this section, we show how these criteria were met. We first selected a region in the temporal retina along the horizontal meridian where overlying vessels are smallest and present the least interference for testing (Figure 2.1A). In this area, we used AOSLO imaging to map the cone mosaic with sub-cellular resolution (Figure 2.1B, C). All cones, except those within 0.25° of the fovea, were well resolved. We note here that variability in cone reflectance in AOSLO images is always observed, and is unlikely to significantly affect a cone's ability to capture light (Roorda and Williams, 2002; Pallikaris et al., 2003). The dark branched structures in the AOSLO montage (Figure 2.1B) are shadows cast by larger blood vessels. What cannot be resolved in these AOSLO images, however, are the capillaries, which are mainly invisible to the 840 nm wavelength used for imaging when focused on the photoreceptor layer. To ensure that we did not test any cones lying beneath capillaries (which cover a substantial portion of retinal area (Snodderly et al., 1992)), we also generated vascular maps in areas where cones were selected (Tam et al., 2010). All the cones analyzed in this study were located in capillary-free patches of retina (compare images of the same field with selected sites in Figure 2.1C and D).

The stimulation light followed the same adaptive optics corrected path as the imaging beam. Thus, in practice, we specified stimuli in terms of image pixels, with the spatial resolution constrained by the resolution of the AOSLO images. However, there are optical factors to consider when making the transition from a stimulus defined in image space to the actual distribution of light as it lands on the retina. First, since the eye's ocular media disperse light, wavelengths used for imaging and stimulation include chromatic offsets that need to be compensated (see Methods). We employed an image-based method for measuring and

correction of these offsets with sub-pixel precision (Harmening et al., 2012), ensuring that the stimulus location corresponded to the location defined in image space. Next, for the field size used (1.28° square), the sampling resolution was high enough that each photoreceptor was imaged within about 10 pixels (Figure 2.2A, B). A stimulus defined in image pixels could thus be well placed within the visible margins of a single cell (Figure 2.2B).

As in any optical device, diffraction effects pose the limits to resolution and will change the geometry of the stimulus. With adaptive optics correction, the incident beam aperture (5.6 mm) yields a point spread function (PSF) with full width at half maximum (FWHM) of 24 arcsec at the stimulation wavelength (543 nm). Expressed in image space, this corresponds to a FWHM of 2.6 pixels (1.9 µm on the retina). With optimal wavefront correction, a nominal 3×3 pixel stimulus (Figure 2.2B) convolved by the system PSF produced a light intensity profile on the retina where the 5% intensity contour corresponded to a nearly circular area 7.3 pixels in diameter (5.3 µm on the retina), roughly matching the diameter of imaged cone apertures at 3° eccentricity (Figure 2.2C). Similar agreement between cone and stimulus size was observed with larger test stimuli that were used at higher eccentricities due to reduced detection.
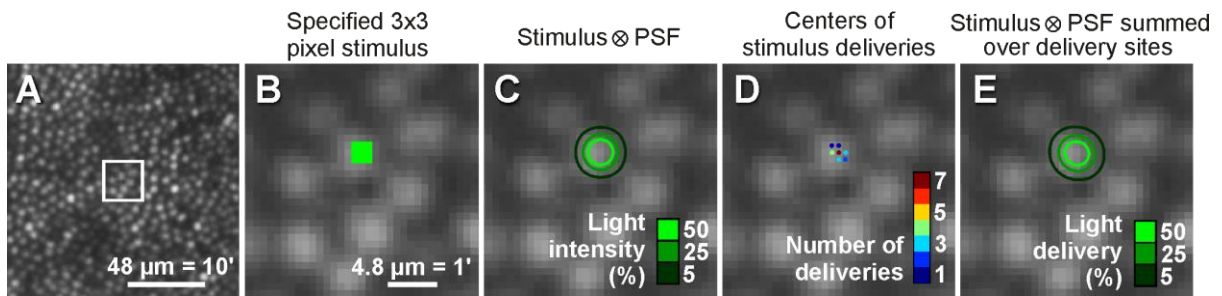
Figure 2.2| Stimulus geometry and delivered light distribution. **A)** AOSLO image of cone mosaic at 3.1° eccentricity, with outlined area scaled up in panels **B-E**. **B)** Cone reflectance profiles at this eccentricity span ~7 pixels, nearly 5 µm in diameter. Stimuli were specified in image pixels, a 3×3 pixel square stimulus in this example. **C)** Light intensity delivered to the retina is estimated by convolving the stimulus geometry with the diffraction-limited point-spread function (PSF) of the eye (see Methods). Intensity contours show that the light spreads over a broader area than the 3×3 specification. **D)** Plot of actual delivery locations of the stimulus center relative to the targeted cone for a 22-trial psychophysical run. Positional delivery errors in eye motion correction caused stimulus deliveries to be jittered from trial to trial. **E)** Cumulative distribution of light delivery on the retina during the run in **D**, derived from the diffraction-limited stimulus integrated over the actual delivery locations. TCA was assumed to be constant for this analysis (see Methods).

Repeated stimulation under constant conditions is mandatory in any psychophysical testing. Consequently, we further characterized light delivery by taking into account spatial delivery errors over each set of stimulus trials after fixational eye movements had been compensated for with real-time eye tracking (see Methods). When a selected cone was identified and tracked during an experiment, it was possible to repeatedly deliver stimuli within 1-2 pixels (0.73-1.46 µm) of the targeted location (Figure 2.2D). In the given example, 7 out of 22 deliveries landed exactly at the targeted image pixel, with the remaining 15 deliveries distributed over the

immediately neighboring pixels. Across all 324 staircase experiments carried out in the study (a total of 7128 stimulus trials), the average standard deviation of delivery jitter was 2.2 pixels, in both x and y image coordinates (1.6 μm on the retina). For a single threshold experiment comprised of 22 repeated trials, the actual light delivery was calculated as the PSF-convolved nominal stimulus definition summed across the actual delivery locations (Figure 2.2E). The resulting light delivery distribution is the final estimation of actual light distribution during one threshold experiment. The 5% delivery contour had a radially averaged diameter of 7.9 pixels (5.7 μm on the retina). Integrating the light distribution within this 5% contour showed that 82% of all the delivered light fell within this contour. Although this suggests that, even after repeated presentation, most of the delivered light was constrained to a retinal area the size of a single cone, we note that this does not take into account uncontrollable light scatter (see Discussion). Nonetheless, the following results suggest that most of the stimulus light during a set of trials was confined to a single cone.

2.4.2 Single-cone Increment Thresholds

With the ability to repeatedly direct light to targeted cones, we first examined whether psychometric functions could be obtained from microstimulation. Luminance increment thresholds were measured in three subjects (S1-3) at three different eccentricities each with a method of constant stimuli. Tested eccentricities were similar for all subjects (S1: 2.41°, 3.42°, 3.93°; S2: 2.47°, 3.07°, 4.23°; S3: 1.98°, 2.7°, 4.13°). For each test location, 7 predefined and equally spaced stimulus intensities were presented 20 times in a randomly interleaved order, and the subjects responded in a Yes-No paradigm. Figure 2.3A shows the light delivery distributions for each 140 trial run in subject S2. Note that the 1% delivery contour is included to document single delivery outliers in the course of the experiment. It is also worth noting that cone size and spacing increased with eccentricity, as expected from known anatomy (Curcio et al., 1990). At each eccentricity in subject S2, psychometric functions were obtained that showed increasing thresholds and shallower slopes with increasing eccentricity (Figure 2.3B). Similar data were found for the other two subjects (Figure 2.3C), with the correlation between threshold and eccentricity being fairly consistent between subjects (Figure 2.3D). In subject S3, the same cone at 1.98° eccentricity was tested on different days and yielded very similar thresholds (0.25 and 0.27), suggesting that the experimental conditions were stable over time. Across subjects and eccentricities, the diameter of the 5% light delivery contour was typically 8.5 pixels (6.2 μm on the retina).

Our findings agree with prior studies showing that photopic thresholds are higher for a constantly sized stimulus as one tests further from the fovea (Wilson, 1970; Lie, 1980; Inui et al., 1981), the difference here being that most of the light was delivered to only one cone. The steepness of the psychometric functions also became shallower with increasing eccentricity, which indicates increases in signal uncertainty (Pelli, 1985; Tyler and Chen, 2000). The most likely retinal source of this uncertainty is increased cone convergence onto bipolar or ganglion cells with eccentricity (Anderson et al., 1991; Dacey, 1993; Volbrecht et al., 2000; Drasdo et al., 2007). These data suggest that standard psychometric assessment of visual function can be performed in the parafovea with cone-sized microstimulation.
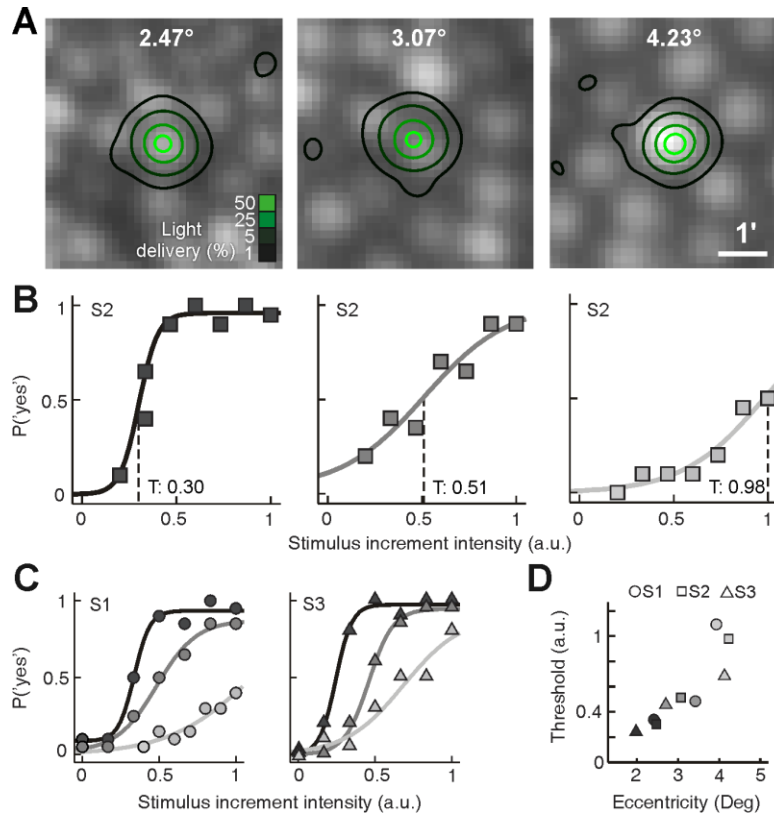
Figure 2.3| Microstimulation threshold measurements. **A)** Light delivery distribution achieved in Subject 2 at three eccentricities, for 140-trial runs using the method-of-constant-stimuli approach. Note the increase in cone size and spacing with eccentricity. **B)** Psychometric functions were constructed by fitting a logarithmic function (lines) to the frequency-of-seeing data at each eccentricity, E, (coded by gray level here and in **C,D**). Threshold, T, was defined as the intensity where the function inflects (dashed lines). **C)** Same as in **B** plotted for subjects S1 and S3. For the most eccentric test sites, modulation limits in the light delivery system (see Methods) result in a clipping of the upper portion of the psychometric function. **D)** Increment threshold was calculated from each psychometric fit and was plotted against eccentricity for all subjects.

2.4.5   Positional Effect of Stimulus Placement

The structures seen in the AOSLO images mostly stem from light emitted at the inner aperture (near the external limiting membrane) of the optical fiber component of the photoreceptor. Because these act as optical waveguides for light traveling to the photopigment-filled outer segments, we tested whether perceptual sensitivity was dependent on the exact placement of the stimulus with respect to the individual cone apertures. The center of the inner segment is where light is captured most efficiently, and that efficiency drops off as a Gaussian function as the edge of the inner segment is reached. If this light capturing profile is detectable psychophysically, it would imply that (1) our visual performance is ultimately determined by exactly where on this mosaic light falls and (2) stimulus energy can be effectively constrained to a cone-sized area in spite of the optical and technical obstacles outlined above.

We measured increment thresholds in four subjects (S1-4), this time using a Bayesian staircase method to allow more rapid estimation of threshold (see Methods). Stimuli were delivered either to the center of a targeted cone or to an adjacent gap between the targeted cone and a neighboring one (referred to as cone and gap conditions, respectively). Stimulus trials were randomly interleaved, drawn from two staircases operating simultaneously for the two conditions. Figure 2.4A shows an example of the light delivery distributions in one subject for a cone/gap pair (S2, 3.5° eccentricity). Threshold estimates were measured multiple times by repeating runs of interleaved staircases (Figure 2.4B). In this example, all of the threshold estimates in the cone condition were lower than in the gap condition, and the difference between means were significant (cone: 0.46±0.04 a.u.; gap 0.74±0.06; p<0.01, two-tailed t-test). For the cone/gap pair in Figure 2.4, 61% more light had to be delivered to reach threshold when light was not centered on the cone. In the model described below, we consider how threshold is still attainable in the gap condition, despite it being counter-intuitive.
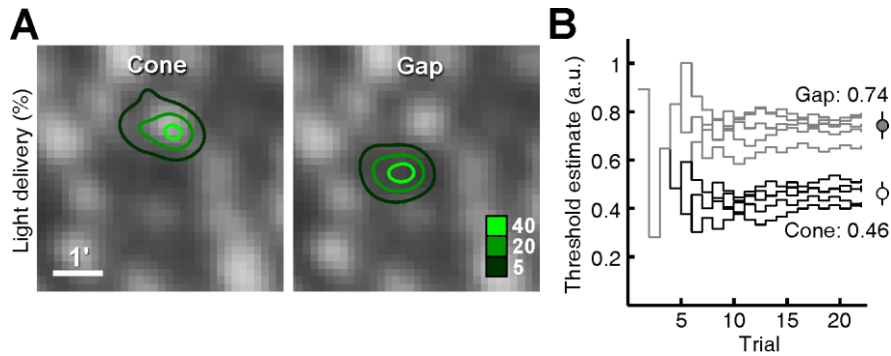
Figure 2.4| Comparing cone versus gap thresholds. **A)** Light delivery profiles for two stimulus conditions, either on a cone (left) or in the adjacent dark gap between cones (right), achieved during randomly interleaved trials (22 trials per condition, 3.5° eccentricity). **B)** Trial-by-trial stimulus intensity progress during 5 Bayesian adaptive staircases for each condition. Mean threshold measured for the cone condition was lower than for the gap condition (circles; mean ±1 SD).

The pronounced difference between cone and gap thresholds was present in all sites tested (n=33, 2.5°-5.5° eccentricity), in all subjects (S1 n=8; S2 n=16; S3 n=4; S4 n=5), and with different stimulus sizes (tested range: 3-9 pixels square). To present these data as a population, we calculated a threshold ratio, comparing the mean gap condition against the mean cone condition for each test site. This ratio normalizes the data by removing the effect of eccentricity and day-to-day variation in background on threshold. A threshold ratio greater than 1 signifies relatively worse sensitivity for the gap condition, while a ratio near 1 indicates no effect of stimulus placement. As evident in Figure 2.5A, all mean gap/cone ratios were greater than 1, with an overall average ratio of 1.48 (range: 1.04-2.39) and with 16 out of 33 of individual sites reaching significance (p<0.05, two-tailed t-test). Across the population, therefore, increment thresholds were generally 1.5 times higher when the light was directed between cones than when it was delivered directly on a cone.

23
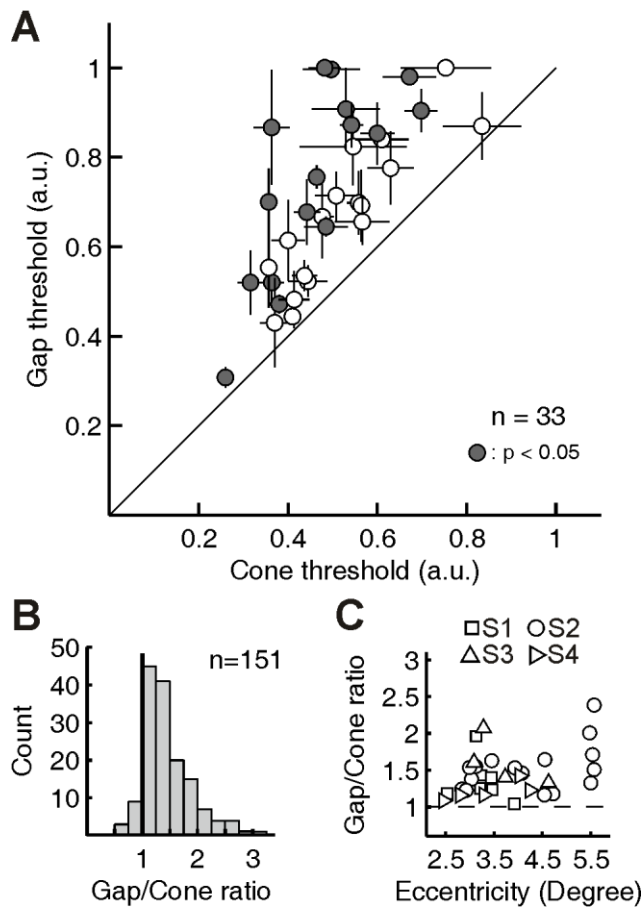
Figure 2.5| Population data for cone versus gap thresholds. **A)** Mean cone thresholds plotted against mean gap thresholds for 33 sites tested in 4 subjects. Horizontal and vertical bars represent ±1 SEM. Filled circles indicate a significant difference between cone and gap thresholds (two-tailed t-test, p≤0.05). **B)** Distribution of gap/cone threshold ratios measured during each pair of staircase runs is skewed towards higher values, with a mean gap/cone ratio of 1.48 (median: 1.38). **C)** Gap/cone threshold ratios plotted as a function of retinal eccentricity for each subject.

The mean ratio data obtained from repeated runs at any one location obscure the wider range of gap/cone ratios we observed during single pairs of runs. The distribution of pairwise gap/cone ratios, measured from each individual pair of runs, ranged from 0.46 to 3.13, and was skewed toward higher values (Figure 2.5B). Analyzed in this way, 138 out of the 151 threshold pairs (91%) had a ratio greater than one. This distribution may underestimate the true extent of the higher gap/cone ratios given that stimulus modulation constraints may lead to ceiling effects in the algorithm used to estimate thresholds (see Methods). Because we tested sites over a range of retinal eccentricities, it was possible that threshold ratios would increase with eccentricity, as the gap between cones tends to widen. At higher eccentricities we used larger stimuli to ensure detection (mostly 5 pixel square compared to 3 pixel square at lower eccentricity), possibly rivaling the effect of increased spacing. A plot of the mean gap/cone ratios as a function of eccentricity revealed a mild positive eccentricity effect with little

24

predictive power (linear regression slope: 0.12, R^2: 0.14, Figure 2.5C). Given the low sample count at higher eccentricities, we used the mean gap/cone ratio of 1.48 as a best estimate for the positional effect of stimulus placement in the analysis below.

As a means of quantifying possible adaptation or fatigue effects that would alter thresholds with time (see for example (Frome et al., 1981)), we tested whether threshold values changed over the course of repeated testing. Normalizing thresholds with respect to the values found in the first run, we found that across subjects and conditions, mean normalized thresholds rose by 7% between repeated runs (Figure 2.6A). This threshold drift towards higher values reached significance (p<0.01, two-tailed t-test) after the second repetition. Because the threshold drift rate was not significantly different for cone and gap conditions, our analysis of a gap/cone threshold ratio was not affected. A Bland-Altman analysis of measurement repeatability (Bland and Altman, 1986) did not indicate any systematic threshold differences between repeated measurements (Figure 2.6B).
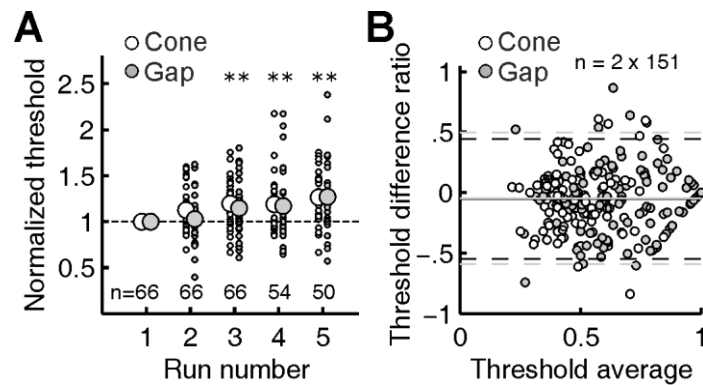
Figure 2.6| Threshold drift and Bland-Altman analysis. **A)** For each stimulus location, repeated threshold measurements were normalized against the threshold measured during the first run, for cone and gap stimulations separately. Thresholds increased by ~7% with each run, suggesting fatigue or adaptation effects. Asterisks mark significant mean threshold increases (p≤0.01); threshold drift over multiple runs did not differ between cone and gap conditions. Small dots correspond to individual thresholds, larger circles are mean values. **B)** Bland-Altman analysis reveals no significant systematic change between pairs of repeated threshold measurements (n = 151 paired measures). The V-shaped arrangement of data points towards higher average values is expected due to our maximum displayable stimulus intensity of 1. Solid lines are the mean, dashed lines encompass 95% of difference ratios.

If perceptual thresholds for a single cone are sensitive to the exact placement of stimulus light, then instances where multiple cones are stimulated should also exhibit a positional effect. We selected test conditions and eccentricities where the subjects reported seeing the stimulus only when two or more cones were stimulated. In two subjects (S3 and S4), increment thresholds were measured as described before, with the exception that two, three or five cones were targeted for simultaneous stimulation (Figure 2.7). In all cases, mean cone thresholds were significantly lower than mean gap thresholds (p≤0.01, two-tailed t-test). With two cone

stimuli at 3.86° eccentricity, the mean gap/cone ratio was 1.8; with three stimuli at 3.40° the ratio was 1.3; and with five stimuli at 4.44° the gap/cone ratio was 1.7 (in this last example, a 3-cone stimulus was not visible to the subject). Thus, while the patterned stimulation required that cone signals combine in order to reach threshold, it was still the case that delivering light to areas between the cones profoundly compromised detection. It suggests that, even at the perceptual level, the cone mosaic cannot be treated as a uniform sheet of sensitivity; rather, it has peaks and troughs of sensitivity defined by the position of each cone.
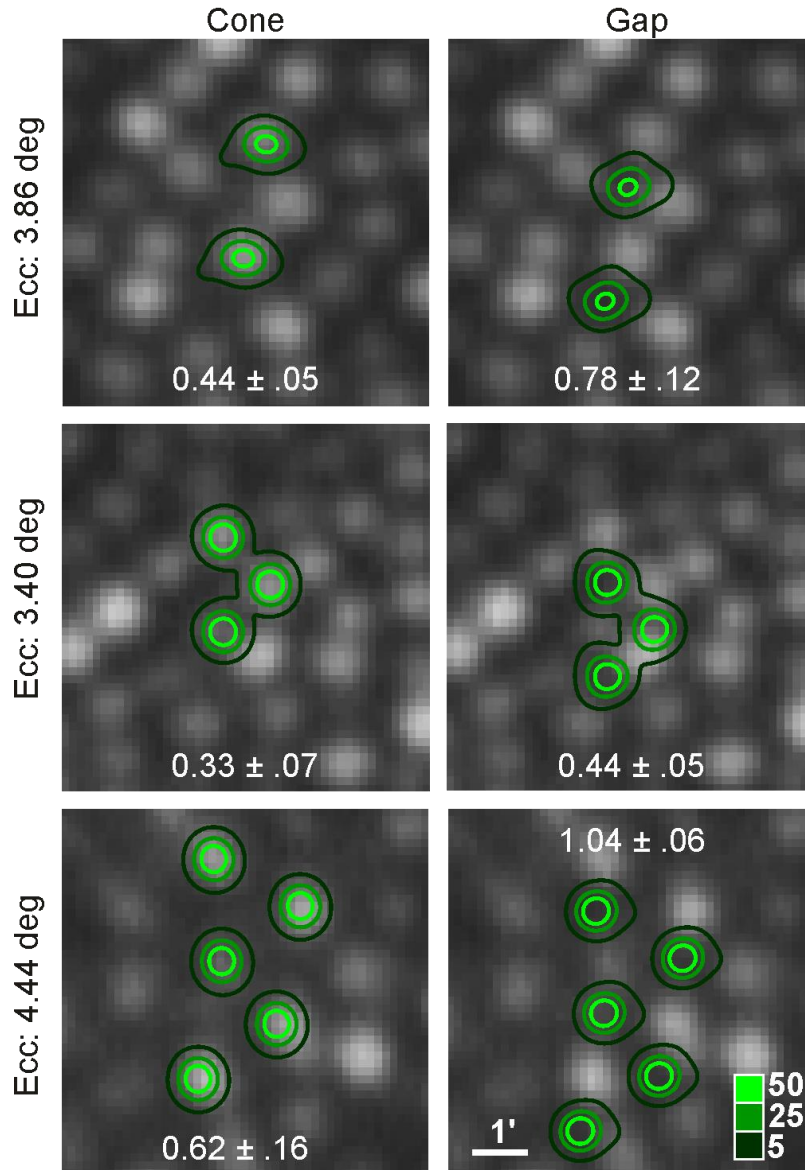
Figure 2.7| Revealing perceptual grain with patterned stimulation. In two subjects at three eccentricities, cone and gap thresholds were measured when 2, 3 or 5 cones were stimulated simultaneously, again with interleaved trials. In all cases, cone thresholds were significantly lower than gap thresholds (p≤0.01). Numbers indicate mean threshold values ±1 SD from 5 repeated runs. Light delivery contours derived as in Figure 2.2.

2.4.6   Light Capture Model

The gap/cone threshold ratios we observed support the hypothesis that light capture—and, consequently, visual sensitivity—in the parafovea is governed by the microscopic gradient manifest in the light collecting properties of individual photoreceptors. One limitation to expressing the data in this fashion is that it requires a continuous variable—stimulus position— to be allocated to one of two categories (viz. cone or gap). To explain the effect of stimulus position on threshold quantitatively, we developed a model of light capture that incorporated data from the trial-by-trial stimulus positions over the course of each psychophysical staircase and the local arrangement of retinal receptors imaged during testing.

The first task in creating the model required validating our estimates of the spatiotemporal distribution of our stimulus on the retina (Figure 2.2). For a number of reasons (see Discussion), residual optical spread (hereafter referred to as residual defocus) not sensed or corrected by our AOSLO system could lead to significant light absorption in neighboring cones. To estimate the magnitude of this residual defocus, we examined the effect of stimulus position on light capture in a model cone mosaic (Figure 2.8A; for details, see Figure legend and Methods). We adopted the assumption that, for neighboring cones in the parafovea, cone signals sum linearly and with equal perceptual weight (differential contribution of L- and M-cones is negligible because we used an equally driving wavelength, 543 nm), such that threshold will be reached when some fixed amount of light is captured by the photoreceptor array. Thus, as the position of a cone-sized stimulus is varied with respect to the cone mosaic, threshold will scale inversely with light capture. For example, when light capture is low (e.g. in the gap condition), more light must be delivered to trigger detection. We compared the ratio of light capture for stimuli landing on a cone and in its adjacent gap at a given eccentricity to the mean gap/cone threshold ratios measured at similar eccentricities. Any remaining discrepancy between the estimated light capture and psychophysical ratios was attributed to residual, uncorrected blur, which has the effect of flattening the light capture gradient (Figure 2.8B).

Residual blur may arise from defocus or uncorrected aberrations; hereafter we will term this *equivalent defocus* since both effects are essentially the same when the errors are small (Zhang and Roorda, 2006). After accounting for diffraction and additional motion blur introduced by stimulus delivery errors (jitter SD = 1.8 pixels), and using an estimate of cone aperture scaling (MacLeod et al., 1992), we estimated our equivalent defocus to be between 0.057 and 0.061 diopters (Figure 2.8B). When the size of the cone aperture was allowed to vary over a reasonable range of Gaussian profile widths (MacLeod et al., 1992), the model yielded defocus estimates ranging from 0 to no greater than 0.08 diopters (Figure 2.8C). These results imply that equivalent defocus was not a major factor contributing to the observed gap/cone threshold ratios. It is worth noting that under natural viewing conditions the cone/gap ratios would tend to unity, because normal ocular aberrations would lead to much larger optical spread than what is found here (points >0.1 D in Figure 2.8C); this indicates that the finest grain of light capture would only be perceptible at our parafoveal test locations when aberrations are minimized.
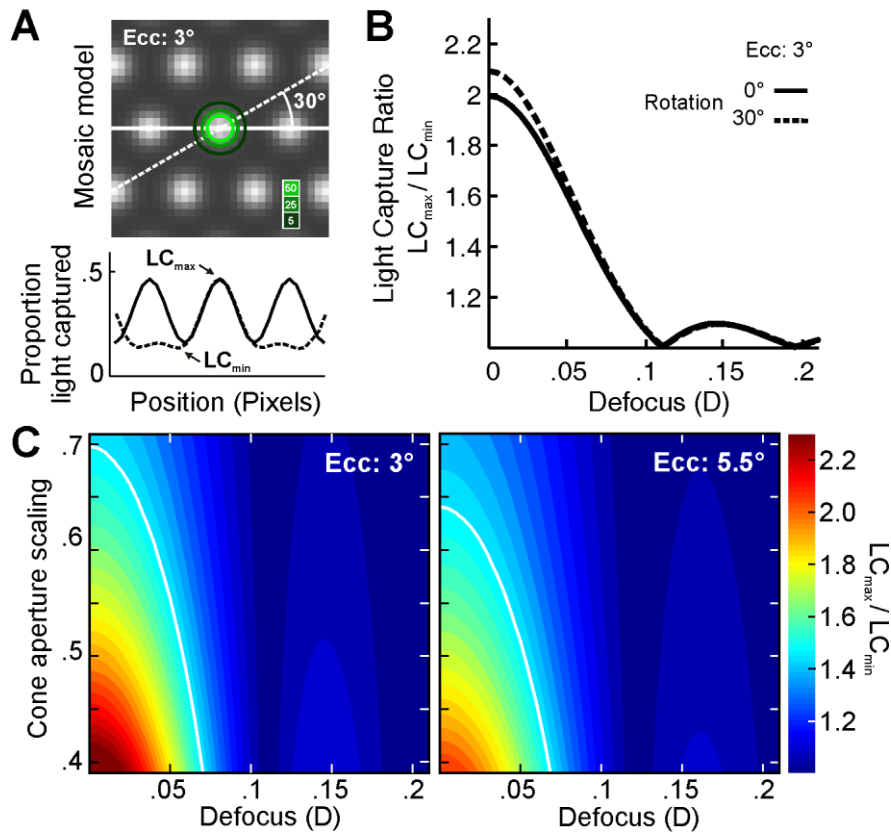
Figure 2.8| Model of cone light acceptance and optical defocus. **A)** A hexagonally packed array of Gaussian cone apertures serves as a light capturing model (upper panel). Translation of a 3×3 pixel stimulus (contours as in Figure 2.2) along a horizontal or 30° oblique line produces light capture (LC) that varies with position (lower panel). **B)** The ratio LC_{max}/LC_{min} derived from the light capture peaks and troughs in **A** is plotted as a function of added stimulus defocus (solid line). The 30° orientation is indicated by dashed lines. Zero defocus corresponds to a diffraction-limited stimulus geometry (as in Figure 2.2C). Given the mean psychophysical gap/cone ratio of 1.48 (corresponding to LC_{max}/LC_{min} in the model), the model suggests that our stimulus was blurred by about 0.06 diopters. **C)** Same analysis as in **B**, with cone aperture (proportion of inner segment diameter) as a free parameter (ordinate). The mean gap/cone ratio (1.48) is superimposed as white line. The full spectrum of scaling vs. defocus was calculated for 3° and 5.5° eccentricity (left and right panel, respectively).

Having arrived at an estimate of the equivalent defocus of the stimulus, a model of light capture identical to the one described in the previous section was generated, with the exception that the actual experimental stimulus locations and receptor arrangements were used in place of their idealized counterparts. Spatial stimulus representations were generated in the same manner as Figure 2.2 and filtered by the cone mosaic to give an estimate of light capture (Figure 2.9A-B). To facilitate comparison across data collected at various parafoveal eccentricities—where photopic threshold and the geometry of retinal light capture both change—it was necessary to normalize our light capture estimates and threshold data. For capture, data were normalized by the mean light capture for the local arrangement of receptors and delivery at each test site; for threshold, data were normalized to the mean value

of the cone and gap condition at each test location. After such normalization, thresholds were plotted as a function of estimated light capture, and showed that threshold decreased with increasing light capture (Figure 2.9C). If sensitivity thresholds were primarily governed by light capture in single cones, we would expect a negative unity slope in such a plot. Because the residual defocus must be non-zero in a real eye in our experiments, we determined what amount of defocus would yield a slope of -1 from an orthogonal regression to the data (R^2_T: 0.47, R^2_C:0.46). This residual stimulus blur had an equivalent defocus of 0.056 diopters, a value that agrees with our estimate of residual blur in the model analysis (Figure 2.8). We conclude from these results that perceptual thresholds for cone and gap conditions can be explained directly by a parsimonious model of cone light capture that includes a small amount of defocus or uncorrected aberrations.
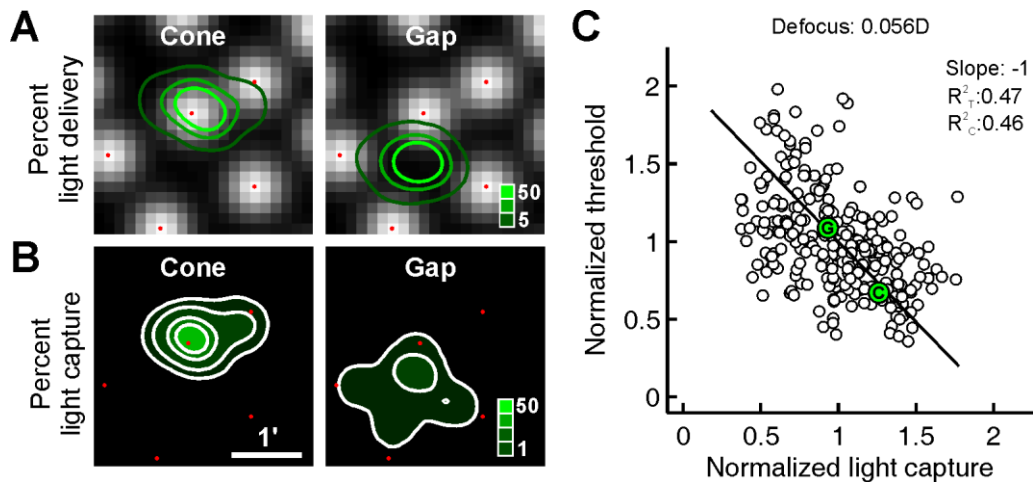
Figure 2.9| Light absorption model based on experimental stimulus delivery. **A)** Cone locations from high magnification cone images around the stimulus location were replaced by Gaussian apertures (locations indicated by red dots). Light delivery from an example 22-trial run is shown as contours over the idealized cone apertures at this 3° test site for the cone and gap conditions. **B)** Proportion of captured light at each stimulus location is shown, calculated by the product of the stimulus location contours with the model apertures. **C)** The spatially summed light capture in **B**, is computed for each threshold location, normalized against the mean within each group of repeated runs, and plotted against the similarly normalized threshold measurements. A residual stimulus blur of 0.056D was applied (see Results) to arrive at unity slope for an orthogonal regression (solid line). The coefficients of determination are given for both threshold (R^2_T) and light capture (R^2_C) variance. The example cone ('C') and gap ('G') pair from **A** and **B** is indicated within their respective data points.

The linear fit in Figure 2.9C, which captures 47% of the variance in the data, assumes that cones are equally weighted in the model, leaving about half of the variance unexplained. It was recently shown that cone inputs converging onto single ganglion cells in primate retina have quite variable weighting (Li et al., 2014). So it is likely that some of the variance not explained by the linear model was due to cones having different weights. To estimate the impact of this variation, we simulated light capture in our data with cone weights that randomly varied by up to 50% SD from a mean cone weight (Figure 2.10). This simulation showed that 25% of the

variance in the data could arise from a 20% variance in cone weighting alone. Although we have no estimate of the true distribution of cone weights, the simulation suggests that half of the unexplained variance in our linear model could result from a modest variability in cone weights. The remaining variance is likely due to nonlinear summation occurring downstream from the cones and from noise in the psychophysical measurement itself.
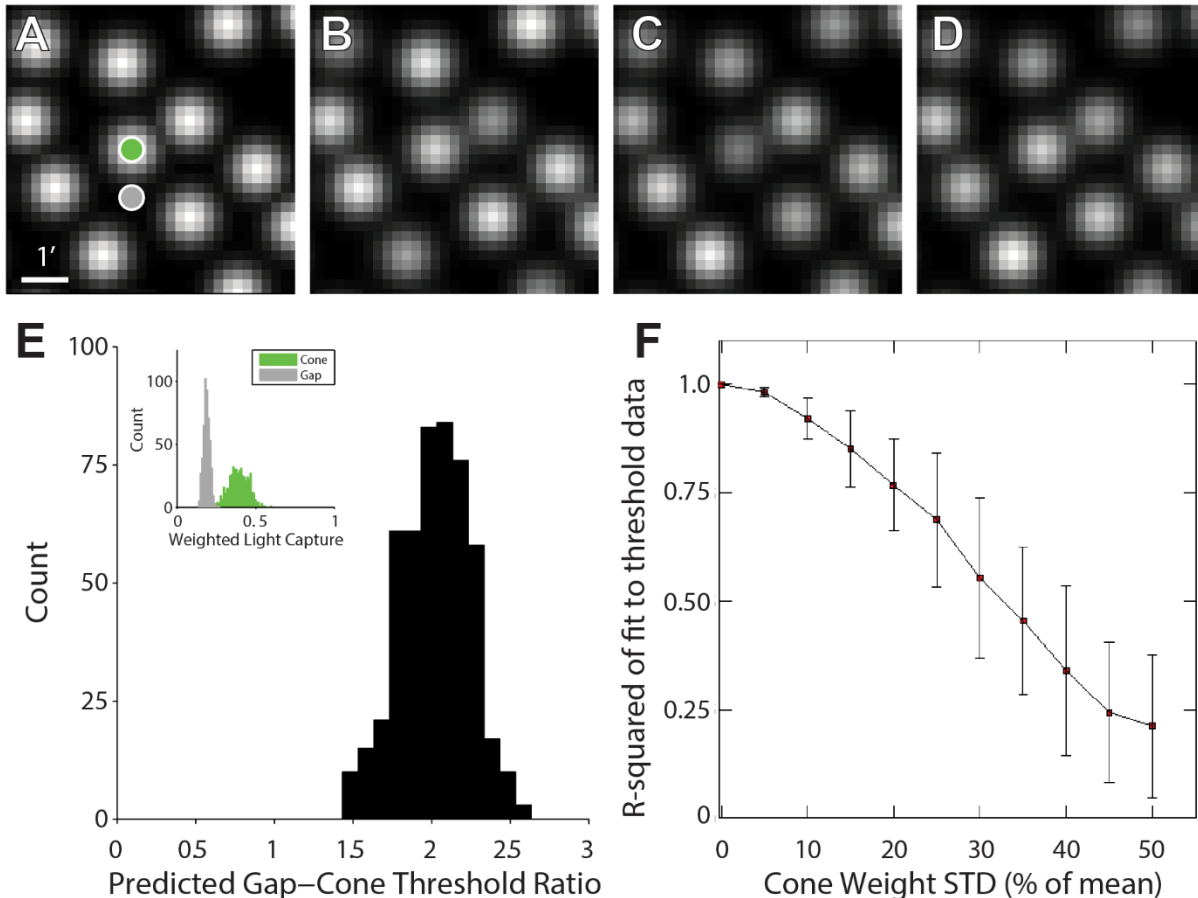
Figure 2.10| Modeling the effect of non-uniform cone weighting on light capture. **A)** Uniformly-weighted model cone array from Figure 2.9A. Green and gray dots indicate cone and gap targets, respectively **B-D)** Model cone arrays with individual weights drawn randomly from a normal distribution with a mean of 1.0 and a standard deviation of 0.20. Cone weights are indicated by the relative intensities of each receptor. Each array represents an iteration of the Monte Carlo analysis (N = 500) described in the text, and was used to filter the spatio-temporal representations of the cone and gap stimulus, respectively (see Figure 9B). **E)** Histogram of predicted gap-cone threshold ratios resulting from varying the cone weights while holding receptor arrangement and stimulus spatio-temporal representation constant. Thresholds were estimated by adjusting the incident light needed to offset the variability in cone (green) and gap (red) light capture shown in the inset plot, such that the filtered output of the randomly-weighted cone array remained constant. **F)** Variance introduced to our linear model by varying cone input weights. For each cone-gap pair in our dataset, the coefficient of determination (r^2) was computed for the fit of the simulated data to the original data. This process was repeated for cone weight distributions of increasing standard deviation and averaged across all cone-gap pairs (error bars = ± 1 standard deviation).

2.5 Discussion

By detecting visual sensitivity to positional shifts on the order of a photoreceptor's size, we demonstrated that fundamental properties of the photopic retina can be revealed by microstimulation. Sensitivity decreased when light was directed into gaps between cones, and increased when light was delivered to cone centers. Because it was accounted for by a model of cone acceptance apertures, the detection of microstimuli appears to be governed simply by cone light capture geometry.

Whether the increment thresholds we measured were derived solely from the activation of one cone remains, however, an open question. Although the trial-averaged stimulus diameters suggest that photon delivery was largely restricted to one cone, possible sources of undetectable stimulus blur exist that could result in photon absorption in more than one cone. These sources include inadequate correction of longitudinal chromatic aberration (Atchison and Smith, 2005), and predominantly, local intra-ocular scatter (Vos and Bouman, 1964; Vos et al., 1976). Such stray light arises from the corneal and lens interfaces, the vitreous humour, and the retinal tissue lying in front of the photoreceptors (Boynton and Clarke, 1964; Franssen et al., 2007; van den Berg et al., 2013). It is also possible that light reflecting off the retinal pigment epithelium could be detected by neighboring cones and contributing to the percept. These scattering sources cannot be sensed or controlled by the AOSLO. We minimized the effect of scatter by using thresholds as our metric, as this uses the least amount of light to perform a perceptual task. Nonetheless, even for the cone-targeted condition, we have no direct evidence that activity arising from only one cone suffices for reaching perceptual threshold.

However, indirect evidence from the multi-cone patterned stimulus experiments suggests that single cones do contribute in a straightforward way to perception. To achieve threshold in these experiments, more than one cone had to be stimulated. The recruitment of multiple cones in order to reach threshold at greater eccentricities (Figure 2.7) is consistent with spatial summation, and with the convergence of cone inputs onto downstream retinal cells where the signals combine (Wilson, 1970; Inui et al., 1981; Volbrecht et al., 2000). Stimulation of multiple cones often shows linear summation up to some critical area (Ricco's Law). Although for a given retinal eccentricity this critical area changes with background intensity and stimulus duration (Barlow, 1958), our stimuli likely fell within the critical area for the eccentricities tested (Inui et al., 1981). Together with the results from our light capture model, these data suggest that if a cone is capturing light, it adds to the signal driving threshold.

Our adaptive optics instrument cannot correct for forward light scatter arising from discontinuities in the optics. Although this light scatter may be significant, the energy is distributed widely and uniformly, such that the contribution onto any individual cone—even neighboring cones—is estimated to be $<10^{-3}$ of the peak intensity for young eyes (Van den Berg et al., 2010). By comparison, the intensity of the first Airy disk PSF ring is ~1% of the peak. Moreover, when the focused PSF location is shifted, its energy distribution is altered dramatically relative to the cone mosaic, whereas the distribution of scattered energy is not. Assuming that light is summed linearly over the 6 adjacent cones that typically surround a

31

single cone, then the total scattered light absorbed in these cones will be far less than that resulting from the blur arising from diffraction plus motion, which the model suggests is already lower than 5% of the light absorbed by the mosaic. The fact that threshold in the gap condition was essentially explained by the light capture model provides further support that intra-retinal scatter does not play a significant role, and that pooling of signals from surrounding cones receiving very small amounts of light contribute negligibly to the threshold. Some of the variance in the data in Figure 2.9C arises from other sources of residual stimulus blur, but it cannot be readily separated from the many post-receptor sources of noise that accompany threshold tasks.

Prior visual testing with adaptive optics corrected microstimuli suggests indirectly that percepts can be mediated by the activity of individual cones. Cone-sized scotomas caused by photoreceptor dysfunction in a deuteranopic subject were detected psychophysically with briefly flashed microstimuli (Makous et al., 2006). A recent model to explain color-naming variability arising from microstimuli suggests that the percepts are accounted for by signals from one cone (Hofer et al., 2005a; Brainard et al., 2008). Psychophysical results derived from laser interferometry that bypass the eye's optical limitations identify the finest channels of visual perception as matching receptive fields that are about the size of foveal cone photoreceptors (Smallman et al., 1996). Other studies used small spots without adaptive optics correction to assess single cone perception. Williams and colleagues reported perceptual S cone mapping by probing just outside the foveola (Williams et al., 1981). Absolute threshold measurements determined L/M cone ratios in the fovea and mid periphery, derived from the fact that only a few cones are likely required for such thresholds (Cicerone and Nerger, 1989b; Wesner et al., 1991; Otake and Cicerone, 2000). Our results build upon these earlier studies showing that percepts can be shaped by signals originating from single cones. The major advantages reported here are that the specific cone being tested is known and it can be stimulated repeatedly; thus perceptual sequelae can be measured directly from the cone of interest.

It has long been accepted that the waveguiding property of cones influences their light capture geometry. This line of thinking was founded on the seminal study of Stiles and Crawford, who found light entering off-axis (at the pupil's edge) harder to detect than light entering along the eye's optical axis (Stiles and Crawford, 1933). An explanation involving cones behaving as optical waveguides with a Gaussian-shaped light acceptance profile was subsequently proffered (Enoch et al., 1981; Vohnsen, 2007). It is thought that waveguiding occurs in the cone inner segment, where the higher internal refractive index—combined with photoreceptor tapering—leads to enhanced funneling of photons into the pigment-laden outer segment (Enoch, 1961; Miller and Bernard, 1983; Hoang et al., 2002). However, recent work suggests that the magnitude of the Stiles-Crawford effect is highly dependent on the coherence properties of the stimulus light source and conditions of illumination under which it is measured (Vohnsen and Rativa, 2011). The absence of the Stiles-Crawford effect for coherent beams displaced symmetrically across the pupil casts doubt on the role of cone waveguiding in this phenomenon, and a framework incorporating the interactions of electro-magnetic

disturbances across image space has been put forth to better account for these findings (Westheimer, 2013).

For our experiment, the use of a partially coherent source further muddies the waters, and a complete theoretical treatment is beyond the aim of this chapter. Nevertheless, cones must collect and transduce photons over some three-dimensional space, and the size and shape of this acceptance profile remains a matter of debate. Studies employing gratings as stimuli suggest light is integrated over the full diameter of the inner segment, both in the fovea (Miller and Bernard, 1983) and periphery (Anderson et al., 1991). By contrast, when studying the distortion percepts generated by high-frequency interference fringes, the inferred cone aperture was ~48% of the inner segment diameter (MacLeod et al., 1992; Chen et al., 1993). We now show that such light capture profiles can be measured perceptually across just one cone. Along with the light capture model, the decreased sensitivity in the gaps between cones support the conclusion that the light-collecting aperture is smaller than the diameter of the inner segment. This result also obviates any prominent role for Müller cells in coupling light to the photoreceptors, at least near the fovea (Franze et al., 2007; Labin et al., 2014).

Given that many combinations of cone aperture size and equivalent defocus can produce agreement between the psychophysical data and the light capture model, we can only set limits on the likely size of the cone apertures. The maximum residual blur estimated by our model (equivalent defocus of 0.08 diopters) is less than the subjective depth-of-focus for the parafovea (Wang and Ciuffreda, 2006); but, given it is at the upper limit of the range of the axial resolution for our system (computed to be ±0.1 diopter [~74 microns] with 543 nm light and a confocal aperture of 3 Airy disk radii for a 5.6 mm pupil (Venkateswaran et al., 2004)), our focus error is <0.1 diopters. This yields a minimal cone aperture of 10% of the inner segment diameter, an unlikely value considering earlier findings (MacLeod et al., 1992). At the upper limit, in perfect focus, the cone aperture is unlikely to be above 70% of the inner segment diameter (Figure 2.8C). However, non-linear pooling of signals across space, which would likely diminish inputs of weakly-stimulated cones (cf. (Bölinger and Gollisch, 2012)), could cause this estimate to shift upwards. Given such limits on the aperture sizes, it is clear that the spatial grain of perception should initially be determined by the exact arrangement of cones in any patch of retina and the exact placement of stimuli onto those cones.

2.6 Summary

Functional testing at the cellular level in the retina creates new opportunities for vision science and retinal disease assessment. It has not been possible previously to stimulate single sensory receptors in the visual system *in vivo,* yet one of the major goals in neuroscience is to understand how perception is mediated by the activity of single neurons (Parker and Newsome, 1998). The stage is now set for probing how signals from multiple cones interact to generate percepts, and how different retinal ganglion cell types might best be stimulated. In the ophthalmological clinic, functional testing of damaged cones may prove useful (Roorda, 2011; Carroll et al., 2013). In many retinopathies the fundus can appear unremarkable, yet cone waveguiding is disrupted and light detection is likely impaired (Birch et al., 1982; Smith et al.,

1988). Cone-targeted stimulation may become a tool for better characterization of disease progression and offer a way to evaluate the efficiency of novel treatments at the microscopic level in the living eye.

2.7 Acknowledgements

CHAPTER 3 – Functional Mapping of the Parafoveal Trichromatic Cone Mosaic

3.1 Abstract

Human color vision is initiated by light capture in the trichromatic cone mosaic and the subsequent comparison of these signals across space by the post-receptoral retinal circuitry. To probe this process *in vivo* on a single-cell scale requires knowledge of the topography of the long-, middle-, and short-wavelength sensitive cones (L-, M-, and S-, respectively), as well as an ability to drive individual photoreceptors in isolation. Near the fovea, these efforts are hampered by the optical imperfections that limit the resolution with which the retina can be visualized and stimulated. We sought to overcome these obstacles by imaging and stimulating the retina with a multi-wavelength adaptive optics scanning laser ophthalmoscope. A combination of selective bleaching and cone-resolved retinal densitometry was used to map the parafoveal trichromatic mosaic in two color-normal subjects, and these maps were compared to single-cone increment thresholds collected across the same receptor array under L-cone isolating conditions. We found good agreement between the objective and functional classification methods, but L-cone thresholds were widely distributed. Monte Carlo simulations revealed that L-cone thresholds tended to increase as the number of adjacent M- or S-cones increased. Optical modeling ruled out stimulus blur as the sole contributor to this elevation, suggesting that increased activity in the M- and/or S-cones engendered by the adapting field serves to inhibit nearby L-cones, either through cone-to-cone electrical coupling, feedback from inhibitory retinal interneurons, or adaptation of downstream circuitry that pools signals from multiple cones. These experiments challenge the notion that cones act as individualized light sensors *in vivo* under polychromatic conditions, and set the stage for future experiments aimed at unraveling the circuitry through which color vision is mediated.

3.2 Introduction

The manner by which the visual system is able to encode percepts of color has been of longstanding interest to the scientific community. In 1802, Young postulated the existence of three types of "sensitive filaments", one each for the three fundamental color sensations: red, green, and violet (Young, 1802). Experimental support for Young's trichromatic theory was later provided by Helmholtz, who demonstrated that normal observers could match any color simply by mixing three independent primaries in the proper proportions (Helmholtz, 1924). Thus, it became generally accepted that color vision is initiated by light capture in a mosaic of receptors comprising three subclasses, each with its own unique spectral sensitivity; the precise nature of these action spectra, however, remained beyond description. In the mid-20th century, Stiles (and later Wald) used steady adapting fields of varying wavelengths to probe sensitivity across the spectrum, and their evidence suggested the presence of three mechanisms with peak sensitivities located at 430, 540, and 575 nm, respectively (Stiles, 1959; Wald, 1964). In recent years, more sophisticated psychophysical approaches have led to improved estimates of the cone fundamentals (see Figure 3.1A-B; (Stockman et al., 1993a; Stockman and Sharpe, 2000)), which were found to be in general agreement with physiological recordings taken from individual cones in macaque and human retina (Baylor et al., 1987; Schnapf et al., 1987).
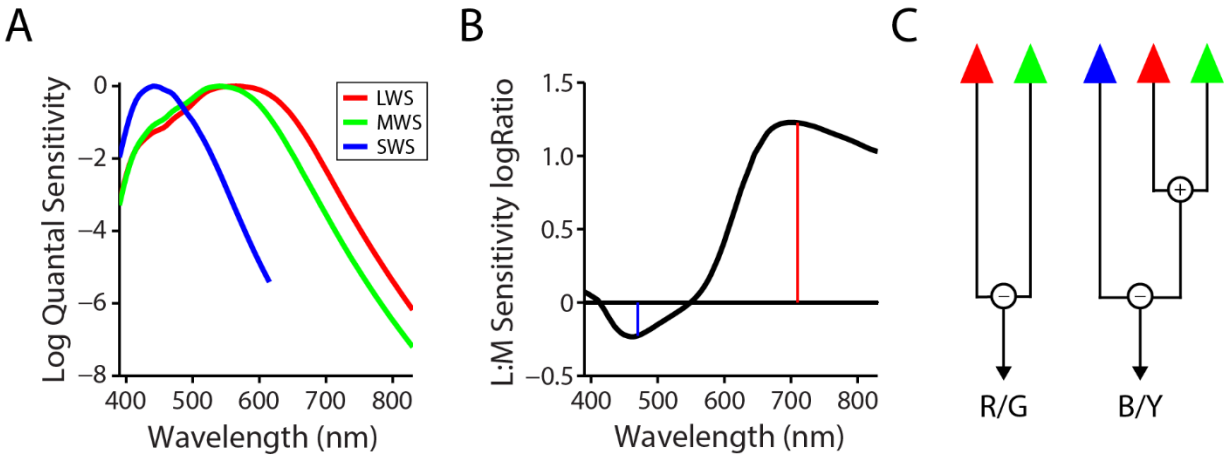
Figure 3.1| Basic properties of the trichromatic visual system. **A)** 2-degree Stockman-Sharpe cone fundamentals for L-, M-, and S-cones taken from Stockman and Sharpe, 2000. **B)** Ratio of L- to M-cone sensitivity as a function of wavelength, plotted on a $\log_{10}$ scale. Horizontal line indicates a sensitivity ratio of 1. Red line and blue lines (λ = 710 and 470 nm, respectively) denote stimulus and adaptation wavelengths selected to achieve the L-cone isolating conditions employed in this chapter. **C)** Schematic of retinal cone-opponent pathways thought to give rise to red-green and blue-yellow color dimensions. Red, green, and blue triangles correspond to L-, M-, and S-cones, respectively. In the red-green pathway, signals from L- and M-cones are opposed; in the blue-yellow pathway, excitatory S-cone signals are pitted against a summed L- and M-cone signal. In the retina, such input arrangements are observed in the response patterns of Type I midget (cf. Wiesel and Hubel, 1966) and small bistratified ganglion cells (cf. Dacey and Lee, 1994), respectively.

Although the Young-Helmholtz theory of trichromacy could account for many aspects of color vision, it was evident that some perceptual phenomena could not be easily assimilated into its framework. Most notably, Hering observed that certain color pairs—red-green and blue-yellow—tend to be perceived in a mutually exclusive fashion. These perceptual linkages formed the basis of his opponent theory of color vision, which was later formalized in a model by Hurvich and Jameson, who proposed that outputs from different cone classes are pitted against each other to give rise to the independent perceptual dimensions of red-green, blue-yellow, and black-white (Figure 3.1C; (Hurvich and Jameson, 1957)). Additional psychophysical evidence for the cardinality of these color mechanisms was provided by Krauskopf and colleagues (Krauskopf et al., 1982), and their results aligned nicely with physiological measurements of the spectral response properties in retinal ganglion cells (Gouras, 1968; De Monasterio and Gouras, 1975; Dacey and Lee, 1994; Field et al., 2010) and neurons of the lateral geniculate nucleus (LGN; (De Valois et al., 1966; Wiesel and Hubel, 1966; Derrington et al., 1984)).

Two parallel retino-geniculate pathways emerged from this work as leading candidates for the first stage of red-green and blue-yellow color vision in primates: midget ganglion cells, which oppose the signals of L- and M-cones and project to the parvocellular layers of the LGN (Dacey and Packer, 2003); and small bistratified ganglion cells, in which excitatory input from S-

cones is opposed against a summed L- and M-cone signal and sent to koniocellular layers of LGN (Dacey and Lee, 1994; Hendry and Reid, 2000). The former is generally considered the neurobiological substrate for red-green color vision, while the latter is thought to form the blue-yellow pathway, although hypotheses that refute, or otherwise refine, the standard model have been offered as alternatives (Rodieck, 1991a; De Valois and De Valois, 1993; Schmidt et al., 2014).

While the exact nature of the cone-driven circuitry underlying color vision remains a matter of debate, it is clear that the first constraint placed on this system is the arrangement and relative numerosity of its input elements, the three subtypes of cone photoreceptor. Over the past 30 years, this fact has motivated vision scientists to study the organization of the trichromatic mosaic. Early successes in this endeavor centered primarily on S-cones, which make up 5-8% of the cone mosaic (Curcio et al., 1991; Hofer et al., 2005b) and have unique morphological and histochemical signatures that facilitate their identification *in vitro* (de Monasterio et al., 1985; Ahnelt et al., 1987; Curcio et al., 1991). Owing to their distinct spectral sensitivity and relatively sparse arrangement, the functional properties of S-cones are more easily separable through psychophysical experimentation than their L- and M-cone counterparts (Brindley et al., 1966; Williams et al., 1981).

Understanding how L- and M-cones are distributed, however, has proven more challenging, in part because no major structural or histochemical differences exist between the two receptor types. The photopigments housed in L- and M-cones are 96% identical (Nathans et al., 1986), and as a consequence they have largely overlapping spectral sensitivities. A painstaking series of microspectrophotometric measurements of pigment transmittance in individual talapoin monkey foveal cones allowed the L- and M- subtypes to be distinguished (Mollon and Bowmaker, 1992), but the application of these methods is necessarily confined to post-mortem tissue, and yield no information about the post-receptoral circuitry through which cone signals propagate. More recently, functional properties of the L- and M-cone mosaic were inferred entirely from the outputs of a large population of retinal ganglion cells recorded on a multi-electrode array (Field et al., 2010). While such cutting-edge electrophysiological approaches have enhanced our understanding of the fine-scale functional connectivity in the excised retina, technical limitations restrict their use to more peripheral eccentricities where ganglion cells are arranged in a monolayer.

Lacking the physiological tools capable of efficiently parsing L- and M-cones at eccentricities nearer the fovea, investigators interested in the properties of the trichromatic mosaic in the central retina turned to psychophysics, with evidence accumulating over the course of 40 years suggesting an average L:M cone ratio of approximately 2-to-1 (De Vries, 1946; De Vries, 1949; Rushton and Baker, 1964; Vos and Walraven, 1971; Walraven, 1974; Smith and Pokorny, 1975; Cicerone and Nerger, 1989a). Direct visualization of L-, M-, and S-cones remained elusive until the late 1990s, when David Williams and Austin Roorda combined cone-resolved adaptive optics absorptance imaging with selective photopigment bleaching to generate the first maps of the trichromatic cone mosaic in the living eye (Roorda and Williams, 1999). These densitometric methods were later refined and applied to a larger population, revealing a striking variability in

L:M cone ratios across a group of individuals with otherwise normal color vision (Hofer et al., 2005b). Estimates of L:M ratio derived from adaptive optics images show good agreement with those derived from flicker electroretinograms collected over the central 70 degrees (Brainard et al., 2000; Carroll et al., 2002; Hofer et al., 2005b), suggesting that the wide phenotypic variation in cone ratio observed in the study of Hofer and colleagues is unlikely to arise from experimental artifact.

The remarkable heterogeneity in the ratios of L- and M-cones in the normal human fovea raises a number of fundamental questions about the neural circuitry mediating color vision: What are the rules governing the fate and arrangement of L- and M-cone progenitors during development (Xiao and Hendrickson, 2000; Neitz and Neitz, 2011)? What level of cone-type selectivity in the color-opponent retino-geniculate pathways is required to account for normal human color experience (Lennie et al., 1991; Reid and Shapley, 1992)? What neural normalization mechanisms are needed to produce a relatively consistent color experience across individuals when faced with input elements that may vary widely in their relative proportions (Neitz et al., 2002)? How does the arrangement of the trichromatic mosaic influence the color percepts elicited by stimulating cones in isolation (Hofer et al., 2005a; Brainard et al., 2008)?

Addressing these questions in humans requires tools capable of characterizing the trichromatic mosaic with cellular resolution, both from a structural (i.e. densitometric) and functional viewpoint. The goal of the experiments described in this chapter was to generate a map of the parafoveal L-, M-, and S-cones using adaptive optics densitometry and compare it to one derived entirely from the psychophysical performance of individual cones within the same array. The motivation for doing so was two-fold: first, any agreement between objective and subjective methods may be taken as additional validation of the adaptive optics densitometric approach to identifying cone type; second, understanding how single-cone performance may be shaped by its surrounding milieu may provide some insight into the nature of the post-receptoral circuitry through which cone signals propagate.

3.3   Methods

3.3.1   Cone-resolved Retinal Densitometry with AOSLO

We used a multi-wavelength AOSLO to characterize the trichromatic cone mosaic in two male subjects with normal color vision (ages: 31 and 36). A full description of AOSLO imaging can be found in Chapters 1 and 2 of this document; only the pertinent details of the adaptive optics densitometry protocol will be described in this section. The approach to identifying L-, M-, and S-cones was adapted from that employed in the studies of Roorda and Williams and Hofer et al., with the most notable difference being that an AOSLO was used in place of the original flood-illuminated AO ophthalmoscope (Roorda and Williams, 1999; Hofer et al., 2005b). AOSLO offers a number of advantages over flood-based systems, including improved image contrast and video-rate imaging, but objective cone classing with AOSLO has not been demonstrated until quite recently (Sabesan R, et al. IOVS 2014; 55 ARVO E-Abstract 1652).

Subjects were dark adapted for a period of 3 to 5 minutes, during which the photopigment was allowed to regenerate to a level corresponding to roughly 90% of its maximum optical density (Rushton and Henry, 1968). To identify S-cones, wavefront correction was engaged and a patch of dark-adapted retina 1.5 degrees temporal to the fovea was imaged with a bright pulse of 543 nm light (bandwidth: ± 13 nm; dose: 3 to 6 microwatts at the cornea), the intensity of which was sufficient to bleach the L- and M- photopigment over the course of roughly 1 second. The wavelength of our imaging beam was chosen because it affects changes in the L- and M-cone opsins with roughly equal efficacy, while remaining effectively unabsorbed by S-cones (Stockman and Sharpe, 2000).

The effect of pigment bleaching by our imaging beam manifests as an increase in pixel intensity over the course of the AOSLO imaging video, with most cones starting dim and eventually rising to a plateau, at which point they are considered fully-bleached. Bleaching videos were stabilized offline using custom software (Stevenson and Roorda, 2005), and the intensity of each cone was tracked over time across a 3-by-3 pixel sampling window. For each cone, absorptance, A, was calculated based on Equation 3.1, where I_D and I_B are the cone intensities in the dark-adapted and fully-bleached states, respectively:

$$A = 1 - \frac{I_D}{I_B} \tag{3.1}$$

Arranging the cone absorptances measured immediately following dark adaptation into histograms reveals two distinct data clusters, a large one exhibiting relatively large absorptances and a second, smaller distribution representing cones showing little or no absorptance (Figure 3.2 A, D). The former corresponds to the L- and M-cones, while cones falling into the latter category are presumed to be S-cones and excluded from further analyses.

To distinguish between L- and M-cones, a selective bleaching step was inserted between the dark adaptation and bleaching stages described above. Selective bleaching wavelengths for L- and M-cones were chosen from points in the spectrum where the differences in their sensitivities were maximal (red and blue lines in Figure 3.1B): for L-cones, a 710 nm selective bleach (dose: 20 µW; duration: 10 seconds; field size: 1.2 x 1.2 degrees) applied directly before the imaging video reduces L-cone absorptance; a short-wavelength bleach (Wratten filter #47B; λ_{peak} = 470 nm) diminishes the M-cone absorptance signal preferentially (dose: 0.4 microwatts; duration: 60 sec). A plot of absorptance over the two bleaching conditions is shown in Figure 3.2 B, E. These data were grouped according to their polar angle, revealing histograms with two data clusters (Figure 3.2 C, F). The data were then fit by the sum of two Gaussians (black line), with the point of intersection of the two component Gaussians (red and green lines) taken as the line of demarcation between the two cone subtypes. Pseudocolor retinal mosaics (Figure 3.2 G, H) were generated according to the classification criterion and used as a basis of comparison for the increment threshold measurements described in the next section.
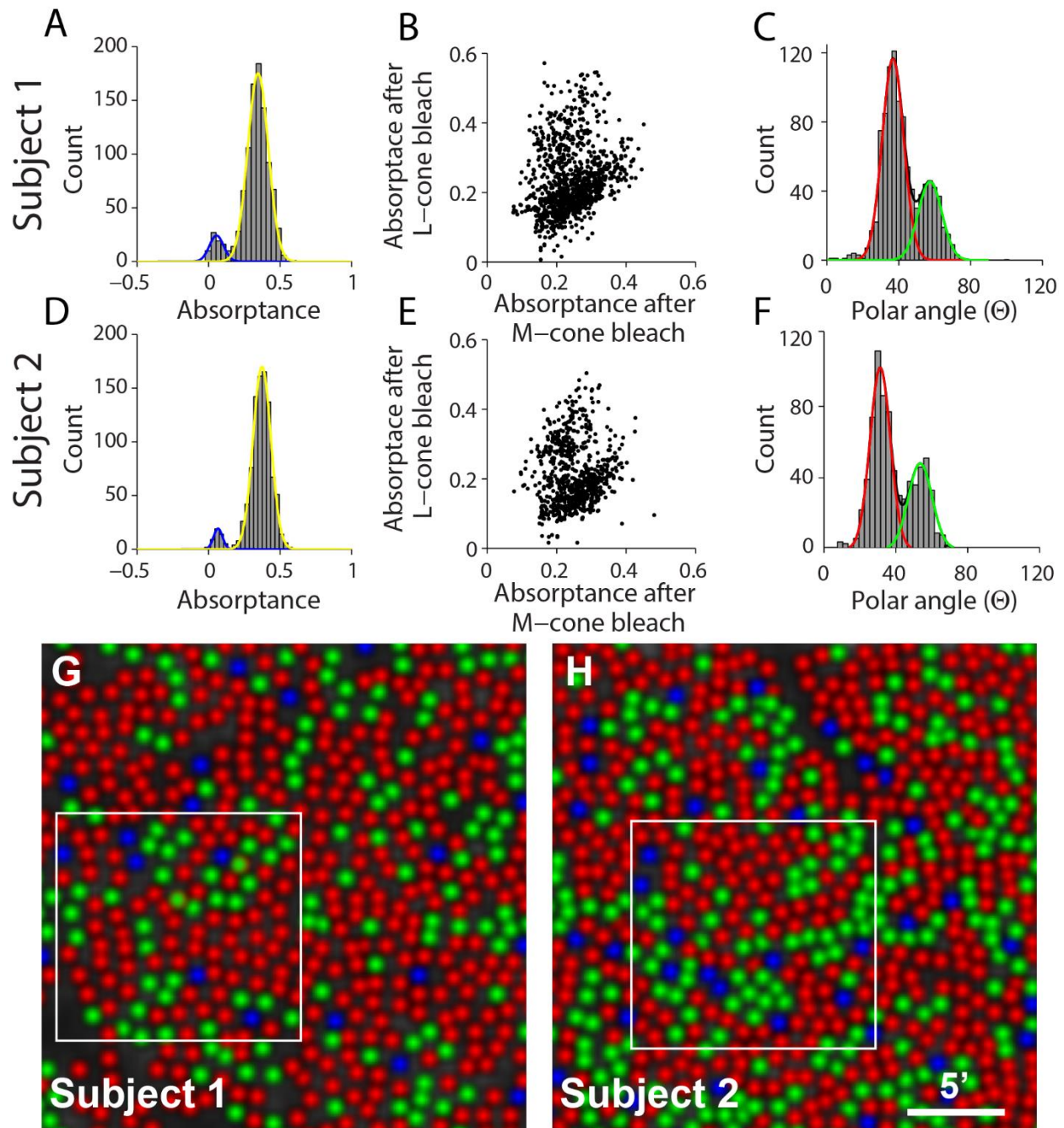
Figure 3.2|Trichromatic mapping with adaptive optics scanning laser ophthalmoscopy. (**A**, **D**) Cone absorptance histograms following dark adaptation reveals S-cone and L-/M-cone clusters (blue and yellow lines, respectively). (**B**, **E**) Cone absorptance measured following L-cone and M-cone-selective bleaching. (**C**, **F**) Histogram of polar angle for each cone plotted in panels **B** and **E**; classification angle (Θ) delineating L- and M-cones is defined as the point of overlap of two component Gaussians (red and green lines) that yield the best sum-of-Gaussians fit (black line) to the entire histogram. (**G**, **H**) Pseudocolor images of the L-, M-, and S-cone mosaic based on the classification angle derived from panels **C** and **F**. White boxes outline region selected for functional testing (see Figure 3.4). (Data courtesy of Ramkumar Sabesan, University of California, Berkeley.)

3.3.2 Generating Functional Maps of the Trichromatic Mosaic

In each subject, a contiguous array of cones located within the cone mosaic classified by adaptive optics densitometry was selected for single-cone increment threshold testing. The general approach to measuring increment thresholds with AOSLO is described in the previous chapters. Targeted cones were selected manually in a high-magnification view of the imaging and stimulus delivery software interface (Chapter 1), and care was taken to avoid cones stationed in the shadows of retinal capillaries (Tam et al., 2010). Transverse chromatic aberration was measured before and after each block of trials, and a bite bar was used to prevent shifts in pupil position during testing.

Thresholds were measured under L-cone isolating conditions (Yeh et al., 1989), where the subject's task was to detect a 0.45 arcmin square stimulus (λ = 710 nm) presented for 125 μsec against a background comprising three elements: the dim, infrared imaging raster; 710 nm AOM leak through the stimulus channel (luminance = 2.5 cd/m^2); and, a short-wavelength background generated by placing a filter in front of a broadband incandescent source presented in Maxwellian view (Wratten #47B; λ_{peak} = 464 nm; luminance: 50 cd/m^2; diameter = 2⁰). A schematic of the subject's view during testing is shown in Figure 3.3A. Cone contrasts for our conditions were calculated based on the stimulus wavelength and the composition of the background, resulting in a predicted L-to-M sensitivity ratio of 24-to-1 (Cole and Hine, 1992); S-cones are not expected to contribute to detection under these conditions, and M-cones were about 1.5 times more adapted than L-cones. Consistent with previous chapters, thresholds were expressed on a linearized scale of arbitrary units (a.u.), with a value of zero indicating the presence of the background alone and a value of 1.0 corresponding to the upper limit of stimulus modulation; thus, if the average L-cone threshold has a value above 0.05 a.u., one might expect M- and S-cone thresholds to register beyond our modulation limit.

During a given run, up to three cones were selected for testing, and cone thresholds were assessed in parallel using randomly-interleaved, 20-trial QUEST staircases guided by a yes-no response paradigm (Watson and Pelli, 1983). All thresholds measured under L-cone isolating conditions were repeated at least twice. For cones exhibiting high thresholds under these conditions, thresholds were re-measured with the adapting background switched off—a recovery of sensitivity supported the interpretation that elevated thresholds were due to the effects of adaptation and not the result of the occasional dysfunctional cone (Figure 3.3B).

3.3.3 Data Analysis and Modeling

Tested cones were grouped according to their average threshold and plotted in a histogram (Figure 3.4 E-F), with thresholds measuring at or above our stimulus modulation limit placed in a single group (see rightmost bar in Figure 3.4 E-F). A functional classification criterion was positioned somewhere along the abscissa of the threshold histogram, such that cones to the left would be classified as L-cones and cones to its right would fall into the non-L category (i.e. M- or S-cones)—the position of this cut off was selected to maximize the agreement between the densitometric and functional classification using Cohen's kappa coefficient, a statistic of

agreement for categorical data (Cohen, 1968). No test was applied to distinguish between M- and S-cones; however, cones falling into the non-L function category were labeled according to type for the purposes of display.
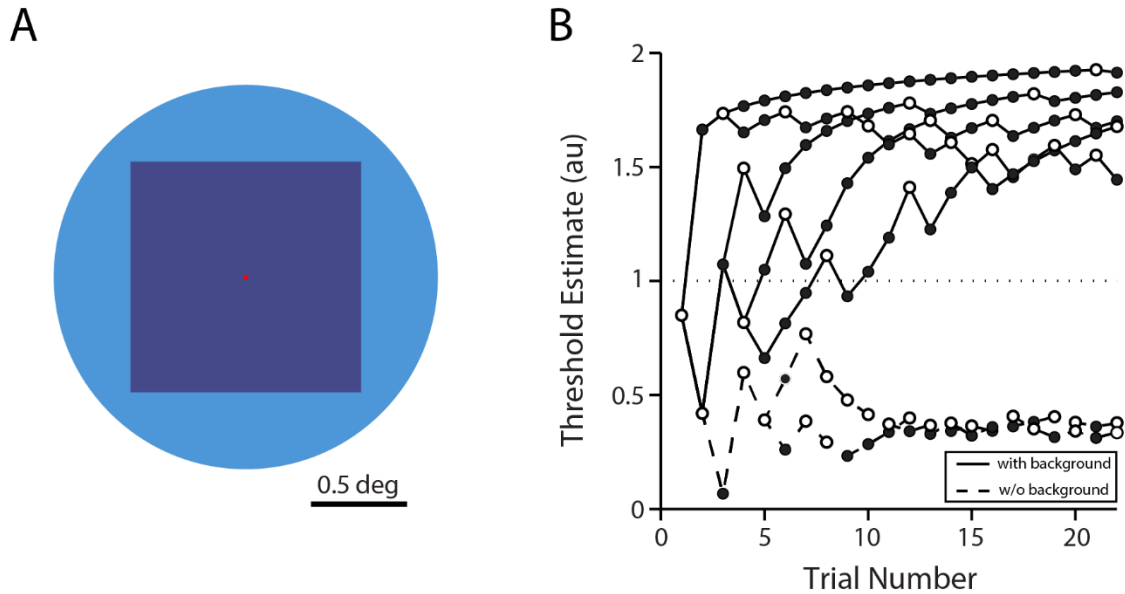
Figure 3.3| L-cone isolating conditions elevate M-cone thresholds. **A)** Schematic of L-cone isolating conditions from the subject's perspective. A 2 degree circular adapting field (Wratten filter #47B; peak λ = 470 nm) presented in Maxwellian view is used to counterbalance adaptation induced by AOM leak in the stimulus channel; blue field adapts M- and S-cones preferentially, leaving L-cones approximately 20 times more sensitive to the 710 nm test probe (small red square). **B)** Example data collected from an M-cone at 1.5 degrees eccentricity. Staircase plots illustrate staircase convergence onto a threshold estimate as trial number increases. Solid lines indicate repeated measures of threshold on the targeted M-cone with the adapting field in place, with thresholds falling beyond the upper modulation limit of the AOM (horizontal dotted line); dashed lines denote staircase functions collected on the same cone when the background was switched off. Open and filled circles correspond to subject responses of "seen" and "unseen", respectively.

To test the hypothesis that the threshold measured in a given L-cone might be influenced by the spectral identities of its surrounding cones, threshold data for all L-cones were binned according to the number of directly adjacent M- and S-cones. The average threshold for each group is plotted in Figure 3.5. Monte Carlo simulations of the adjacent cone effect were carried out to test the likelihood that the relationship between L-cone threshold and neighboring cone type might arise randomly. This was done by shuffling the mosaic of tested cones and repeating the neighborhood analysis described earlier in this paragraph. Multiple iterations (n = 10,000) of this process yields a distribution of the average threshold for each category in Figure 3.5.
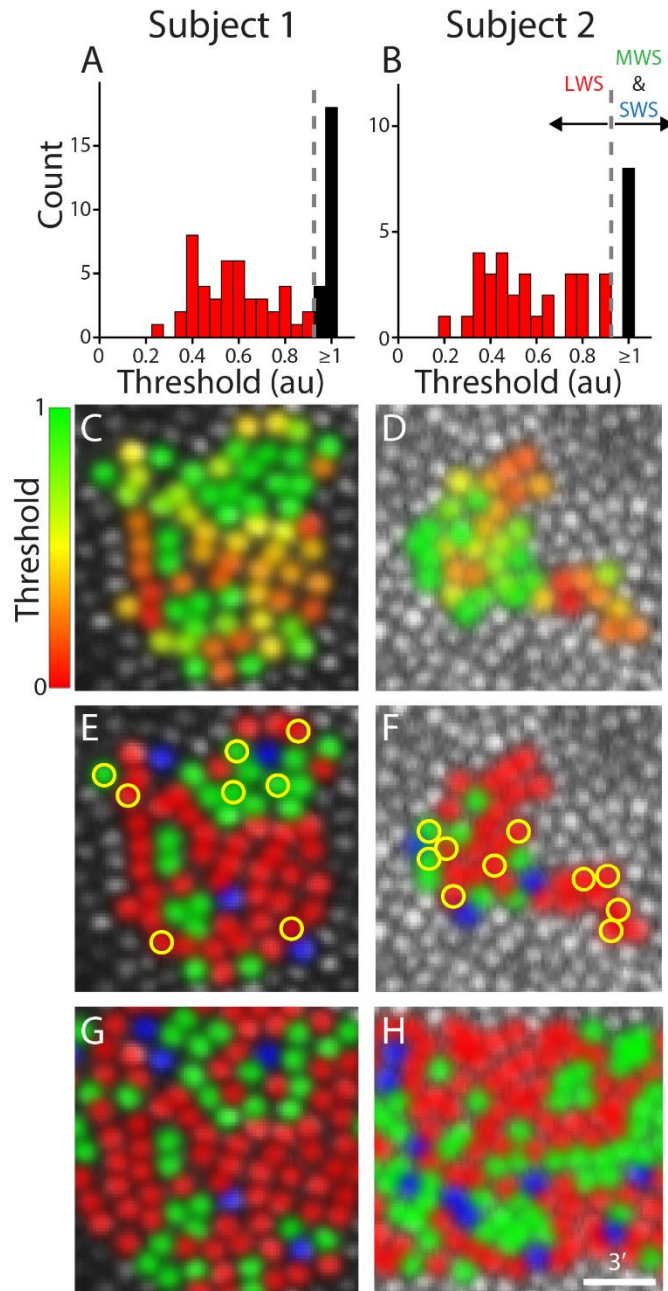
Figure 3.4| Functional cone classing in the living eye. **(A**, **B)** Histogram of mean increment thresholds for the contiguous array of cones tested under L-cone isolating conditions. Grey dashed line represents the threshold cutoff that produced the best agreement between objective and subjective classification methods; for this subject, cones exhibiting a mean threshold less than 0.95 arbitrary units were classified as L-cones (see panels **E** and **F**). **(C**, **D)** Increment threshold data for an array of 67 cones collected under L-cone isolating conditions (marker color denotes threshold values on an arbitrary scale from 0 to 1). **(E**, **F)** Functional cone classification based on increment thresholds from panels **C** and **D**. Yellow circles mark cones (n =18) whose functional measures were inconsistent with their objectively-determined cone class. **(G**, **H)** Pseudo-color images of the trichromatic cone mosaic generated with AO imaging and retinal densitometry at ~1.5 degrees eccentricity. Red, green, and blue labels correspond to L, M, and S cones, respectively.

43

Finally, a model of light capture similar to the one described in the previous chapter was constructed to examine relationship between threshold, unaccounted-for stimulus spread, and the spectral composition of the local receptor milieu (Figure 3.6). As before, two-dimensional Gaussian light-collecting apertures representing individual cones were arranged in a hexagonal pattern according to normative cone spacing data for the test eccentricity (Curcio et al., 1990). The size of each aperture was assumed to be 50% of the inner segment diameter at the same eccentricity (Hirsch and Curcio, 1989; MacLeod et al., 1992), and its light capture efficiency was scaled by its expected sensitivity under the test conditions. Seven model cone arrays were generated, all featuring a central L-cone, but with anywhere from zero to six L-cones in the surrounding ring. A spatio-temporal representation of our test stimulus was calculated from diffraction and the expected noise in stimulus delivery, centered on the central L-cone, and filtered by each model array. Predicted thresholds (Figure 3.6 panel I) for each model array were calculated based on the assumption that a fixed number of quanta must be captured to reach threshold, such that the product of light capture efficiency and incident quanta (i.e., the height of our stimulus increment) would remain constant. Additional optical defocus was introduced to the stimulus representation until the slope of the predicted thresholds across the range of model arrays matched that observed in our data (see Figure 3.5).

3.4   Results

The adaptive optics densitometry results for our two subjects are shown in Figure 3.2. For both subjects, S-cones accounted for roughly 5% of all cones analyzed, consistent with previous histological and image-based findings at this eccentricity (Curcio et al., 1991; Roorda and Williams, 1999; Hofer et al., 2005b). The L:M cone ratio for our two subjects was 2.1:1 and 1.8:1, respectively—well within the range previously reported for individuals with normal color vision (Hofer et al., 2005b). The classification error for the densitometric approach was estimated by examining the overlap of the component Gaussians in Figure 3.2 E-F and found to be 4.1% and 3.2% (S1 and S2, respectively), consistent with the findings of previous investigators (Roorda and Williams, 1999; Hofer et al., 2005b).

Single-cone increment thresholds were measured for a total of 109 cones across the two subjects. An increment threshold classification criterion of 0.90 (gray dashed line in Figure 3.4 A-B) yielded maximal agreement between the densitometric and functional classification approaches (Subject 1: 88% observed agreement, Cohen's kappa = 0.74, p < 0.0001; Subject 2: 74% observed agreement, Cohen's kappa = 0.4493, p = 0.016). For both subjects, nearest neighbor analysis (Figure 3.5) revealed that thresholds associated with L-cones positioned in a cluster of M- and S-cones were nearly double those measured from L-cones surrounded entirely by cones of like type. By contrast, Monte Carlo simulations of this analysis demonstrate, on average, no relationship between L-cone thresholds and neighboring cone type (open circles, Figure 3.5), although the relative infrequency with which receptor configurations on either extreme of Figure 3.5 occur results in substantially wider error estimates than those associated with more common arrangements.
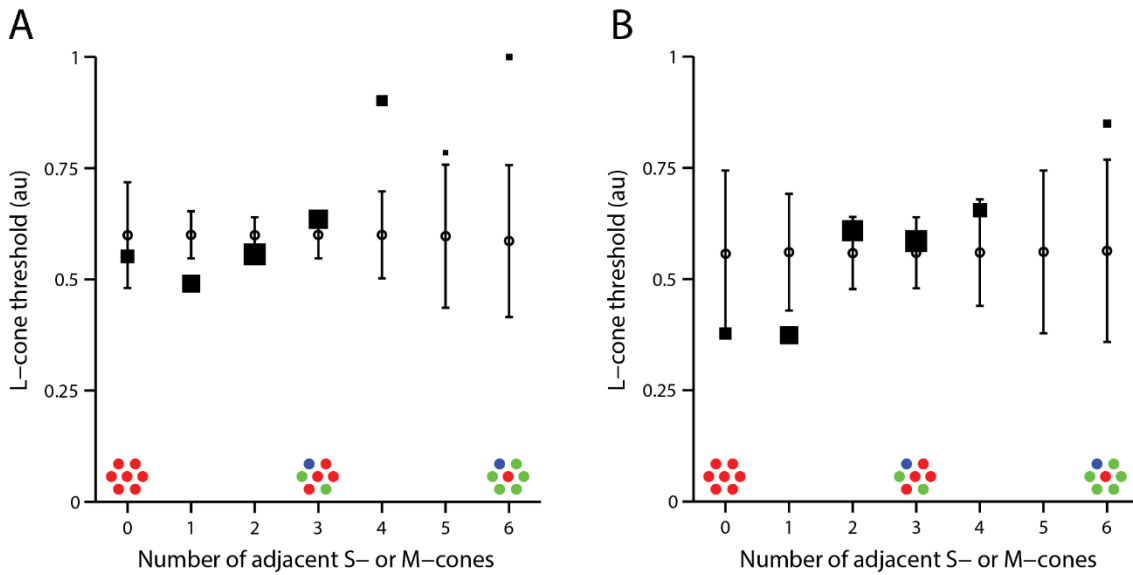
Figure 3.5| The influence of neighboring cone type on measured L-cone thresholds. L-cone thresholds were grouped according to the number of immediately adjacent M- and S-cones, with the mean thresholds for each configuration group plotted as black squares; the area of each marker is proportional to the number of occurrences of that configuration within the subject's mosaic. Panels **A** and **B** refer to Subject 1 and 2, respectively. Monte Carlo simulation (n = 10^4 iterations) was performed by randomly permuting cone locations within the array and repeating the neighborhood analysis as described above. The average group-mean threshold across all simulations is plotted as open circles (error bars: ± 1 standard deviation).

The results of the light capture modeling for our test conditions are shown in Figure 3.6. After accounting for diffraction, the size and wavelength of our stimulus, the adaptation state of L- and M-cones, and additional spatio-temporal spread introduced by errors in stimulus delivery, we were able to generate predicted thresholds for L-cones while varying the spectral makeup of the surrounding cones, while also manipulating the amount of additional blur that may be present in our stimulus. To facilitate comparison across blur conditions, the highest predicted thresholds for each defocus condition were normalized. With zero residual defocus, we estimated that purely optical effects will serve to increase thresholds by roughly 20% across our configuration categories. Applying the 0.05 diopter residual blur calculated from the cone-gap experiments in Chapter 2, we observed a 33% increase across the same span of model arrays. To reach the nearly 100% increase in threshold shown in Figure 3.5 required the introduction of 0.10 diopters of unaccounted-for blur, which, in the typical eye, corresponds to a focal shift of roughly 30 microns in the axial dimension, a distance which is approximately equivalent to outer segment lengths measured from mature parafoveal cones (Yuodelis and Hendrickson, 1986).
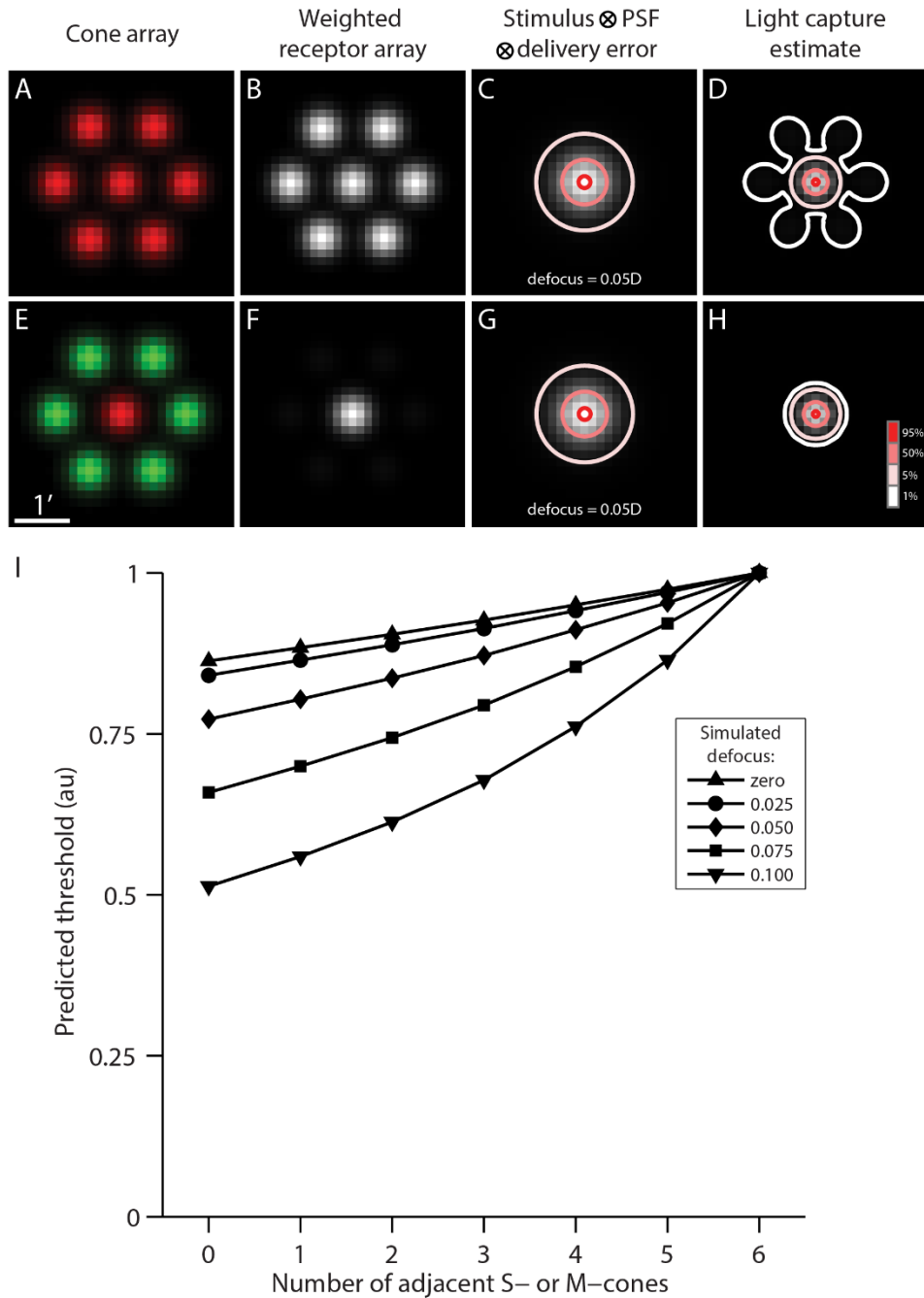
Figure 3.6| Light capture modeling in the trichromatic cone mosaic. (**A**, **E**) Example model cone mosaics featuring a central L-cone and surrounded entirely by either L- or M-cones (panel **i** categories "0" and "6", respectively). Scale bar in **E** applies to all panels. (**B**, **F**) Gaussian light collection apertures weighted by expected cone sensitivity under L-cone isolating conditions. (**C**, **G**) Retinal stimulus representations generated by successively convolving our 3x3 pixel stimulus with a point spread function (PSF) and an estimate of stimulus delivery error (Gaussian standard deviation = 0.5 arcmin). Representations shown here were generated with PSFs featuring 0.05D of residual defocus, consistent with the findings presented in Chapter 2. Contour lines denote fall off in light intensity as a percentage of peak height. (**D**, **H**) Light capture estimates generated by filtering our stimulus representation with the weighted receptor array. (**I**) Predicted thresholds across the range of cone arrangement categories with varying levels of residual stimulus blur in our stimulus representation.

46

3.5 Discussion

Under L-cone isolating conditions, we used a single-cone increment threshold approach to identify likely L-cones in the parafovea. Comparing these results to objective classification obtained via adaptive optics retinal densitometry, we found statistically significant agreement across a contiguous array of cones in both subjects, with 83% of tested cones performing according to spectral type. Given that the error associated with adaptive optics densitometry is estimated to be around 5% (Roorda and Williams, 1999; Hofer et al., 2005b), our functional classification approach appears to have performed well, despite the formidable technical and optical hurdles involved with attempting to drive individual photoreceptors in isolation this close to the fovea. In addition to the support provided by flicker electroretinography (Carroll et al., 2002), these results can be taken as further confirmation of the validity of the adaptive optics densitometry approach to cone classification.

A number of factors could have influenced or otherwise corrupted our results. For instance, the adaptive optics densitometric technique classifies S-cones entirely by exclusion—that is, cones which do not show responsiveness to the 550 nm imaging bleach after dark adaptation are assigned to the S-cone group. While this approach has generally resulted in S-cone densities and packing arrangements in accordance with histological estimates taken from both man (Curcio et al., 1991) and monkey (de Monasterio et al., 1985; Roorda et al., 2001), it remains possible that the occasional L- or M-cone features morphological anomalies in its outer segment that impair its ability to reflect light normally, or its reflection may stem entirely from the junction between the inner and outer segment. After examining a series of images collected over many months from a group of healthy subjects in our lab, we have noticed a small number of cones that remain persistently dark, failing to exhibit the normal reflectance fluctuations observed in most cones across imaging sessions (Pallikaris et al., 2003). Interestingly, single-cone increment thresholds collected from these sites are indistinguishable from those taken from nearby, normally-reflecting cones, suggesting the reflectance properties of a cone are not entirely predictive of its functional state (Bruce KS, et al. IOVS 2014; 55 ARVO E-Abstract 4544).

Another possible source of discrepancy between the functional and densitometric classification results is optical blur. Upon examining the non-random clumping of L- and M-cones observed in roughly in half of their subjects, Hofer and colleagues postulated that optical blur could lead to erroneous classifications in cases where L- and M-cones are surrounded by cones of opposite type (Hofer et al., 2005b). They reasoned that, since a small fraction of the reflected light attributed to a cone may actually stem from its neighbors, an M-cone situated in an L-rich region is more likely to masquerade as an L-cone than an M-cone residing in a more diverse neighborhood. Thus, if densitometric classification errors arising from optical blur were undermining our data, one would expect functional misclassifications to occur at cones surrounded by cones of like type in the densitometric image (i.e., in clustered regions). Our adjacent cone analysis suggests the opposite, demonstrating functional misclassifications were more likely to occur at cones featuring three or more receptors of opposite type in their immediate surround, as defined by densitometry (Figure 3.5).

Although optical blur during densitometry cannot account for the functional classification errors we observed, stimulus blur during our psychophysical task could be a contributing factor. We constructed a simple model of light capture in the fovea for a range of L- and M-cone configurations (Figure 3.6), based largely on the model presented in Chapter 2. After accounting for diffraction, stimulus size and wavelength, the size and spacing of individual receptors at our test eccentricity, expected relative L- and M-cone sensitivities, and the average stimulus delivery uncertainty for our system, we estimated that neighboring cones at this eccentricity receive some stimulus light and, thus, could contribute modestly to detection, even with a perfectly-corrected stimulus. Adopting an estimate of equivalent defocus of 0.05 diopters, which best described the data collected in Chapter 2, we find that optical factors could explain about half of the elevation we observe in our adjacent cone analysis (Figure 3.5); to fully account for the rise in L-cone threshold resulting from increasing the number of M-cones in a receptor's surround, the stimulus blur added to our model had to be doubled to 0.10 diopters. Blur of this magnitude is nearly double the axial resolution of the AOSLO, and adjusting system defocus by this amount markedly reduces the quality of images collected in the stimulus channel, making it unlikely to be this high during data collection.

While the exact spatial extent of our stimulus on the retina is a likely contributor to the adjacent-cone interactions we observe in our data, we speculate that neural factors may also play a role. Center-surround receptive field arrangement has long been considered an organizing principle of early visual processing, and is found in the response patterns of retinal ganglion cells and LGN neurons in a number of species (Barlow, 1953; Hartline and Ratliff, 1957; Hubel and Wiesel, 1960; Wiesel and Hubel, 1966). The adapting field used in this study engendered relatively higher activity in M-cones relative to L-cones, by a factor of about 1.5, and it is possible that this enhanced activity may serve to inhibit the sensitivity of nearby L-cones. Electrophysiological recordings from cone photoreceptors reveal that a cone's response to the onset of a steady background is characterized by a sharp increase in membrane current, followed by a slower return to a steady state at a level corresponding to 50% of the peak response amplitude (Normann and Perlman, 1979; Valeton and van Norren, 1983; Schnapf et al., 1990). Thus, it is expected that our background would result in relatively higher resting current for M-cones relative to L-cones; the remainder of this discussion will consider the routes through which this signal could travel to inhibit nearby L-cones, beginning in the photoreceptor layer and moving downstream through the visual circuitry.

A simplistic view of the retina begins with an array of densely-packed photoreceptors, which capture photons and feed their signals forward into the visual circuitry for comparison or combination. This picture—in which cones act as independent light sensors—is not well-founded: in reality, intercellular coupling between neighboring cones is prevalent (Baylor et al., 1971; DeVries et al., 2002). It has been suggested that the benefits gained from reducing noise through signal averaging across neighboring cones outweigh the potentially deleterious effects of neural signal spread on high-acuity and chromatic vision (Lamb and Simon, 1976; Tessier-Lavigne and Attwell, 1988; DeVries et al., 2002). In the primate retina, L- and M-cones couple indiscriminately via gap junctions, and this connectivity appears to be restricted to the central cone and its immediate surrounding ring (DeVries et al., 2002; Hornstein et al., 2004). Gap

junction-mediated signal transfer between receptors is linear and temporally bandpass, with maximal signal transfer occurring near 20 Hz (Hornstein et al., 2004). Computational modeling of the electrical network in the photoreceptor layer under uniform illumination predicts a cone receptive field containing a central peak and a surrounding ring of lower amplitude (~5% of central peak) contributed by its immediate neighbors (DeVries et al., 2002). According to the analysis of DeVries and colleagues, approximately 24% of the activity arising from an individual L-cone under uniform illumination originates in its neighbors. If the L-cone in question is surrounded by 6 M-cones, each exhibiting 1.5 times greater activity, the baseline activity of the central L-cone would be increased by 12% relative to the same L-cone surrounded by receptors of like type, and one would expect its threshold to be increased as a result of its slightly elevated adaptation state.

A second way in which M-cone activity could influence thresholds measured from nearby L-cones is through inhibitory retinal interneurons. Horizontal cells are one viable candidate, as they are thought to be the neural pathway through which receptive field surrounds in most major classes of retinal ganglion cells are established (Mangel, 1991; Dacey et al., 1996; Dacey et al., 2000; McMahon et al., 2004; Packer et al., 2010; Crook et al., 2011). Photon capture in cones triggers hyperpolarization in the inner segment and a subsequent decrease in glutamate release into the synapse. Cone pedicles contact both cone bipolar cells, which propagate signals forward, and horizontal cells, which send inhibitory feedback signals laterally through the retina onto nearby cones. Two types of horizontal cells are found in primate retina: H1 cells, which receive mixed input from L- and M-cones; and H2 cells, which are connected to all three cone types but whose input is derived predominately from S-cones (Dacey et al., 1996; Dacey et al., 2000). The spatial extent of lateral signal spread through the horizontal cell network is governed by ambient light levels, and, in comparison to gap junctions, the temporal dynamics of horizontal cell feedback signals are relatively sluggish (Smith et al., 2001; Lee et al., 2003). Thus, it remains possible that steady-state M-cone activity evoked by the adapting field could feed back through the H1 horizontal cell network onto nearby L-cones, thereby causing a reduction in their sensitivity.

Post-receptoral adaptation of downstream circuitry that pools signals over multiple cones represents yet another explanation for the adjacent cone effect we observed in our data. Adaptive mechanisms allow the visual system to remain responsive over an enormous range of ambient illuminations (Shapley and Enroth-Cugell, 1984), and there is abundant physiological and psychophysical evidence that these processes are active at multiple stages in the visual pathway, including cone photoreceptors (Boynton and Whitten, 1970; Valeton and van Norren, 1983; Dunn et al., 2007) as well as at post-receptoral sites (Pugh and Mollon, 1979; Stromeyer et al., 1985; Purpura et al., 1990; Yeh et al., 1996; Dunn et al., 2007). In the fovea, detection of a small, brief spot of light is influenced markedly by the presence of a concentrically-arranged circular background (Westheimer, 1967). The effect of the background on probe detection is size-dependent: for small backgrounds (5 arcmin or less), thresholds rise steadily with increasing diameter; further increases in patch size elicit a gradual return to normal sensitivity. It is thought that, up to a certain diameter, the additional illumination provided by the background patch serves to elevate the adaptation signal arriving at a downstream site, which

presumably integrates input across that region of retina. Further expansion of the background engages more distal inhibitory mechanisms acting laterally on the retinal locus, lowering its adaptation state and restoring sensitivity.

Elevated thresholds measured from L-cones positioned amongst M-cones can be interpreted in a similar framework, provided the signal driving post-receptoral adaptation in the pathway mediating detection is pooled over multiple cones. For the purposes of this discussion, let us presume that the site of post-receptoral adaptation is the retinal ganglion cell (Purpura et al., 1990; Yeh et al., 1996). Under our cone-isolating conditions, the adapting field will evoke non-uniform steady-state activity across the variegated trichromatic cone mosaic, with each cone submosaic adapted according to its respective sensitivity to the background. If the ganglion cell class mediating detection for our task receives input from predominately one cone, the spatial variation in ganglion cell adaptation state will be inherited directly from the non-uniform activity in the underlying cone mosaic, and the effect of downstream adaptation on single-cone-driven thresholds ought to be similar for all cones belonging to the same subclass (e.g. L-cones). In the event that detection is governed by a pathway with coarser spatial sampling, the adaptational state of each ganglion cell would depend on the relative number of L- and M-cones from which it pools signals, with a ganglion cell sampling an L-cone rich patch of retina receiving a lower adapting signal than a similar cell integrating over a locus containing mostly M-cones. An L-cone feeding into the former would be expected to have better sensitivity than an L-cone whose signals are fated to propagate through the latter.

Thus, interpreting our data through the lens of post-receptoral adaptation requires a consideration of the sampling properties of the retino-geniculo-cortical channel through which detection in our task is likely mediated. Anatomical findings indicate midget ganglion cells may account for as much as 95% of the total ganglion cell population at our test eccentricity (Dacey, 1993). It was long presumed, based on both anatomical and psychophysical evidence, that midget ganglion cells possess receptive field centers driven by a single cone at eccentricities up to around 5 degrees (Green, 1970; Enoch and Hope, 1973; Williams and Coletta, 1987; Curcio and Allen, 1990; Dacey, 1993). Only recently has histological and psychophysical data emerged suggesting cone convergence may commence much closer to the fovea, perhaps as close as 1 degree eccentricity (Drasdo et al., 2007; Rossi and Roorda, 2010). If midget ganglion cells are mediating detection in our task, we might expect their receptive field centers to comprise anywhere from a single cone up to perhaps 5 cones, based on known cone densities and current estimates of parafoveal midget ganglion cell density (Curcio et al., 1990; Drasdo et al., 2007). If, on the other hand, detection proceeds through the parasol-driven magnocellular channel, downstream adaptation might reflect the pooled signal of anywhere from 50 to 100 cones (Dacey and Petersen, 1992). In the case of the latter, differential downstream adaptation is unlikely to play a major role, since each neuron in the ganglion cell mosaic would sample from enough cones that its input demographics ought to reflect the average L:M ratio in the retina.

From a functional perspective, a wealth of physiological evidence supports the magnocellular visual pathway as the basis for detecting stimuli of low spatial and high temporal

frequencies, owing to the larger receptive fields and faster conduction velocity of parasol ganglion cells that constitute its input; by comparison, the parvocellular pathway is thought to be more sensitive to chromatic modulation and stimuli of higher spatial frequency (Merigan et al., 1991; Merigan and Maunsell, 1993). It therefore remains unclear which pathway might govern detection of our small, briefly-presented stimulus. In the fovea, increment thresholds measured on a white background for small, brief monochromatic stimuli of different wavelengths resulted in detection contours across the spectrum resembling the photopic luminous efficiency function (King-Smith and Carden, 1976). The neural substrate of the so-called "luminance channel" is thought to be parasol ganglion cells, whose response properties resemble human performance on flicker photometry (Lee et al., 1988). For our task, the subjects perceived the test flash as achromatic on virtually all trials, and recent work in our lab has shown chromatic percepts elicited from single cones do not begin to emerge until the stimulus duration is increased substantially—on the order of 500 milliseconds (Sabesan et al., unpublished). These times scales are consistent with work showing reduced wavelength discrimination for brief stimuli (Regan and Tyler, 1971).

Taken together, these findings and observations seem to support a magnocellular substrate for our task. Nevertheless, it is worth noting that recent *in vitro* multi-electrode recordings of retinal ganglion cells found similar contrast sensitivity profiles in parasol and midget cells when driven with cone-sized stimuli, albeit for 250 millisecond stimuli presented at mid-peripheral (15-40º) eccentricities (Li et al., 2014). This work, as well as that being emerging from other novel electrophysiological techniques (Sincich et al., 2009), underscores the fact that conventional wisdom founded on standard experimental approaches may break down when visual performance is probed at the elementary scale of individual receptors.

3.6   Summary and Future Directions

In this chapter, we began with a simple goal: to link single-cone psychophysical performance with the spectral type of individual photoreceptors. Measuring increment thresholds cone-by-cone under L-cone isolating conditions produced reasonable agreement with an objective classification method employing adaptive optics densitometry. When examined in more detail, our data suggested that the performance of relatively un-adapted cones (i.e. L-cones) may be inhibited by elevated activity in their immediate neighbors. The physical limits of our stimulation resolution were modeled based on previous work and found to account for some, but not all, of the sensitivity-reducing effects of adjacent M-cones. Potential neural avenues for lateral interaction of cone signals—including inter-cone coupling, horizontal cell feedback, and post-receptoral adaptation—that may contribute to this effect were discussed.

While the data in this chapter are not sufficient to delineate between the potential sites of neural interaction among individual cones signals, future work can be designed to parse them more effectively. A carefully calibrated adapting field—one which leaves L- and M-cones in an equally adapted state—could be used to eliminate the effects of electrical coupling and allow the impact of stimulus blur to be modeled without confounding factors. Once accomplished, it

would be of interest to investigate how interactions among cone signals may influence performance on a single-cone-driven psychophysical task. To do so requires inducing activity in one cone class while stimulating receptors of another. In our task, we adopted a traditional approach to cone isolation by using steady adapting fields (Stiles, 1949, 1959). Other investigators have found isolation of a given cone class to be improved substantially when the test stimulus is accompanied by a background exchange that induces an abrupt spike in the adaptation state of the other two cone types while remaining unseen by the target class (Stockman et al., 1993a; Stockman et al., 1993b). To distinguish between the effects of cone coupling and post-receptoral processes, the silent substitution method might prove useful, as adjusting the relative timing and/or duration of the exchanged background with respect to onset of a brief stimulus may be used to distinguish between the fast signal spread propagating through gap junctions (Hornstein et al., 2004) and the relatively sluggish reductions of sensitivity associated with horizontal cell feedback (Smith et al., 2001; Lee et al., 2003) and pooled adaptation signals in the post-receptoral circuitry (see, for example, Fig. 6 in (Westheimer, 1967)).

3.7 Acknowledgements

CHAPTER 4 – Adaptive Optics Microperimetry: Methods and Validation in Normal Eyes and Patients with Retinal Disease

4.1   Abstract

The methods and results presented in the previous sections demonstrate how photopic vision can be studied one cell at a time. In a clinical setting, however, cone-by-cone assessment of outer retinal disease may prove impractical, owing to a number of complicating factors that emerge when patients become involved: reduced image quality, increased eye movements, and limited chair time. Nevertheless, functional testing with AOSLO is a potentially powerful tool, as it is capable of establishing structure-function correlations with unmatched precision. This chapter describes methodologies developed and adopted to allow this technology to be translated to the clinic. Early efforts to validate the system on normal subjects are presented, as well as two case reports from patients with outer retinal disease that demonstrate agreement between multimodal structural assessment and high-resolution visual function testing.

4.2   Introduction

The introduction of adaptive optics (AO) into ophthalmic imaging systems by Liang et al. in 1997 ushered in a new frontier in retinal imaging (Liang et al., 1997). By measuring and compensating for the high-order monochromatic aberrations of the eye, it became possible to collect images of the living retina in which individual photoreceptor cells could be resolved reliably. While the earliest forays into AO-based imaging dealt primarily with describing the normal cone photoreceptor mosaic (Liang et al., 1997; Roorda and Williams, 1999; Brainard et al., 2000), one immediately obvious application of high resolution retinal imaging is in its potential to observe and characterize the structural changes associated with retinal disease on the cellular scale.

The adaptive optics scanning laser ophthalmoscope (AOSLO) is one such AO-based imaging modality (Roorda et al., 2002), and it has been used extensively to evaluate the cone photoreceptor mosaic in both normal subjects and patients with retinal disease (Wolfing et al., 2006; Duncan et al., 2007; Yoon et al., 2009; McAllister et al., 2010; Duncan et al., 2011b; Talcott et al., 2011). Over the past 10 years, AOSLO imaging systems have continued to evolve. Increasingly finer structures, including rod photoreceptors and foveal cones, are now resolvable (Dubra and Sulai, 2011; Dubra et al., 2011; Merino et al., 2011). A recent investigation in a group of patients with retinitis pigmentosa demonstrated that cone mosaic structure can be followed longitudinally in a patient population, suggesting that AOSLO imaging may be an especially sensitive outcome measure for clinical trials evaluating treatments aimed to slow down the progression of inherited retinal diseases (Talcott et al., 2011).

While AOSLO can be used to track high-resolution structure in the retina over time, the functional consequences of subtle changes in the photoreceptor mosaic are often difficult to elucidate. In patients with retinal disease, AOSLO images often contain patches where photoreceptor structure is ambiguous, owing to an increased presence of factors that

compromise imaging, such as media opacities, retinal edema, and weakly reflecting cones. To ensure that high fidelity metrics of photoreceptor distribution (i.e., cone spacing and cone density) can be acquired in this population, it becomes necessary to select regions of interest (ROIs) within AOSLO images where unambiguous arrays of cones can be identified and tracked longitudinally. Often, these ROIs span relatively small patches of retina; for example, ROI width ranged between 0.2° and 0.6° in the work of Talcott and colleagues. If AOSLO imaging is to emerge as an objective marker of disease progression, the notion that a visible cone is a functional cone must be tested. To best accomplish this, the functional status of the cones located within the small ROIs selected for analysis must be established with confidence. In addition to describing the function of cones that can be resolved with ease, tools capable of high-precision visual function testing would also deepen our understanding of the regions in AOSLO images where photoreceptor mosaic structure is ambiguous or compromised.

It has been suggested recently that the reflectance properties of cones may serve as a proxy for their functional viability (Dubis et al., 2014), but definitive functional evidence supporting these claims has yet to arrive. One reason for this is that correlating structural findings from AOSLO imaging with results from conventional perimetric devices is prone to imprecision. Traditional perimetry instruments (e.g. Humphrey Visual Field Analyzer) are unable to monitor and correct for small fixational eye movements and offer a limited array of test patterns, leaving the examiner to infer which regions of the retina were stimulated during a given visual field test and unable to target specific ROIs for functional assessment. Fundus-related perimetry, often referred to as microperimetry, obviates the need for inference by conducting simultaneous retinal imaging and visual function testing, allowing more precise structure-function correlations to be established in patients with retinal disease (Sjaarda et al., 1993; Takamine et al., 1998; Schmitz-Valckenberg et al., 2004; Okada et al., 2006). While custom-built and commercially-available microperimeters typically feature some form of eye tracking, thereby permitting the delivery of stimuli to targeted locations (Sunness et al., 1995; Midena et al., 2010), their ability to target and test visual function in regions as small as the ROIs defined in the typical AOSLO imaging study remains lacking. For instance, in a commercially-available microperimeter (MP1, Nidek Technologies, Padua, Italy), a mean eye tracking accuracy of 4.9 arcmin has been reported (Midena, 2007), and the image registration between the IR tracking image and color fundus photograph on which results are plotted is subject to errors as large as 2 degrees (Enoch and Le, 2004; Woods et al., 2007). Given that the smallest stimulus presented by the MP1 is Goldmann I-sized (6.5 arcmin diameter), this system may lack the precision to probe visual function over time within ROIs as small as 12 x 12 arcmin.

A second limitation associated with most microperimeters is their inability to detect subtle changes in visual dysfunction. In the MP1, this is apparent when one examines its normative sensitivity values: despite enormous changes in the packing density of cones (Curcio et al., 1990) and the convergence of their signals onto downstream neurons across the parafovea (Curcio and Allen, 1990), the MP1 measures a completely flat sensitivity profile over the central 20 degrees (Midena et al., 2010). This is likely due to its limited dynamic range (20 dB) which may lead to "floor effects", although stimulus size may also play a role (Bowl et al., 2013). In any event, a perimetric approach that cannot reveal the expected change in sensitivity across

the parafovea associated with normal anatomy is unlikely to be sensitive to subtle changes induced by retinal disease.

To put the high resolution structural data yielded by AOSLO imaging into a more meaningful context, tools capable of testing visual function on a commensurate scale are needed. In this chapter, we build upon the work described in the preceding sections of this document and describe a series of methodological adjustments that enable the quick and efficient measures of visual sensitivity at targeted retinal loci. Although many of the features that distinguish AOSLO microperimetry from other perimetric devices have already been applied to the study of primate electrophysiology (Sincich et al., 2009), here we present a more efficient and robust system that can be used in humans—in both normal subjects and patients with retinal disease—to image and test a region of cones simultaneously, with the capacity to follow these measures longitudinally. This chapter will demonstrate how this method has been translated to the clinical realm, while highlighting its potential to define structure-function relationships in patients with retinal disease. Ultimately, AOSLO microperimetry may prove a valuable tool for use in clinical trials designed to evaluate new treatments for retinal degeneration.

4.3 Methods

4.3.1 Participants

For our normal subjects, seven individuals were recruited from the student and faculty population of the University of California, Berkeley and the University of California, San Francisco. The participants belonging to this group were 5 males and 2 females, with an average age of 32.5 years (SD = 7.3; range = 25 to 44). In addition, two patients with outer retinal disease were recruited for AOSLO imaging and psychophysical testing in the Department of Ophthalmology at the University of California, San Francisco: a 39 year-old female with simplex retinitis pigmentosa and a 53 year-old male with dry age-related macular degeneration. Prior to enrollment, informed consent was obtained after the study protocol and its potential risks and complications were presented to the subject in verbal and written form. The study design and informed consent documents were approved by the University of California Institutional Review Board and the research was conducted in accordance with the tenets of the Declaration of Helsinki.

4.3.2 Measuring Visual Sensitivity Across Eccentricity in Normal Subjects

Simultaneous high resolution retinal imaging and visual function testing were conducted using an AOSLO. The specifics of imaging and conducting psychophysical experiments with AOSLO have been described elsewhere in this document. For the purposes of this chapter, only the general nature of the psychophysical tasks and the data analysis associated with using AOSLO to measure visual sensitivity in normal subjects and patients will be described here; for details of AOSLO imaging, stimulus generation and delivery, test location selection, and light source calibration, refer to the preceding chapters.

In the first experiment, an increment threshold approach was used to measure visual sensitivity at various retinal eccentricities between 0 and 5 degrees along the temporal horizontal meridian of one eye. For each eccentricity, thresholds were measured a total of eight times over the course of two testing sessions. The retinal loci targeted for sensitivity testing were either chosen manually by the observer (Subjects 1-5) or using software designed to automatically recover previously-tested locations (Subject 6; Section 4.3.4). The background for testing was produced by a 2.1° x 2.1° raster scan of the 840 nm imaging superluminescent diode (SLD; Superlum, Carrigtwohill, Ireland; power = 200 μW = 1.47 log Trolands) and the test stimulus was generated by a 680 nm SLD (Superlum, Carrigtwohill, Ireland) controlled by an acousto-optic modulator (AOM; Brimrose Corp, Baltimore, MD, USA) operating at up to 50 MHz (Poonja et al., 2005). When the stimulus light source was set to a maximum power of 26 nW, the AOM leak was on the order 0.2 nW (= -0.13 log Trolands calculated for a field size of 4.41 deg^2). Thus, for the data presented in this study, the total retinal illuminance produced by the raster scan was 1.47 log Trolands; however, as the power incident on the AOM is increased, the amount of light leaking through the AOM also increases, resulting in different background intensities at different power settings. The power of the stimulus light source is adjustable, and for the data presented in this study its maximum power was set to 26 nW, corresponding to a maximum retinal illuminance of 1.98 log Trolands for the Goldmann I-sized stimulus (diameter = 6.5 arcmin; ~32 μm on the retina) used in this study. The AOSLO-based microperimetry protocol was implemented via a custom software interface used for programming psychophysical experiments in our laboratory (Matlab, Mathworks Inc., Natick, MA, USA). All data for this experiment were collected using a self-paced 40-trial QUEST staircase with a yes-no response paradigm (Watson and Pelli, 1983).

To measure sensitivity, dynamic AO imaging was initiated (for details, see previous chapters), allowing retinal videos to be stabilized in real-time and the region targeted for stimulus delivery to be selected. Twenty minutes before AOSLO imaging, one drop of 1% tropicamide and one drop of 2.5% phenylephrine were instilled to achieve mydriasis and cycloplegia. Once the pupil was sufficiently dilated, the subject was situated in a chin rest mounted on an X-Y-Z stage and the pupil was aligned with the imaging beam. Head stabilization was aided using padded temple mounts and subject fixation was guided using a laser-illuminated spot on a screen external to the system. All wavefront sensing and correction were done over a 6 mm pupil.

A high-speed image-based eye tracking algorithm was used to track the retinal locus targeted for testing and generate a prediction on when to deliver the perimetric stimulus (Arathorn et al., 2007; Yang et al., 2010). Each individual trial of the psychophysical staircase was initiated by the subject with a button push, triggering the recording of a one second imaging video during which the perimetric stimulus was delivered to the targeted retinal location non-continuously over a period of 200 msec. Poor image quality and fixational eye movements greater than ~50% of the raster size can both cause the image-based eye tracking algorithm to fail. When this was the case, stimulus delivery would not be initiated. To help differentiate between true negatives and trials during which stimulus delivery was not

triggered, an auditory cue was provided for the subject whenever the voltage signal was sent to the AOM to deliver the stimulus. Individual trials during which stimulus delivery failed were immediately repeated. After stimulus presentation, the subject indicated their response via keyboard press and then initiated the next trial. Each response and its associated experimental parameters were saved to a data file for subsequent analysis.

Once all measures of visual sensitivity were collected, experiment videos were processed offline to generate retinal images with high signal-to-noise ratios. Stimulus delivery location was determined for each trial, allowing the removal of trials where delivery was spatially errant or failed entirely. Individual trials with a delivery error greater than 4 pixels (~1.0 arcmin) were excluded from analyses; when necessary, thresholds were recomputed using only trials where the stimulus fell within the inclusion window.

Next, the test location for each sensitivity measure was plotted onto an AOSLO image montage, and the distance to the subject's preferred retinal locus of fixation was calculated. Measured visual thresholds ($T_{measured}$) were converted to sensitivities in decibels (S_{dB}) using Equation 1, where T_{max} is the maximum retinal illuminance produced by the stimulus light source and $T_{measured}$ is the retinal illuminance at threshold, both in Trolands:

$$S_{dB} = 10 \times \log_{10}(T_{max}/T_{measured}) \tag{1}$$

Expressing sensitivity in decibels is common in the perimetric literature, but the reader should be cautioned that this scale simply reflects the ratio of the threshold retinal illuminance to the maximum retinal illuminance the perimeter is capable of displaying. Since these basic parameters differ from device to device, sensitivities in decibel values are not directly comparable across instruments. For these reasons, a conversion table between decibels and AOM arbitrary units is provided in Appendix 1.

Visual sensitivities were plotted as a function of retinal eccentricity, and a linear regression was fit to the data using curve fitting software (Matlab, Mathworks Inc., Natick, MA, USA). Cone photoreceptors were identified in the AOSLO images using a combination of manual and automated cone counting software, allowing metrics of photoreceptor distribution to be calculated (Li and Roorda, 2007). Cone spacing data were used to estimate the number of cones sampling the perimetric stimulus. To ensure high fidelity cone spacing data, only test locations beyond 2 degrees retinal eccentricity were included in this analysis. Visual sensitivity was plotted as a function of the number of cones sampling the stimulus and a linear regression was fit to the data.

4.3.3   Choosing a Threshold Algorithm: Bland-Altman Analysis of QUEST vs 4-2 dB

When selecting a psychophysical test strategy to measure visual thresholds in a patient population, a number of factors must be taken into consideration: accuracy, repeatability, and test duration. The Bayesian adaptive staircase approach described in the previous section is commonly used to obtain fast and reliable estimates of threshold in practiced observers, but it

can be especially susceptible to subject errors that occur during the first few trials (Vingrys and Pianta, 1999), and may be less repeatable at test sites with reduced sensitivity (Artes et al., 2002). The shortcomings of the Bayesian approach are a particular concern when the goal is to measure thresholds in patients who may have reduced function and are often naïve to the task.

With this in mind, we investigated the agreement in thresholds yielded by two staircase approaches: the Bayesian method described above and a modified 4-2 dB staircase similar to the "full threshold" strategy employed by conventional perimetry. In four of our normal subjects, measures of visual sensitivity were collected at the fovea and 2.25° eccentricity over two measurement sessions separated by two days. The stimulus was an aberration-corrected Goldmann I-sized spot ($\lambda = 680$nm) delivered to targeted retinal loci. Initial test locations for each retinal eccentricity were saved to reference frames, and subsequent locations were selected automatically using Fourier-based image registration (for details, see next section). Increment thresholds were obtained using two different strategies: (1) a 40-trial adaptive Bayesian staircase procedure (QUEST); and (2) an average of three consecutive 4-2 dB staircases. The latter operates by adjusting stimulus intensity in 4 dB steps until the first reversal (e.g., "yes" followed by "no", or vice versa) is reached, after which step size is reduced to 2 dB. The second response reversal terminates the staircase, and threshold is taken as the midpoint between the last two trial intensities. Bland-Altman analyses were used to assess limits of agreement (LOA) between threshold strategies (Bland and Altman, 1986).

4.3.4   Automated Retrieval of Previously-Tested Locations

In many cases, it is desirable to return to previously-tested retinal locations at subsequent AOSLO imaging sessions. This is particularly true for clinically-motivated investigations, where the ability to track photoreceptor structure and function longitudinally could enable a better understanding of the natural course of retinal disease progression, as well as providing an avenue for establishing the efficacy of therapeutic intervention. In the software interface described in the first chapter, retinal targets are selected for testing manually via mouse click. Repeated selection of the same retinal locus under these conditions is difficult because the reflectance of the mosaic can vary considerably over the course of just a few hours (Pallikaris et al., 2003). Further, day-to-day fluctuations in image quality and vascular appearance can make it difficult to select locations targeted in previous sessions for retesting.

Due to normal fixational drift, cyclotorsional eye movements, and the subtle intersession variations in raster scanning geometry that result from calibrating the field size each day, optimal real-time image stabilization is best achieved using a reference frame selected immediately before capturing a video. As a result, each psychophysical procedure (i.e. a 40-trial staircase) is typically associated with a unique reference frame, and the x- and y-coordinates marking the retinal target in one reference frame will not necessarily correspond to the same retinal location in a reference frame acquired at a later session. Thus, while stimulus delivery to a targeted retinal location during a given set of trials can achieve single cone precision, it is difficult when selecting test locations manually to target the same patch of cones for repeat

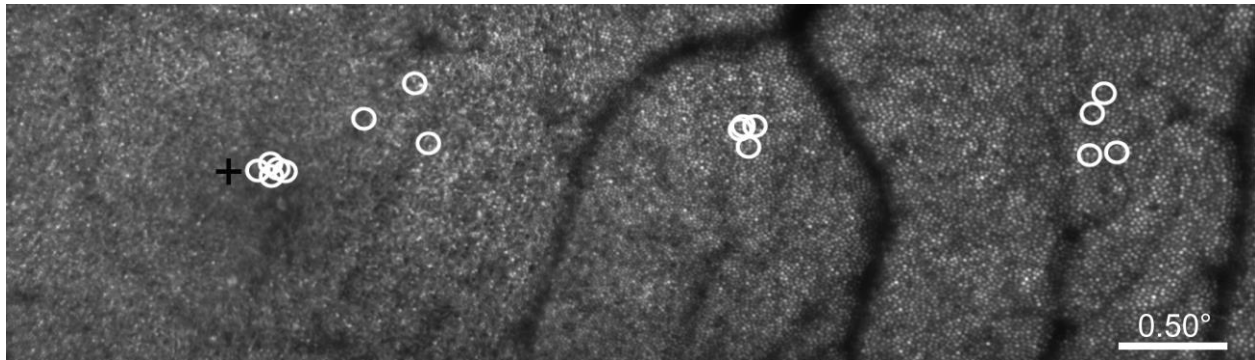testing with consistency, especially near the fovea where there are fewer retinal landmarks (Figure 4.1).

Figure 4.1| Adaptive optics microperimetry test locations for Subject 3. Manually-selected test locations for AOSLO-based microperimetry are denoted by the white circles, the size of which represents the size of the perimetric stimulus on the retina (Goldmann I = 6.5 arcmin = ~32 μm on the retina). The subject's preferred retinal locus of fixation is marked by the black cross.

To mitigate this problem, custom software was incorporated into the current imaging interface (Yang et al., 2010) to enable the automated retrieval of previously-tested locations. When a given region of interest is tested for the first time, the x- and y-coordinates of the location selected for targeted delivery are saved. At subsequent sessions, the original test location can be recalled by using a fast image registration algorithm (Guizar-Sicairos et al., 2008) to calculate the shift between the original reference frame and the current reference frame. Applying this shift to the saved x- and y-coordinates of the original reference frame allows the original retinal test location to be identified and targeted in the x- and y-coordinates of the current reference frame. A schematic of this registration process is shown in Figure 4.2.
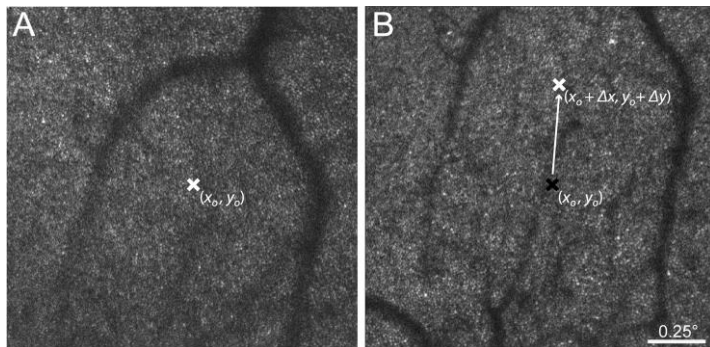
Figure 4.2| Method for retrieving previously-tested retinal locations. **A)** The reference frame for real-time video stabilization from a previous AOSLO microperimetry testing session with the retinal location (x_o, y_o) targeted for sensitivity testing indicated by the white "x". **B)** The reference frame from a subsequent testing session, in which the retinal position has changed. The reference frame in **B** is registered to the frame in **A**, and the shift $(\Delta x, \Delta y)$ between the two images is applied to the target x- and y-coordinates of the original frame (black "x") to retrieve the previously tested retinal location (white "x") automatically.

4.3.5   Structure-Function Relationships in Normal Subjects: Probing Angioscotomas

To further test the level of stimulus control offered by AOSLO-based microperimetry, the methods described in the preceding sections were used to measure visual thresholds in one subject on and around a parafoveal blood vessel (eccentricity = 2.5°) using a 4.2 arcmin stimulus. Because the retinal vasculature is located anterior to the photoreceptor layer, the blood vessels cast a shadow on the underlying retina, resulting in a corresponding decrease in visual sensitivity known as angioscotoma (Evans, 1927). Three measures of visual threshold were collected at each of three locations, including one directly over a blood vessel whose luminal diameter was roughly equal to the stimulus size (~21 μm). Measured sensitivities were averaged based on location and compared statistically using a two-tailed t test. To test visual sensitivity over the blood vessel, it was necessary to increase the maximum power of the stimulus light source to 0.68 μW, which produced a maximum retinal illuminance of 3.40 log Trolands for a stimulus of this size. Because increasing the stimulus light source intensity results in an increased amount of light leaking through the AOM when it is switched off, the background retinal illuminance increased by roughly 50% for this power setting. Thus, the threshold values plotted in Figures 4.4A and 4.7C should not be compared directly.

4.3.6   Structure-Function Relationships in Outer Retinal Disease: Two Case Reports

We examined the relationship between the structure observed with AOSLO and optical coherence tomography (OCT) and function measured with adaptive optics microperimetry. Two cases are presented: in the first, structure and function in the cone mosaic was assessed in a patient with early-stage simplex retinitis pigmentosa; in the second, visual sensitivity was measured on and around parafoveal subretinal drusen in a patient with dry age-related macular degeneration. All thresholds were measured using the 4-2 dB staircase described in Section 4.3.3; however, a 543 nm spot (diameter = 3 arcmin) was used in place of the original long-wavelength stimulus. The background luminance was set to 100 Trolands to ensure testing in the photopic range (Aguilar and Stiles, 1954). Transverse chromatic aberration was minimized by adjusting the patient such that the imaging raster and stimulus raster (resulting from AOM leak) were in subjective alignment. Cone spacing was assessed from the AOSLO images using methods described previously (Li and Roorda, 2007; Talcott et al., 2011).

4.4   Results

4.4.1   Measuring Visual Sensitivity Across Eccentricity in Normal Subjects

The performance of real-time eye tracking, which allows for targeted stimulus delivery to selected retinal locations, is demonstrated in Figure 4.3. When fixation was stable and photoreceptor mosaic structure was well-resolved, high-speed eye tracking and targeted stimulus delivery enabled the same patch of cones to be stimulated on 100% of trials; by contrast, without high-speed eye tracking, any given cone will be stimulated only on a fraction

of trials, even with good fixation. Across all test locations and normal subjects, the vertical and horizontal stimulus delivery errors averaged 0.81 and 0.89 arcmin (~4 microns), respectively. On average, delivery errors were isotropic (p = 0.14, two-tailed t-test). In general, tracking performed best at locations beyond 1 degree eccentricity, owing to retinal features becoming more easily resolved with increasing distance from the fovea. Based on our predetermined exclusion criterion, the stimulus was delivered to its targeted location on 90.1% of all trials.
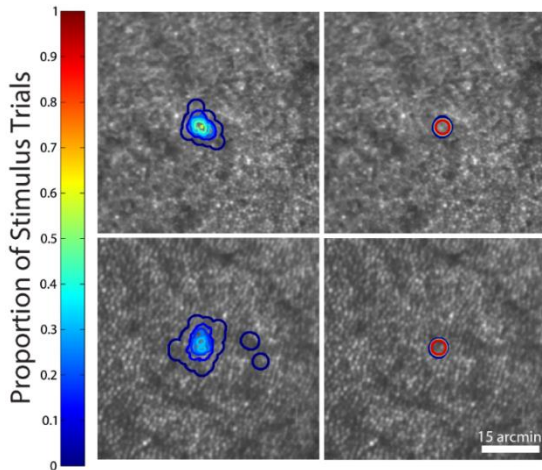
Figure 4.3| Stimulus delivery plots for adaptive optics microperimetry stimulus delivery. Contour lines delineate the proportion of trials that a given pixel was stimulated during a psychophysical task (n = 60 trials). Stimulus delivery plots are shown for conditions without (left) and with (right) retinal tracking at two eccentricities (top: 0.5°; bottom: 1.5°).

Visual sensitivity to the Goldmann I-sized stimulus decreases as a function of increasing eccentricity (Figure 4.4A; slope = -1.32dB/degree; R^2 = 0.60; P < 0.001). Beyond 2 degrees, there is a significant correlation between visual sensitivity and the number of cones sampling the perimetric stimulus, as estimated from cone spacing measures (Figure 4.4B; slope = 0.19; R^2 = 0.41, P < 0.001).
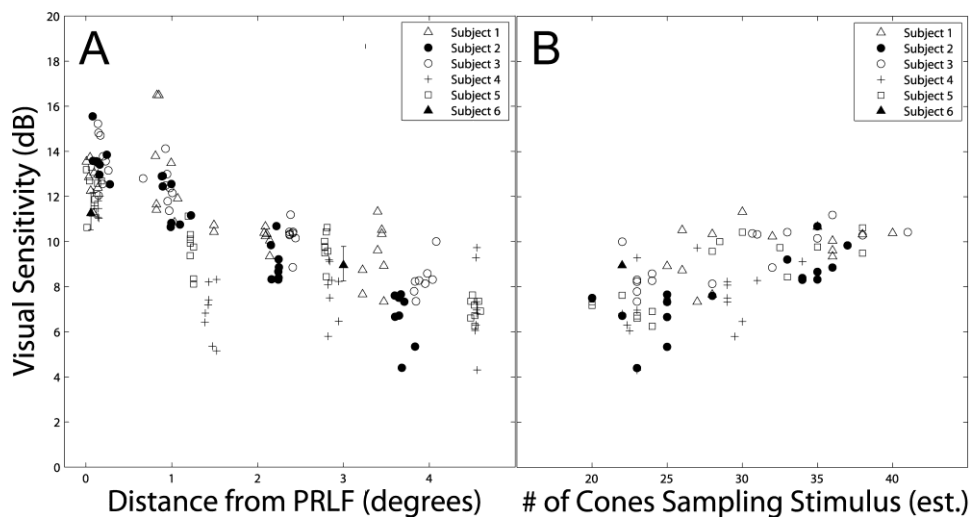
Figure 4.4| Visual sensitivity versus retinal eccentricity and number of cones stimulated. **A)** Sensitivity values are plotted in dB as a function of retinal eccentricity. **B)** Sensitivity is plotted as a function of the number of cones sampling the stimulus, which is estimated from measures of cone spacing.

4.4.2 Choosing a Threshold Algorithm: Bland-Altman Analysis of QUEST vs 4-2 dB

The agreement between the two threshold strategies is shown in Figure 4.5. Thresholds measured with QUEST were not significantly different from those measured using the 4-2 dB staircase (mean difference: 0.067 dB; p = 0.99, paired t-test; 95% LOA: -2.68 dB to +2.82 dB). Linear regression of the data produced a slope of 0.04, which was not significantly different from zero (p = 0.59), suggesting the agreement between the two methods was independent of the underlying sensitivity. The average number of trials per 4-2 dB staircase was 14.0 ± 2.8, corresponding to roughly 60 seconds per threshold measurement.
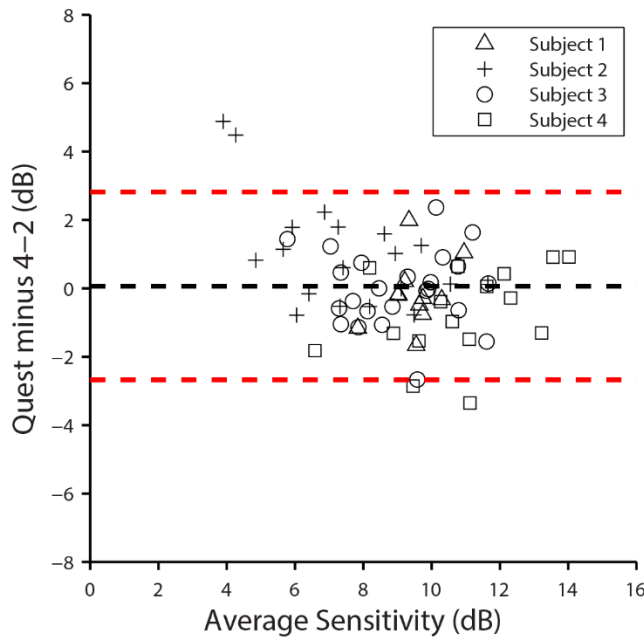
Figure 4.5| Bland-Altman analysis of two threshold staircase algorithms. Pairwise differences between sensitivities yielded by a 40-trial Bayesian adaptive staircase (QUEST) and a modified 4-2 dB staircase strategy are plotted against their average. Sensitivity values are expressed in decibels (dB), and were collected at locations along the temporal horizontal meridian between 0 and 4 degrees. At each test site, measures were repeated four times for each algorithm. The mean difference between the two approaches is plotted as the black dotted line; the red dotted lines represent the upper and lower limits of agreement, respectively (i.e. the 95% confidence interval).

4.4.3 Automated Retrieval of Previously-Tested Locations

Figure 4.6 demonstrates the automated recovery of previously tested locations. Although the majority of the data presented in this study were collected at retinal loci manually selected by the examiner, the automated recovery allows AOSLO-based microperimetry testing to be repeated at the same retinal location with good precision. Stimulus location recovery appears robust to reference frame misalignments, and can retrieve previously-tested locations over a period of several months.

4.4.4 Structure-Function Relationships in Normal Subjects: Probing Angioscotomas

Results from angioscotoma testing in Subject 3 are shown in Figure 4.7. Visual sensitivity for stimuli targeted at the retinal blood vessel is significantly lower than when measured in directly adjacent retina (Figure 4.7C; p<0.05, two-tailed t-test), revealing a relative angioscotoma.
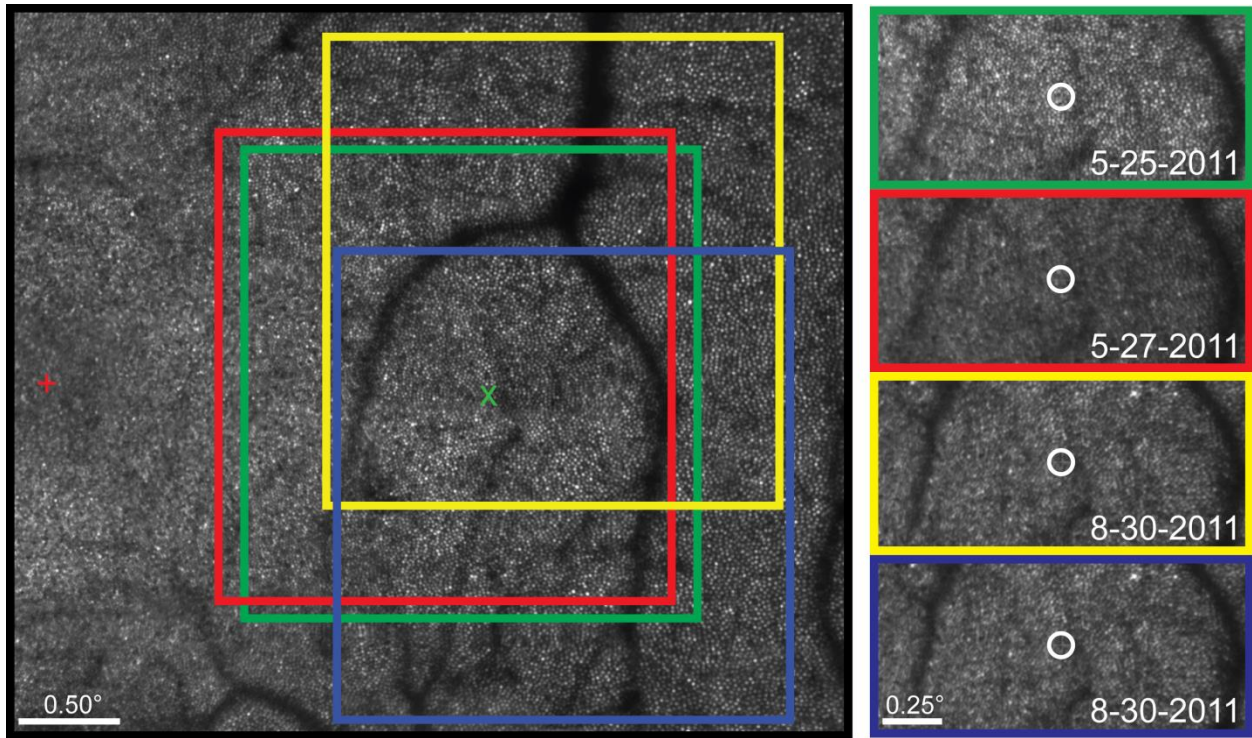
Figure 4.6| Automated stimulus location recovery in Subject 3. (Left) Highlighted regions corresponding to individual reference frames used to collect stabilized retinal videos at ~2.5° retinal eccentricity. The original reference frame is outlined in green and the targeted retinal location for stimulus delivery is marked by the green "x". To retrieve the original test location, subsequent reference frames (red, yellow, blue) are registered against the original, and the shift is used to define the targeted retinal locus in the x-y coordinates of the new reference frame. The subject's preferred retinal locus of fixation is represented by the red cross. (Right) The Goldmann I-sized white circles are plotted at the average stimulus delivery location for a 40-trial psychophysical task performed at baseline, baseline + 2 days, and baseline + 3 months.
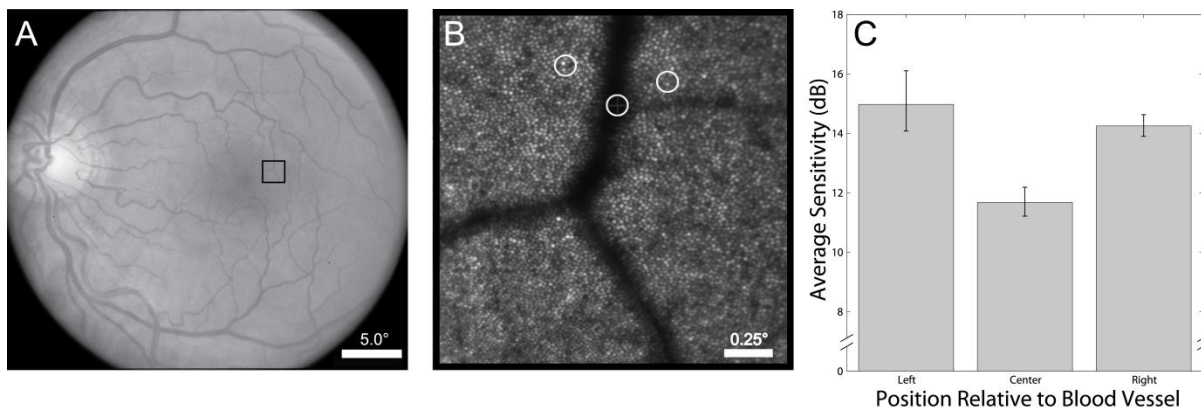
Figure 4.7| Results from sensitivity testing on and around a parafoveal blood vessel. **A)** Fundus photograph with box indicating the blood vessel targeted for AOSLO-based microperimetry (eccentricity ~2.5°); **B)** AOSLO image with perimetry test locations indicated; **C)** Average sensitivity plotted as a function of stimulus location (error bars = ± 1 SEM). (Note: The size of the white circles marking test location represent the size of the stimulus on the retina.)
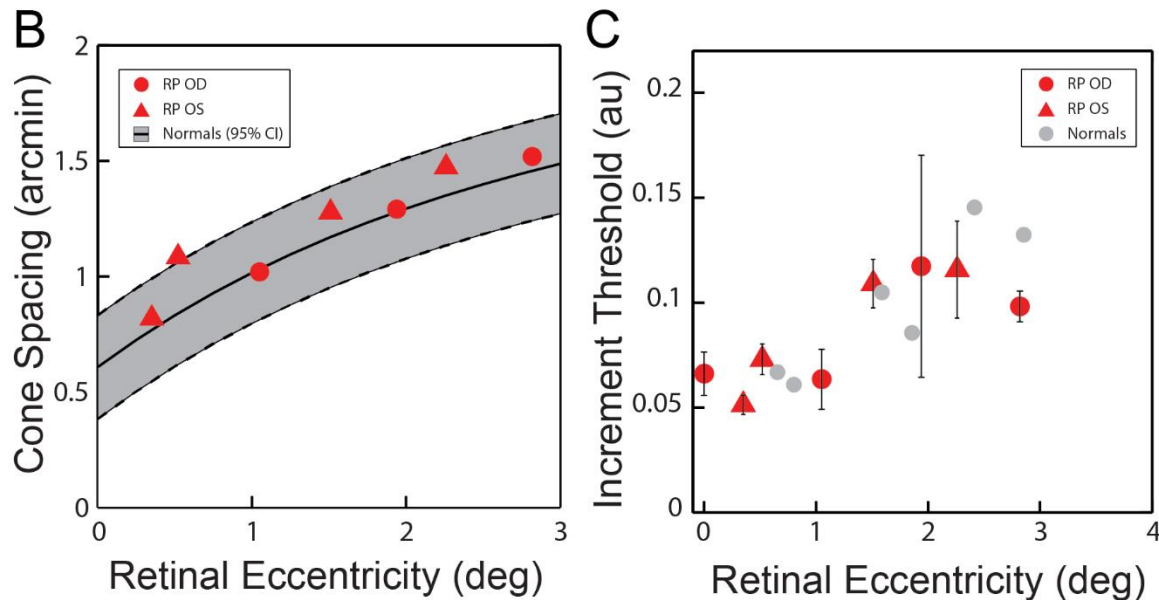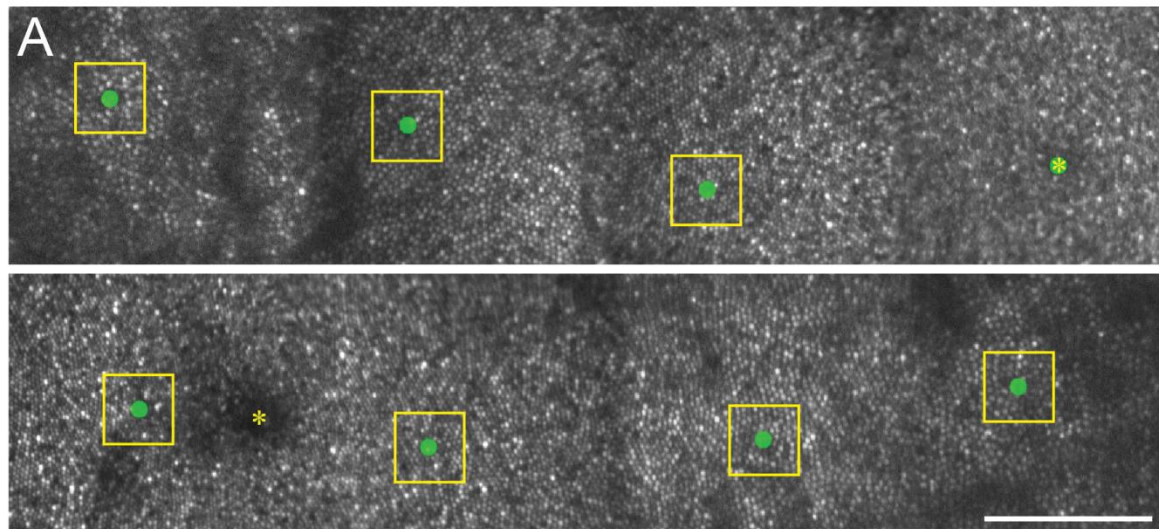
Figure 4.8| Adaptive optics microperimetry in simplex retinitis pigmentosa. **A**) AO images from the right (upper) and left (lower) eyes of a 39 year-old female patient with simplex RP (scale bar = 0.5 degrees). Green markers denote AOSLO microperimetry test sites; asterisks indicate foveal location. Yellow boxes outline regions selected for cone spacing analysis. **B**) Cone spacing analysis for reveals normal cone spacing values across the parafovea (black center line: normal mean cone spacing; gray shaded area and black boundary lines = 95% confidence interval). **C**) AOSLO increment thresholds plotted as a function of retinal eccentricity, demonstrating similar thresholds relative to normal data collected near the same time (error bars = ± 1 SD; gray spots = normal threshold data).

4.4.5   Structure-Function Relationship in Outer Retinal Disease: Two Case Reports

Parafoveal AOSLO images for the right and left eyes of a 39 year-old patient with simplex retinitis pigmentosa are shown in Figure 4.8A (upper and lower panels, respectively). At all test sites, cone spacing was within normal limits (Figure 4.8B). Thresholds measured in this patient increased with eccentricity in a similar fashion to data taken on the same system from a group of age-similar normals (Figure 4.8C). OCT scans through the test regions showed normal appearance, including an intact inner-segment/outer-segment band (data not shown).

Figure 4.9 shows adaptive optics imaging and microperimetry results from 53 year-old male patient with early-stage dry age-related macular degeneration. The AOSLO image montage is aligned to the underlying color fundus photograph, with individual test sites indicated (Figure 4.9A). Image quality was variable across the montage, with several sites of clearly-resolved cones interspersed with regions containing ambiguous structure. Threshold data were collected on and around apparent subretinal drusen. OCT b-scans aligned to the color fundus photo (gray and blue lines in panel A) demonstrate drusen deposits accompanied by varying amounts of laminar disruption in the inner retina (Figure 4.9B-C). The inner segment-outer segment junction appears continuous in both OCT scans shown here. Approximate test locations are denoted by the yellow arrowheads in the OCT images. Increment thresholds measured with adaptive optics at Sites 3 and 4 (see Panel C) were elevated relative to those collected at eccentricity-matched sites featuring less laminar disruption on the OCT image (Sites 5 through 7; see Panel B), despite the qualitatively similar appearance of both test sites on the *en face* AOSLO image.

4.5   Discussion

4.5.1   Controlling the Perimetric Stimulus

The results of this study demonstrate that high precision visual function testing can be achieved with AOSLO-based microperimetry, both in normal subjects and in patients with outer retinal disease. With dynamic AO correction in place, stimuli that are at or near the diffraction limit can be presented to the subject's retina, leaving the examiner more confident about the pattern of light that is being sampled by the photoreceptors. While monitoring and correcting high-order aberrations is not an infallible process, an advantage of conducting simultaneous retinal imaging and visual function testing—compared to a non-imaging AO psychophysics system—is that the sharpness of the perimetric stimulus in the imaging plane is directly tied to image quality, minimizing the need to rely on other metrics, such as root-mean-square deviation or Strehl ratio, as an indicator of stimulus fidelity. However, it bears mentioning that any stimulus—AO-corrected or not—is subject to scatter as it travels through the retina, and the degree of scatter in layers not conjugate with the confocal imaging pinhole is not conveyed in the collected image (for more, see the discussion of Chapter 2).
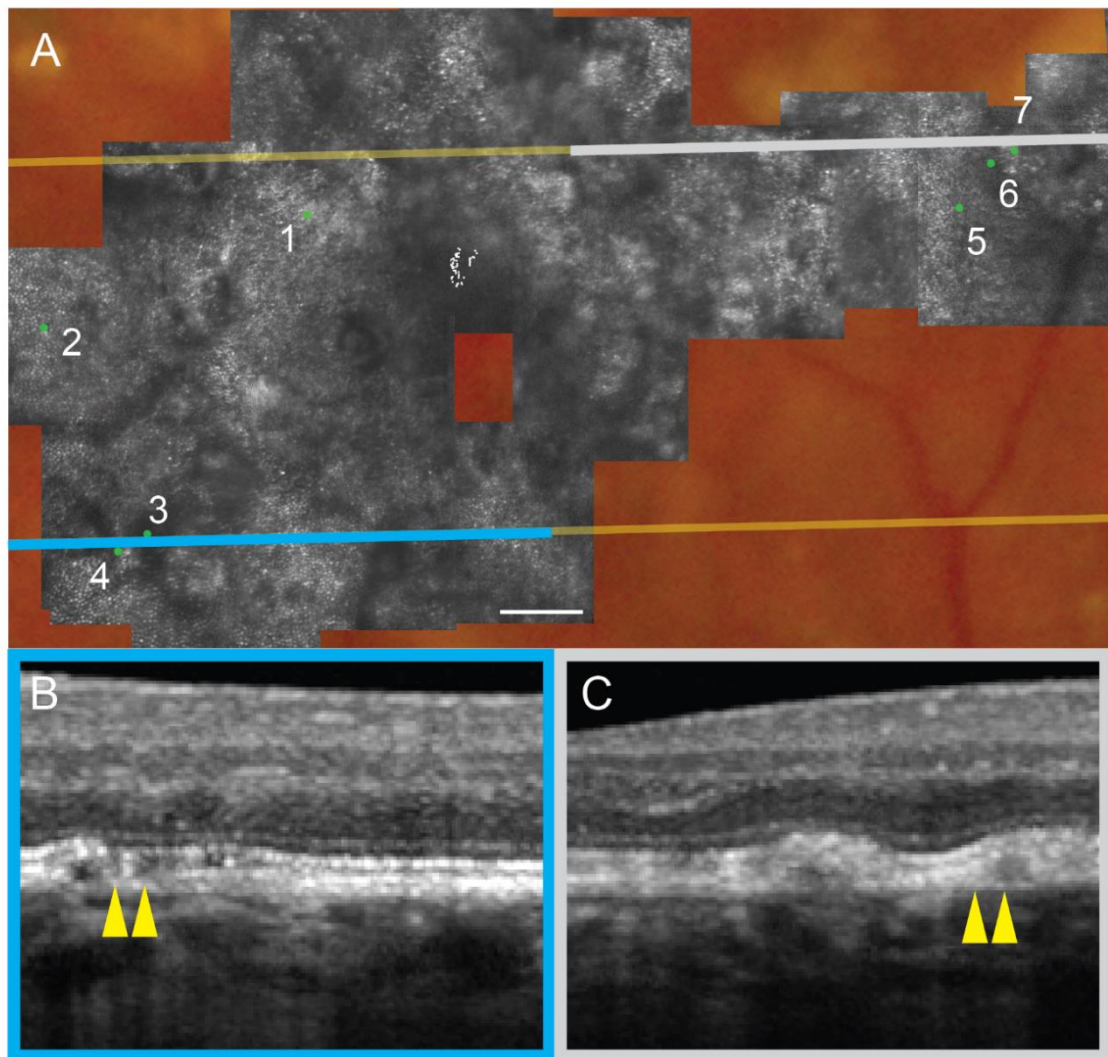
Figure 4.9| Adaptive optics microperimetry in dry age-related macular degeneration. (A) AOSLO image montage from the left eye of a 53 year-old male patient with dry AMD (scale bar = 0.5 degrees). Color fundus photo is shown below. Green spots mark microperimetry test sites and are scaled according to their retinal size; site numbers correspond to indices in Panel D. Scattered white dots indicate preferred retinal locus of fixation (PRLF). Blue and gray lines correspond to OCT B-scan sections shown in B and C. (B, C) OCT b-scans corresponding to blue and gray lines in A, respectively. Yellow markers indicate approximate location of adaptive optics microperimetry test sites. (D) AOSLO microperimetry thresholds (error bars = ± 1 SD; gray spots = normal data from n = 4 subjects).
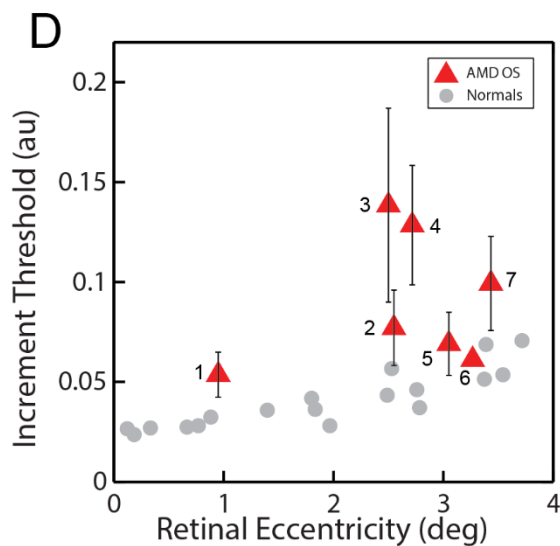
Here we report values for cone-targeted stimulus delivery errors that are roughly 3 times higher than those previously reported using the same high-speed eye-tracking algorithm (Arathorn et al., 2007). The precision of image-based eye tracking and targeted stimulus delivery is primarily contingent on image quality and fixation stability. In both cases, the imaging field size plays a critical role. With regard to image quality, the use of an imaging field larger than the isoplanatic patch of the human eye—about 1 degree (Bedggood et al., 2008)—may result in images of suboptimal quality secondary to variations in the monochromatic aberrations as the wavefront sensor beacon is scanned across the retina. In addition, decreased spatial sampling is inherent to larger raster dimensions if the pixel clock remains fixed, further reducing image resolution. On the other hand, a larger imaging window allows more room for fixational instability, as any eye movement larger than ~50% of the imaging field can cause the ROI targeted for testing to move out of the imaging window, rendering the stimulus undeliverable. Thus, in patients with retinal disease whose fixation may be less stable than normal, the desire for obtaining the highest quality images may need to be balanced against the efficiency with which the AOSLO-based microperimetry system can deliver stimuli to targeted locations.

With this in mind, a 2.1° field size was chosen so that these normative results might be compared against future testing in patients with retinal disease. While the test conditions described in this report are not optimal for targeted stimulus delivery, a delivery error of 0.89 arcmin is still less than the cone-to-cone spacing at all eccentricities beyond 1 degree (Curcio et al., 1990), and is ~5.5x better than the tracking errors reported in the MP1 (Midena, 2007). In the end, the exclusion criterion for errant stimulus delivery can be relaxed or tightened during post-processing, depending on the desired spatial resolution of the sensitivity measures.

Although the reflectance of single cones in the photoreceptor mosaic fluctuates over periods of minutes, and these fluctuations are independent between adjacent cones (Pallikaris et al., 2003), the Fourier-based stimulus location recovery software works over a period of at least three months in a normal subject. While the majority of the data presented in this report were collected before it was implemented, this software will enable measures of visual sensitivity at a specific retinal location to be tracked longitudinally. It is likely that this image registration algorithm is driven primarily by alignment of the cone mosaic. If true, this will serve to limit the precision of the registration in cases where there are disease-induced changes to the cone mosaic. Nevertheless, coarser features such as vasculature may continue to drive the registration, albeit with lower accuracy.

4.5.2   Establishing Structure-Function Relationships on the Cellular Scale in Normal Subjects

AOSLO and other AO-based systems have been used to establish structure-function relationships in the normal human retina (Hofer et al., 2005a; Rossi and Roorda, 2010). Of the studies using AO-imaging to obtain structural measures in patients with retinal disorders, only one endeavored to test visual function on a scale commensurate to the imaging (Makous et al., 2006). Using 0.75' AO-corrected stimuli, Makous and colleagues were able to confirm the

presence of microscotomas in the retina of a patient with a disrupted cone mosaic secondary to a middle-wavelength-sensitive cone mutation. Despite an estimated 30% loss of cone photoreceptors, this patient with dichromacy had normal visual acuity and visual field results (Humphrey 10-2; stimulus size: Goldmann III), suggesting small spot perimetry may be necessary to establish the functional implications of subtle changes in the photoreceptor mosaic. Other studies also hint at the benefit of using small, non-redundant stimuli—which AO-based systems are ideally suited to generate—to reveal more fully the functional consequences of degenerate photoreceptor arrays (Geller et al., 1992; Geller and Sieving, 1993).

While the AO microflash method of Makous et al. produced convincing results, it is perhaps too inefficient to be suitable for use in the wider patient population. Using a flood illuminated AO system leaves the examiner unable to target specific regions in the cone mosaic for functional testing. In patients with diffuse photoreceptor loss, this limitation can be overcome by clever experimental design and statistical inference, but measuring visual sensitivity with efficiency and confidence at focal retinal loci—such as a patch of cones at the edge of geographic atrophy in age-related macular degeneration or within a small ROI in a patient with inherited retinal degeneration—would remain a challenge.

The angioscotoma data shown in Figure 4.7C serve as a proof-of-concept for using the methods outlined in this paper to test focal vision loss. That the blood vessels in the retina cast a shadow on the underlying photoreceptors is not surprising: Purkinje first noted the phenomenon nearly 200 years ago (Westheimer, 2003). However, under normal conditions these shadows are not perceived. It has been postulated that the underlying photoreceptors simply increase their gain to compensate for the decrease in light impinging on them (Westheimer, 2003). It is known that the visual system can undergo rapid local adaptation—for instance, entoptic images of the retinal vasculature induced by transcleral illumination can fade in as little as 80 msec (Coppola and Purves, 1996). This fading is considered analogous to that which occurs when images are stabilized on the retina (Ditchburn and Ginsborg, 1952; Riggs et al., 1953). More recently, it has been observed in some primates that these permanent shadows induce a form of "local amblyopia" on the scale of just a few cones, which is manifested in primary visual cortex of enucleated squirrel monkeys (Adams and Horton, 2002). Although the depth of the defect is contingent on pupil diameter, eye length, vessel caliber, and the distance between the vessel and the photoreceptor layer, these results imply that a different, more long-term mechanism may dictate the function of photoreceptors normally falling in the shadow of the blood vessels. Most perimetric studies of angioscotoma are confined to probing function near the large caliber arteries and veins that emerge from the optic disc (Remky et al., 1996; Schiefer et al., 1999). The data shown in Figure 4.7 represent, we believe, the first report of a quantifiable angioscotoma this close to the fovea. While the data in Figure 4.7 are preliminary findings, the methods outlined in this report could enable a deeper investigation into how the visual system responds to focal long-term visual deprivation.

To use AOSLO-based microperimetry to establish structure-function relationships in the cone photoreceptor mosaic, it is important to ensure that our measures of visual sensitivity primarily reflect cone function. Rod photoreceptors are effectively blind to the 840 nm

background, and they will not be bleached as a result of exposure to it. Further, the absolute spectral sensitivities of the photopic and scotopic visual systems are roughly equivalent at our stimulus wavelength (680 nm) (Wald, 1945). This fact is borne out in the results of Chapanis, who investigated the effect of stimulus wavelength on the dark adaptation curves of normal trichromats and found no rod-cone break when testing with 680 nm light, suggesting that rod contribution to visual sensitivity is equivalent to or less than cone input at this wavelength (Chapanis, 1947). As such, it is reasonable to question whether, and to what degree, the measures of visual sensitivity we report may be influenced by input from rod photoreceptors.

The roughly 0.65 log unit increase in visual threshold from 0° to 5° eccentricity shown in Figure 4.4A is slightly steeper than the findings of Stiles' testing with a stimulus of similar wavelength and size (Stiles, 1949). In that study, an increase in increment threshold of roughly 0.6 log units between 0° to 5° eccentricity was found in dark-adapted subjects when testing with a 10 arcmin, 700 nm stimulus. For the measures reported here, the subjects were not dark-adapted, and the AOM leak associated with the 680 nm test stimulus produced an equivalent background luminance of 1.05 cd/m^2, which falls within the mesopic light range. Given that the density of rod photoreceptors increases with eccentricity until about 18° from the fovea (Curcio et al., 1990), their relative contribution to the overall visual response to 680 nm light would be expected to increase with eccentricity. Therefore, one might interpret the steeper drop off in sensitivity observed in our data as the result of a dampened rod response induced by the mesopic test conditions. At any rate, this consideration carries less weight in the current incarnation of our AOSLO, where stimuli are presented at 543 nm (the point of equal sensitivity for L- and M-cones (Stockman and Sharpe, 2000)), and leak through the stimulus AOM can be adjusted easily to produce an adapting field of sufficient luminance—100 scotopic Trolands (Aguilar and Stiles, 1954)—to ensure testing in the photopic regime.

While the visual thresholds shown in Figure 4.4A increase with retinal eccentricity in the expected fashion, the data are noisy, and the source of this noise is unclear. For any perimeter, it is essential that variability—both within and between measurement sessions—be assessed thoroughly so that the examiner knows what magnitude of change in sensitivity may be deemed significant. One source of variability in the sensitivity data reported here is common to all perimeters: stimulus size. In standard automated perimetry, variability in measured thresholds increases as the perimetric stimulus size decreases (Gilpin et al., 1990; Vislisel et al., 2011). Normal variability in standard automated perimetry using Goldmann-I stimuli is on the order of ±3.5 dB (= 0.35 log units), which is in line with the data presented in Figure 4.5, although differences in the testing parameters—including background luminance, test wavelength, and modulation range—among different perimetry devices precludes us from making any direct comparisons.

4.5.3   Structure-Function Relationships in Retinitis Pigmentosa

Retinitis pigmentosa (RP) is part of a genetically heterogeneous group of inherited disorders that result in outer retinal degeneration (Wright et al., 2010). The prevalence of retinitis pigmentosa and its associated syndromes (e.g. Usher Syndrome) is estimated to be

approximately 1 in 4000, afflicting more than 1 million individuals worldwide (Bunker et al., 1984). The disease course of RP is characterized by the relentless loss of rod and cone photoreceptors (Mendes et al., 2005; Hartong et al., 2006). Clinically, RP manifests as night blindness and impaired dark adaptation during adolescence, followed by mid-peripheral visual field loss in young adulthood. In most cases, visual acuity—which is mediated by cones at the foveal center—remains unaffected until later stages (Holopigian et al., 1996). Ultimately, RP results in irreversible blindness due to photoreceptor death. There is no cure for RP, and treatments designed to mitigate its effects are limited (Hartong et al., 2006; Jacobson and Cideciyan, 2010).

The data from the early-stage RP patient presented in this chapter suggests normal structure and function persists in the parafoveal cone mosaic (Figure 4.8). This is not entirely surprising, as studies of the natural progression of RP have demonstrated that clinically significant changes in conventional measures of visual function—such as visual acuity or visual field—may not manifest until 7-10 years after diagnosis (Holopigian et al., 1996; Fishman et al., 2007). The relatively low prevalence and slow progression of RP are a major impediment for clinical trials aiming to evaluate novel RP treatments. Developing more sensitive measures of RP progression may reduce the time required to reveal a treatment effect in a clinical trial, thus lowering the cost of evaluating new therapeutic interventions and, by extension, advancing the treatment options available to the patient. With this in mind, it is worth discussing approaches which may reveal subtle RP-induced structural and functional changes in the cone mosaic that may go undetected by conventional techniques.

Currently, the leading candidate for detecting RP progression in its early stages is high resolution retinal imaging. The high-resolution modality most easily applied in the clinic is optical coherence tomography (OCT). Studies using OCT cross-sectional imaging have found distinct anatomical differences in RP patients compared to healthy controls, including reduced thickness of retinal layers associated with the photoreceptors (Hood et al., 2009; Rangaswamy et al., 2010) and diminished intensity of the inner segment/outer segment (IS/OS) band (Aizawa et al., 2008; Hood et al., 2011a; Hood et al., 2011b). To the first order, these anatomical markers appear to be coarsely related to conventional measures of visual function (Aizawa et al., 2008; Rangaswamy et al., 2010; Hood et al., 2011b; Wen et al., 2012; Birch et al., 2013; Cai et al., 2014).

However, relying solely on structural measures from OCT as a proxy for disease state or treatment efficacy is not without limitation. For example, outside the central fovea, both rod and cone photoreceptors will contribute to the signal forming the photoreceptor layers in OCT images, making it difficult to parse the relative effects of a novel treatment on the two receptor types. Second, it is unknown how sensitive OCT image features might be to the subtle changes associated with early-stage retinal disease, given that these layers only contain a handful of pixels to begin with (Hood et al., 2011a). Lastly, it is not clear if variation in the IS/OS band signal intensity conveys information about the relative number of photoreceptors present, their collective functional viability, or some combination of both.

More direct observation of cone and rod photoreceptors can be achieved with AOSLO, with which subtle reductions in cone density have been observed in patients with RP (Duncan et al., 2007; Talcott et al., 2011; Makiyama et al., 2013). In three patients with simplex RP and normal visual acuity, cone spacing in the parafovea was found to be normal (Duncan et al., 2007), consistent with the case report described in this chapter. Longitudinal observation of a group of 3 RP patients receiving unilateral ciliary neurotrophic factor treatment found a 9% greater reduction in cone density per year in the sham-treated eye compared to treated eye (Talcott et al., 2011). No significant changes in visual acuity, electroretinography findings, or visual field were observed in either eye over the 36-month study period.

These data support the contention that AOSLO imaging may be a highly sensitive marker of disease progression and, by extension, treatment effect in patients with inherited retinal degenerations. However the functional status of these preserved cones remains unclear. One possible explanation for this structure-function discrepancy is that the standard outcome measures for visual function may not possess the resolution or sensitivity required to quantify the functional impact of treatment. To best investigate the impact of a change in the photoreceptor mosaic, one must carefully choose a stimulus with which to probe photoreceptor function. For example, the identification of visual gratings sampled by degenerate-sampling arrays may remain unimpaired until 88% of the sampling elements are removed (Geller et al., 1992). In a similar vein, carefully-designed small-dot detection tasks revealed photoreceptor losses in subjects with clinically normal results on other tests of visual function, including automated perimetry (Geller and Sieving, 1993; Makous et al., 2006). Taken in combination, these results illustrate the need for functional tests and analytical tools designed to better reveal the relationship between photoreceptor structure and function in the parafoveal retina of normal subjects and patients with retinal disease.

4.5.4   Structure-Function Relationships in Age-related Macular Degeneration

Age-related macular degeneration (AMD) is the leading cause of blindness in individuals over age 65 in developed countries, and is characterized in its early stages by the presence of subretinal deposits (drusen) and retinal pigment abnormalities in the central retina (Jager et al., 2008; Lim et al., 2012). Progression of AMD may eventually involve the development of geographic atrophy (i.e. non-exudative/dry AMD), choroidal neovascularization (i.e. exudative/wet AMD), or both. In the parafovea, histological and psychophysical evidence suggests rod photoreceptors are selectively damaged in non-exudative AMD, which may in turn trigger cone loss at later stages (Curcio et al., 1996; Owsley et al., 2000). Adaptive optics imaging of the cone mosaic in age-related macular degeneration has yielded inconsistent results. A recent report employing a commercially-available adaptive optics retinal camera found marked drops in cone visibility over both subretinal drusenoid deposits and conventional drusen (Mrejen et al., 2014), but other investigators have found near-normal cone densities near the edges of geographic atrophy and over retinal drusen using AOSLO imaging (Zayit-Soudry et al., 2013).

Microperimetry studies on and around retinal drusen have generally found reduced sensitivity, particularly over large drusen (> 125 microns in diameter) (Takamine et al., 1998; Midena et al., 2007; Hartmann et al., 2011), with functional measures correlating to markers of photoreceptor integrity (i.e., IS/OS band) in OCT images (Hartmann et al., 2011). The data presented in Figure 4.9 are consistent with these findings, showing some image regions containing normal cone structure and sensitivity, and other areas where ambiguous structure is accompanied by reductions in sensitivity. The major difference between our approach and earlier studies is the improved stimulus control offered by AOSLO, which should facilitate better a better understanding of how function changes across structural abnormalities like drusen and borders of geographic atrophy.

4.6 Summary

We demonstrate in this chapter the feasibility of translating adaptive optics microperimetry to the clinical realm. From a research perspective, the advantages of conducting simultaneous retinal imaging and visual function testing with ASOLO are myriad, chief among them the ability to correlate retinal structure and function with cellular precision. In normal subjects, thresholds can be measured with good efficiency and repeatability, and stimuli can be delivered to the retina with single-cone precision. Findings from an early-stage patient with retinitis pigmentosa showed good agreement between imaged structure and visual function, consistent with our understanding of the natural course of this disease. In one patient with non-exudative age-related macular degeneration, we showed that adding functional testing to multimodal high-resolution imaging clarifies some of the structural ambiguity observed in the AOSLO image alone. The next chapter in this document builds upon these methods, which were used to reveal some interesting dissociations between structure and function in an inherited retinal disease, macular telangiectasia.

4.7 Acknowledgements

CHAPTER 5 – Structure-Function Dissociations in Macular Telangiectasia Type 2

5.1 Abstract

In the previous chapter, two case reports were presented wherein general agreement was found between outer retinal structure assessed by multimodal retinal imaging (AOSLO and OCT) and visual function measured with adaptive optics microperimetry (AOMP). The goal of this chapter is to highlight instances in which adaptive optics microperimetry (AOMP) reveals a dissociation between visual function and apparent retinal structure. Visual function and high-resolution retinal morphology were assessed in 3 patients from 2 unrelated families with macular telangiectasia (MacTel) type 2. AOSLO and AOMP were used to evaluate the structure and function of macular cones in 3 eyes with MacTel type 2, and registered spectral domain optical coherence tomography (SD-OCT) scans were used to aid the interpretation of ambiguous retinal structure observed in the AOSLO images. AOMP was used to measure visual sensitivity in and around areas of apparent cone loss in the AOSLO images. Although lesion surface area increased over time, some regions affected at visit one subsequently showed clear, contiguous, and normally-spaced cone mosaics with recovered photoreceptor inner/outer segment (IS/OS) reflectivity at the second visit. Measurable visual sensitivity was present everywhere except areas lacking an intact external limiting membrane (ELM) and featuring diffuse scattering in the IS/OS and posterior tips of the outer segments (PTOS) regions on OCT. Residual visual sensitivity measured in areas of apparent focal cone loss on AOSLO and OCT imaging suggests that MacTel type 2 lesions with a preserved ELM and underlying hypo-reflective zone (HRZ) may contain functioning cones with abnormal scattering characteristics. These findings highlight the importance of adopting a multi-modal approach when assessing the status of the diseased retina, and may prove useful in identifying candidates for novel therapeutic intervention, as well as tracking the efficacy of new treatment approaches.

5.2 Introduction

Macular telangiectasia (MacTel) type 2, also known as idiopathic juxtafoveolar telangiectasia type 2, is a rare bilateral but often asymmetric condition that causes marked visual disturbances such as impaired reading ability in patients over 40 years old (Finger et al., 2009). MacTel type 2 derives its name from the hallmark fluorescein angiography (FA) finding of telangiectatic retinal capillaries temporal to the fovea (Figure 5.1) (Gass and Oyakawa, 1982; Gass and Blodi, 1993; Yannuzzi et al., 2006). Affected eyes often exhibit photoreceptor inner-outer segment (IS/OS) junction disruptions and hyporeflective cavities on optical coherence tomography (OCT; (Sallo et al., 2012; Charbel Issa et al., 2013)).

While the Beaver Dam Eye Study reported the U.S. prevalence of MacTel type 2 as 0.1%, the disease is likely underdiagnosed due to the subtleties of early clinical manifestations as well as late-stage similarity to age-related macular degeneration (AMD; (Klein et al., 2010)). Compared to individuals affected by AMD and other eye diseases, those with MacTel type 2 have some of the lowest National Eye Institute Visual Functioning Questionnaire (NEI-VFQ-25) scores (Clemons et al., 2008; Clemons et al., 2010). It is unclear whether MacTel type 2 is

73

primarily vascular or neurodegenerative in origin (Charbel Issa et al., 2013), and there are no effective treatments for vision loss resulting from the disease.

Additionally, standard outcome measures of disease progression and treatment response are subjective and sometimes unreliable, leading to efforts to develop objective structural and functional characterization of the photoreceptors in MacTel type 2. Confocal AOSLO imaging in MacTel type 2 has shown disruption of the normal hexagonal cone mosaic pattern, leading to dark-appearing regions that correlate with characteristic IS/OS junction (or ellipsoid zone (EZ) band; (Staurenghi et al., 2014)) breaks seen on high-resolution OCT (Ooto et al., 2011). While prior studies have demonstrated visual function abnormalities in MacTel eyes with cone mosaic and IS/OS disruptions (Charbel Issa et al., 2013; Ooto et al., 2013), standard fundus-guided microperimetry methods use large retinal vascular landmarks to track the fundus and cannot assess retinal function with resolution commensurate with the individual cone structures imaged using AOSLO. Integrating microperimetry into AOSLO makes it possible to concurrently image cones and test their visual function in both an efficient and longitudinal manner (Chapter 4; (Tuten et al., 2012)). Such an approach, known as adaptive optics microperimetry (AOMP), has the potential not only to accurately distinguish between functional and dysfunctional cones in patients with MacTel type 2, but also to more precisely assess visual perception in areas of apparent cone loss. Compared to other retinal diseases characterized by focal disruptions (e.g., AMD), MacTel is particularly well-suited for AOMP testing because (1) disease onset occurs by middle age, before the natural development of media opacities that often make AOSLO imaging difficult, (2) central visual acuity is usually spared in the early stages, leaving patients with the relatively stable fixation needed for image-based eye tracking and stimulus delivery, and (3) lesions are typically surrounded by seemingly healthy retinal regions, allowing patients to serve as their own internal controls.

In this chapter, we examine cone structure and function in three patients mildly affected by MacTel type 2. We measure the progression of retinal structural changes in two patients and perform AOMP in all three patients at a single time point. The striking result regarding lesion progression is that clear, contiguous, normal-appearing, and normally-spaced cone mosaics appear in regions where no apparent cones were present at the first visit. Moreover, we find that in some regions lacking both visible cones on AOSLO and structural indicators of cone presence on OCT (IS/OS and posterior tips of the outer segments (PTOS) reflectivity), the retinas retain some visual function. Together, these findings suggest that there may be some functional intra-lesion cones that have the potential to recover normal scattering characteristics. An indicator of the presence of these reclaimable cones may be an intact external limiting membrane (ELM) that has is accompanied by a clear underlying hyporeflective zone (HRZ).

5.3 Methods

5.3.1 Participants

Three subjects with MacTel type 2 were enrolled at the University of California, Berkeley. Informed consent was obtained after the study protocol and its associated risks were reviewed

with each subject. The informed consent forms and study protocol were approved by the University of California San Francisco and University of California Berkeley Institutional Review Boards, and research procedures followed the tenets of the Declaration of Helsinki.

The participants were 2 women and 1 man from 2 unrelated families (F1P1, F2P1 and F2P2) with an average age of 48 at time of enrollment (Table 5.1). F1P1 and F2P1 were imaged at two time points (Table 5.1), but only structural imaging was done at visit one as the technology for AOMP had not been developed at the time. In the past year, all three patients were brought in for AOMP and imaging. Enrollment inclusion criteria included: 18 years of age or older, clinical signs of MacTel type 2, visual acuity of at least 20/40 in either eye, clear ocular media (cornea and lens), and fixation stability (ability to fixate on a target for at least 15 seconds). The study eye in each patient was selected based on clarity of OCT and AOSLO image quality.

Table 5.1| Study subject clinical characteristics. Information includes patient gender (F: female, M: male), age (years), study eye (SE), visual acuity (VA), manifest refraction (MR), and family history (FH). FU: follow up, BL: baseline. Other abbreviations used: optical coherence tomography (OCT), inner segment/outer segment junction band (IS/OS), not applicable (N/A).

Subject Characteristics							
Subject ID	Gender/ Age	SE	VA	MR (sphere, cylinder, axis)	Time since BL	Area of IS/OS loss on *en face* OCT	FH MacTel (Y/N)
F1P1	F/43	OS	BL: 20/16 FU: 20/32	-0.50DS	2 years	BL: 0.14 mm^2 FU: 0.17 mm^2	N
F2P1	F/49	OS	BL: 20/20 FU: 20/16	+1.25DS +0.25DC X 016	4 years	BL: 0.04 mm^2 FU: 0.28 mm^2	Y
F2P2	M/52	OD	BL: 20/20 FU: N/A	Plano	N/A	N/A	Y

5.3.2   Clinical measures

All subjects had undergone complete eye examinations by retinal specialists (PSB, SDS – see acknowledgements at the end of this chapter) within a few months of study enrollment. Clinical information gathered at these visits included best-corrected visual acuity (BCVA) measured according to the Early Treatment of Diabetic Retinopathy Study (ETDRS) protocol and converted to Snellen equivalent measures, color fundus photographs, fluorescein angiograms, and fundus autofluorescence images. The study eyes are shown in Figure 5.1.

For each study eye, pupil dilation was achieved with one drop of 1% tropicamide and one drop of 2.5% phenylephrine. Frame-averaged line scans, each comprised of 20 individual B-scans, were acquired with one of two Cirrus HD-OCT (Carl Zeiss Meditec, Inc; Dublin, CA) retinal

imaging systems. Macular cube volume scans were acquired with either the commercially available 512x128 cube protocol covering 6mm^2, or a proprietary 256x256 cube protocol covering 3mm^2. A line-scanning ophthalmoscope integrated into the Cirrus system obtained infrared fundus scans simultaneously with the SDOCT acquisition and was used to indicate scan position. *En face* OCT scans were derived from IS/OS slabs that were between 43 and 45 microns thick using an RPE-based geometry. Within these *en face* scans, a significant decrease in reflectivity indicated a disruption of the normal IS/OS. The surface area of such defects was measured manually using ImageJ (http://rsbweb.nih.gov/ij/) (Table 5.1).
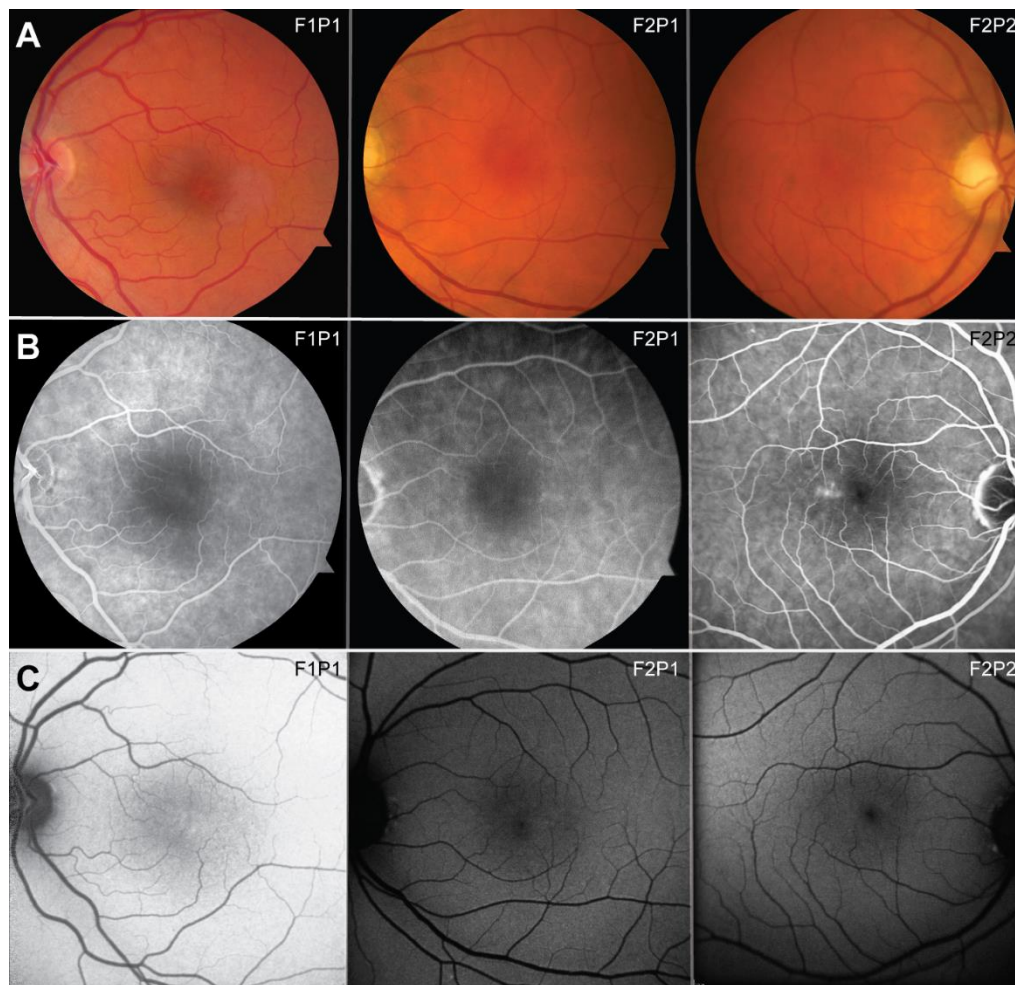

Figure 5.1| Clinical findings in patients with macular telangiectasia type 2. Color fundus photos (row **A**) reveal subtle MacTel type 2 features such as loss of retinal transparency and telangiectatic vessels temporal to the fovea. These are more clearly seen with evidence of hyperfluorescence on fluorescein angiogram images (row **B**) and fundus autofluorescence images (row **C**).

5.3.3 AOSLO imaging and AOMP testing

High-resolution AOSLO images were obtained from each study eye using an AOSLO as previously described (Chapters 1-4; (Duncan et al., 2007; Merino et al., 2011; Talcott et al., 2011)). Individual AOSLO images, which covered 1.2° x 1.2° of retina, were assembled into larger montages that encompassed the fovea, the macular area with IS/OS junction band disruption, and surrounding normal appearing cones in each imaged eye. The appearance of the images in the immediate vicinity of the lesions fell into three categories:

- **N:** normal appearing cone mosaics on AOSLO, presence of normal appearing ELM, IS/OS and PTOS on OCT.
- **D**: weakly reflecting or no cones visible on AOSLO; presence of ELM, IS/OS and PTOS but IS/OS and PTOS appear relatively dim or disrupted.
- **R**: RPE cells, but no cone mosaic is visible on AOSLO; IS/OS and PTOS are not present, ELM may or may not be present.

Using information shown in SD-OCT images and AOSLO montages, specific 0.1° x 0.1° retinal regions of interest (ROIs) were manually selected for AOMP functional testing. AOMP tests were done at **N**, **D** and **R** sites, all of which were located between 0 and 185 arcminutes (0° and 3.1°) from the preferred retinal locus (PRL), presumed to be the anatomical fovea. **N** category AOMP test sites across all 3 eyes provided normative data against which thresholds values in all eyes were compared.

AOMP was implemented as described in Chapter 4 of this document. The stimulation wavelength (λ = 543 nm) was selected on the basis that it drives L and M cones—which make up 90-95% of the cone receptor mosaic—equally (Stockman and Sharpe, 2000). The stimulus diameter was roughly half that of a Goldmann I-sized stimulus (3.45 arcmin), and its area would span between 43 (at the fovea) and 5 (at 3°) cones in a normal retina (Curcio et al., 1990). To ensure accuracy of stimulus delivery to a given AOMP test site, locations were visualized using dynamic AOSLO imaging and tracked by a high-speed image-based eye tracking algorithm, which predicted the precise moment to deliver the stimulus (Arathorn et al., 2007; Yang et al., 2010). Additionally, transverse (TCA) chromatic aberration was measured and corrected according to established methods when image quality permitted (Harmening et al., 2012); in other cases, the TCA was minimized by asking the subject to fixate the imaging and stimulus rasters and adjusting pupil position until the two were brought into subjective alignment.

Visual sensitivity was assessed via an increment threshold approach. Light leaking through the stimulus channel provided a background of ~4 cd/m^2, bright enough to prevent rod photoreceptors from contributing to the measured thresholds (Aguilar and Stiles, 1954). Stimulus intensity was represented in arbitrary units (au) on a linearized scale from 0 to 1; a value of 0 indicates the presence of the background only; an intensity of 1 represents the strongest light the system is capable of presenting (for more, see Appendix 1). AOMP results were generated using a subject-paced 4-2 dB staircase with yes-no response paradigm (Chapter 4; see also (Artes et al., 2002)). At each AOMP test site, the subject pushed a button to initiate a

staircase, which typically consisted of 12-15 trials and was repeated 3 times per retinal test site. A trial involved the following sequence of events: successful stimulus delivery, signaled by an auditory cue; subject's "yes" or "no" keyboard response; subject's initiation of the next trial. Trials with failed stimulus delivery were repeated immediately, and each retinal test site ultimately underwent a total of 36-45 trials.
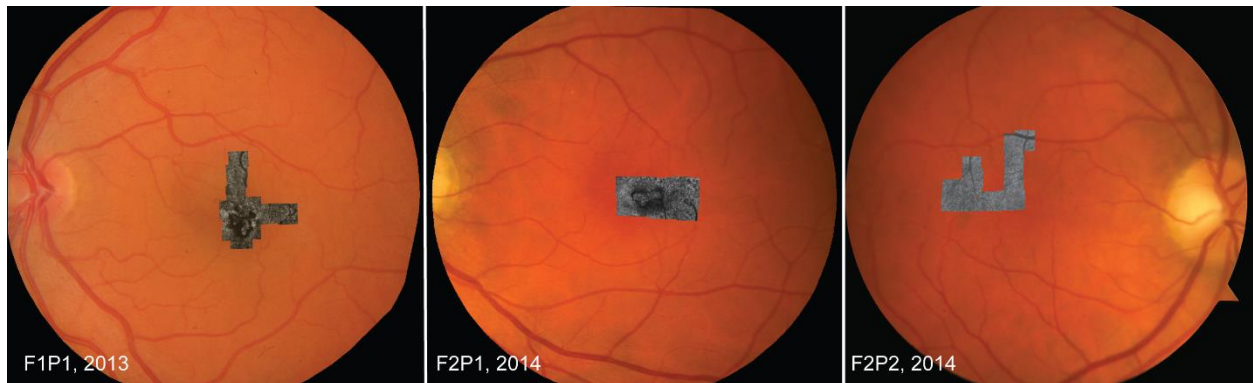

Figure 5.2| AOSLO montages superimposed on clinical images. Relative location and size of MacTel type 2 lesions are shown for all three subjects. In F2P2, the patient with earliest disease, telangiectatic vessels temporal to the fovea are the only abnormal findings.

5.3.4   Image Overlays

Comprehensive image overlays were generated (Adobe Illustrator, San Jose, CA) to contextualize OCT, AOSLO, and AOMP measures. AOMP retinal test sites were marked on respective AOSLO montages, which were then correlated precisely with clinical images demonstrating the MacTel type 2 lesions (Figure 5.2). *En face* OCT slab images of IS/OS layers and single cross-sectional OCT B scans, along with corresponding scan lines, were subsequently superimposed on AOSLO montages and precisely registered using the study eye's lesion appearance and vascular anatomy.

5.3.5   Cone Spacing

Cone spacing was measured at locations with unambiguous arrays of contiguous cones and avoided where cones may have been obscured by inner retinal pathology. Using the methods previously described (Rodieck, 1991b; Talcott et al., 2011), cone spacing was estimated via custom software (Matlab, MathWorks, Natick, MA), which extracts the nearest neighbor distance based on a histogram of all intercone distances from subsets of cones at 43 locations. Study eye values were compared to values from 27 age-similar healthy eyes. Selected locations included 10 of the 13 N category AOMP test sites.

5.3.6   AOMP Data Analysis and Statistical Methods

Among the 3 study eyes, a total of 22 retinal test sites were tested using AOMP. 13 out of these 22 sites were in the **N** category, 4 in the **D** category, and 5 in the **R** category. During the course of AOMP testing, an individual retinal site generated a series of thresholds; these values were averaged into a single measured threshold value for each test site. Linear regression analysis of thresholds at **N** sites across all 3 eyes was used to determine expected threshold values for normally-functioning cones at any given eccentricity. A p value < 0.05 was considered to be statistically significant. Expected thresholds were used as normal values against which measured threshold values at all 22 retinal test sites were compared.

5.4   Results

5.4.1   Progression

For study eyes F1P1 and F2P1, past AOSLO montages were used to examine lesion progression. Comparison of current and previous AOSLO montages showed that there was significant expansion of lesion boundaries in both eyes (Table 1). In F1P1, the lesion expanded nasally to include the original PRL, forcing the subject to adopt a slightly eccentric PRL (Figure 5.3A and B). This eye also experienced a decrease in VA from 20/16 to 20/32 (Table 1). In F2P1, the lesion, which at the first visit started 2° temporal to fixation, expanded nasally to reach the anatomical fovea (Figures 5.3C and D). The PRL and acuity in this patient remained stable between visits. The most striking change was that in both F1P1 and F2P1, subsequent visits showed clear and contiguous arrays of cones in some previously affected intra-lesion regions. The OCT images showed corresponding recovery of the reflections consistent with the IS/OS junction and the PTOS. (Figure 5.3A-D).

5.4.2   Structural Characterization

At 41/43 locations where unambiguous cones were observed (10/41 were AOMP **N** category sites), cone spacing values fell within the 95% confidence interval of the normal mean, which was calculated using values from 27 healthy eyes. These locations with normal values included 4 areas within newly-resolvable cone arrays. The remaining 2/43 locations had spacing values in the 99% confidence interval. In 2 out of 3 study eyes (F1P1 and F2P1), *en face* OCT slab images containing the IS/OS showed dark MacTel type 2 lesions that correlated well in size and shape with the lesions seen on corresponding AOSLO montages. On cross-sectional OCT B scans, the reflectivity of the IS/OS lines within the lesions were relatively dim or absent compared to outside the lesions. B scans in F1P1 (Figure 5.4A, white arrowheads, scans e and f) revealed a relatively preserved ELM line with an underlying HRZ where the IS/OS and PTOS would normally be seen, while in F2P1 these distinctions were less clear (Figure 5.4B, white arrowhead, scan c). In F2P2, there was no discontinuity in the cone mosaic or in the IS/OS or ELM bands, although shadows of inner retinal abnormalities were seen in the AOSLO montage (Figure 5.4C) and telangiectatic vessels were observed temporal to the fovea on fluorescein angiography (Figure 5.1B).
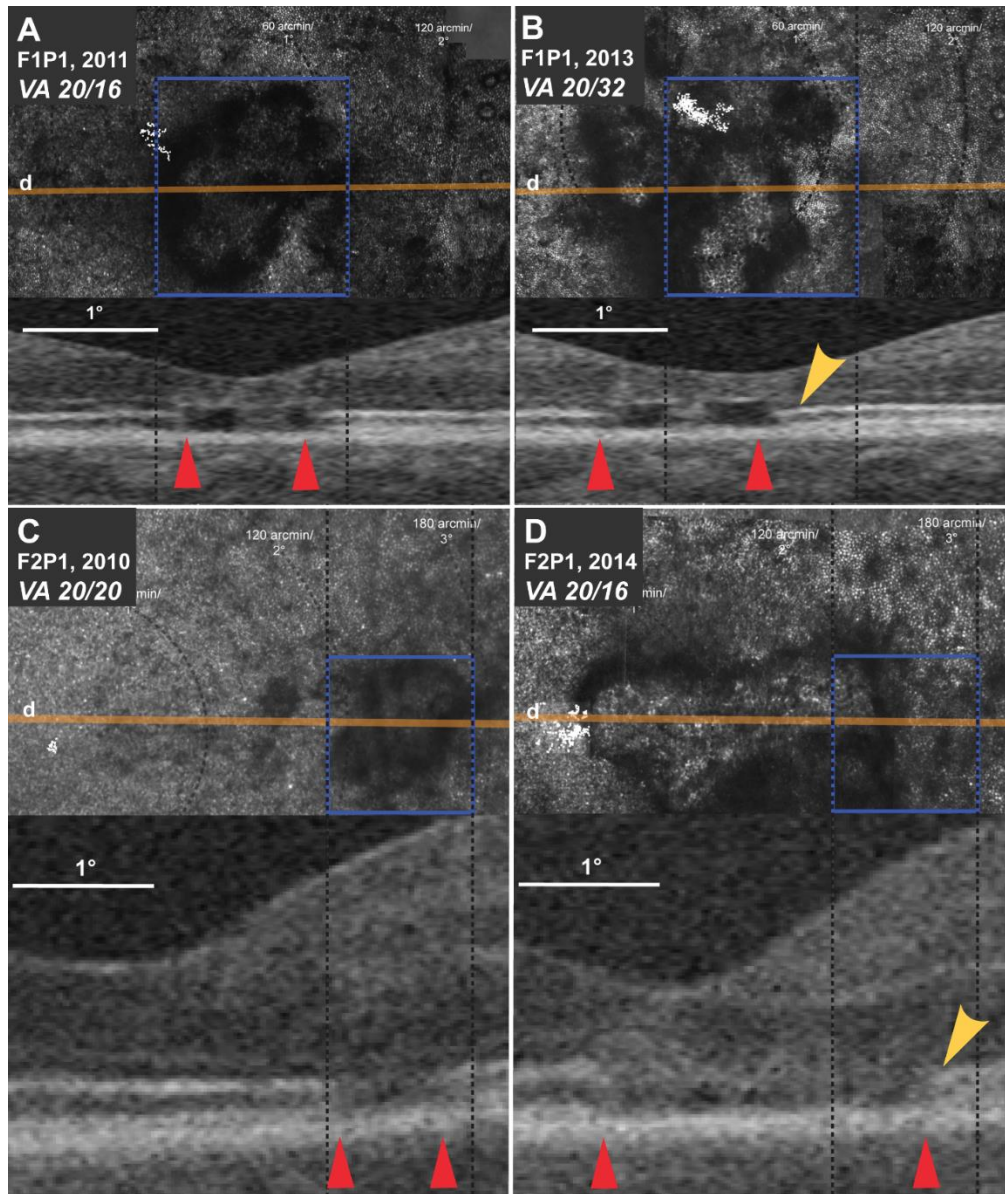
Figure 5.3| Disease progression in 2 MacTel type 2 patients. Baseline lesion boundaries are outlined in blue on AOSLO and correlated with OCT B scans via black, vertical dashed lines. Visual acuity (VA), preferred retinal loci (PRL, white clusters), and IS/OS breaks on OCT (red arrowheads) are shown. **A, B) AOSLO (top row)**: There is nasal expansion from 2011 to 2013. Within the blue rectangle, there are newly-resolvable, hyper-reflective cones temporally that are not seen in **5.3A**. **A, B) OCT (bottom row)**: Selected scan shows anatomy at all 3 AOSLO-defined categories (N, D, R). The reflectivity of the IS/OS line within the lesion is relatively dim compared to outside the lesion. In **5.3A**, the dashed vertical lines do not correspond exactly with IS/OS breaks. In **5.3B**, the same dashed lines show that temporally, a small, previously dark IS/OS segment in 2011 is hyper-reflective in 2013 (yellow arrow). **A, B) VA, PRL**: The decline in VA coincides with a shift in PRL. **C, D) AOSLO**: There is nasal extension from 2010 to 2014. Within the blue rectangle, there are apparent cones in a formerly dim region temporal to the vertical retinal vascular landmark. **C, D) OCT**: The IS/OS defect has increased and extended nasally. A small, previously dark IS/OS segment in 2010 appears hyper-reflective in 2014 (yellow arrow). Note: The difference in foveal contours between **5.3C** and **5.3D** is likely due to loss of outer retinal layers, as demonstrated in Figure 5.4B, B-scans **a** through **e**. **C, D) VA, PRL**: VA stable, PRL center unchanged during the course of the study.

5.4.3 Functional Characterization

The AOMP thresholds measured at all 13 **N** sites increased with increasing eccentricity (Figure 5.4D; slope = 0.054 au/degree, R^2 = 0.77, p < 0.0001), demonstrating that for normal-appearing cones, visual sensitivity decreases with increasing distance from the fovea at a similar rate for all three subjects. All 9 AOMP test sites in the **D** and **R** categories were measured in subjects F1P1 and F2P1, while the third study eye (F2P2) had only **N** category retinal test sites (Figure 5.4A-C). Of 4 **D** sites tested in regions with dimly-reflecting cones, 3 produced average threshold values at least twofold greater than normal, corrected for eccentricity. Of the 5 **R** sites tested where RPE cells were visible, average threshold values were at least twofold greater than normal at 2 sites and fourfold greater than normal at the other 2 (see color scale on Figure 5.4A.
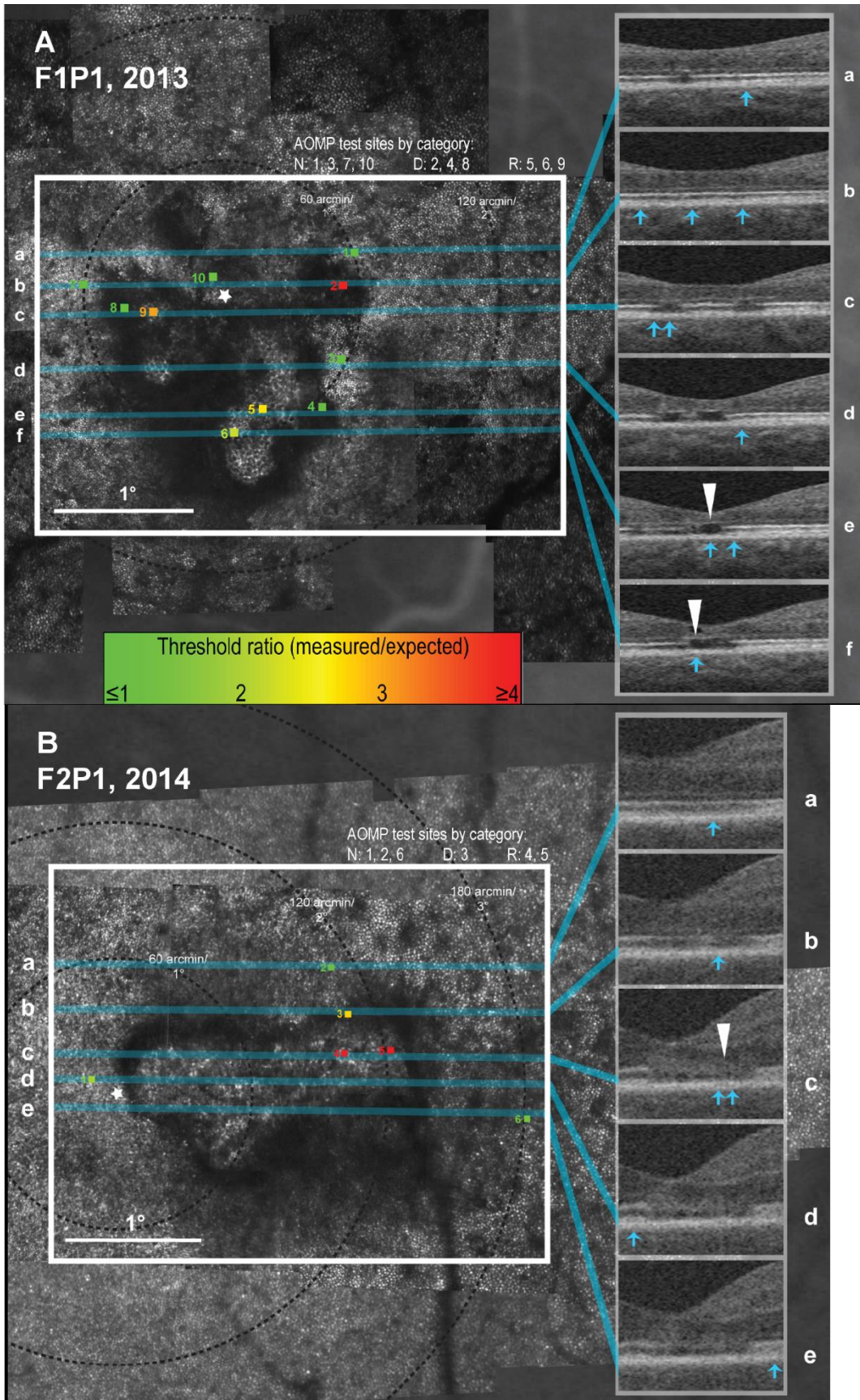
5.5 Discussion

This is the first report of recovered visibility of contiguous cone arrays within regions that had previously been identified as being within a lesion. This is also the first report showing measurable function in recovered regions as well as regions where no cones were visible on either OCT or AOSLO imaging. These new findings have challenged our notion that regions with no visible cones on OCT or AOSLO lacked cones as well as visual function, leading to the following questions:

1. Cone structure: What is the nature of the recovery of cone visibility? Are cones migrating into this region; are new cones forming; or is there a recovery of structure and corresponding reflections from cones that were always present?
2. Cone function: What the best explanation for the existence of light sensitivity in areas where no cones are visible on AOSLO and which lack visible structures consistent with the IS/OS and the PTOS in OCT?

5.5.1 Cone Structure

In this series of MacTel type 2 patients, cone spacing is normal in nearly all sites with contiguous and unambiguous arrays of cones. Specifically, the cones that regained visibility had normal spacing (2 out of 2 eyes). If these cones had migrated into their respective lesions, there would have been a corresponding increase in spacing (decrease in local density) in the general vicinity as more normal cones moved into empty spaces to replace lost cones. In fact, the comprehensive image overlays showed that, when comparing across the two visits, cone mosaic regions near the lesion matched cone-to-cone, indicating that the newly-observed cones were not migrating from nearby regions (2 out of 2 eyes). These two findings rule out migration as an explanation for the newly visible cones.

A
F1P1, 2013

AOMP test sites by category:
N: 1, 3, 7, 10   D: 2, 4, 8   R: 5, 6, 9

60 arcmin/1°   120 arcmin/2°

a
b
c
d
e
f

1°

Threshold ratio (measured/expected)
≤1   2   3   ≥4

a
b
c
d
e
f

B
F2P1, 2014

AOMP test sites by category:
N: 1, 2, 6   D: 3   R: 4, 5

120 arcmin/2°   180 arcmin/3°

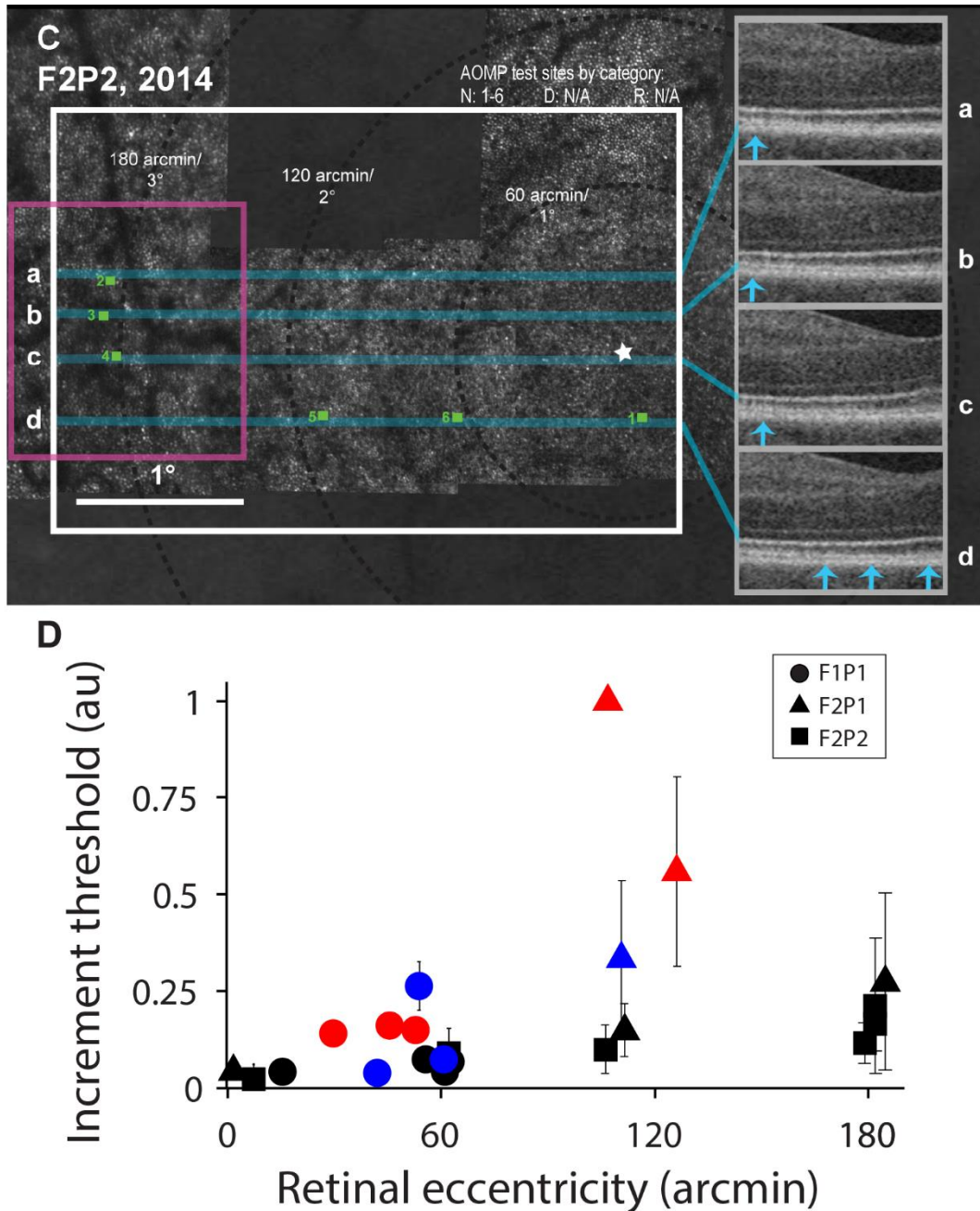60 arcmin/1°

a
b
c
d
e

1°

a
b
c
d
e

82

Figure 5.4| Cone structure and function in MacTel type 2 study eyes. Each panel (**A-C**) shows AOSLO montages, OCT scan lines, OCT B scans, AOMP test site locations (colored squares, actual test stimulus size), and average AOMP threshold values [reported in arbitrary units (au)]. Extent of threshold elevation compared to expected indicated by color. White stars mark foveas and scale bars = 1°. B scans were scaled and registered with vasculature prior to miniaturization (33% original). Scans show retinal anatomy at AOMP test sites (blue arrows). **5.4A**) AOSLO: MacTel type 2 lesion with RPE cells (R sites) and dim areas (D sites). OCT (**a-f**): IS/OS breaks appear to have overlying preserved ELM bands (white arrows). RPE areas correspond to definitive IS/OS breaks on B scans. Dim areas correspond with a range of IS/OS findings: test site 9 corresponds to an unambiguous break; 2, 4 and 8 to a present but often relatively weakly reflecting IS/OS. AOMP: Measureable threshold values (au ± 1 S.D.) at RPE sites are less abnormal than value at D site 2. **5.4B**) AOSLO: Visible RPE mosaics and dimly-reflecting regions. OCT (**a-e**): Concurrent IS/OS and ELM disruptions (white arrow) correspond to AOMP R sites (4, 5), while D site 3 co-

83

localizes with a present but weakly reflective IS/OS. AOMP: R site thresholds exceed thresholds in normal-appearing and dim areas. **5.4C)** AOSLO: Shadows of inner retinal abnormalities (pink rectangle). OCT (**a-d**): No disruption of the IS/OS junction band or ELM band. AOMP: Thresholds increased with eccentricity, with site 3 elevated more than site 2 or 4. **5.4D)** AOMP thresholds from all 3 study eyes are shown as a function of retinal eccentricity. Thresholds at normal (N, black) locations increase with eccentricity and serve as comparison for thresholds at dim (D, blue) and RPE (R, red) sites. Symbol shapes denote subject.

While the regrowth of entirely new cones is unlikely, it is possible for a cone to persist without the normal structures that give rise to the IS/OS and PTOS reflections. These reflections not only account for their visibility on OCT, but also on AOSLO images. Therefore, it is conceivable that cones with abnormal outer segments experience a loss of visibility and a corresponding reduction, but not complete loss, of function. Indeed, two recent reports in the literature support the possibility of cones in regions where they are not visible in AOSLO or OCT. First, recent results from an AOSLO employing a novel split-detection scheme has shown visible structures consistent with mosaics of inner segments in regions where standard confocal AOSLO imaging fails to show anything (Scoles et al., 2014). Second, a case report showed histologically normal-appearing cones within regions of IS/OS breaks, providing evidence that in MacTel type 2, breaks in the IS/OS junction may indicate conditions that disrupt the IS/OS cone reflectivity rather than reveal photoreceptor death (Powner et al., 2013). Neither of these analyses were done on our patients, however, as the new split-detector technology does not presently exist in our lab, and the histological analysis necessarily requires post-mortem tissue.

Nevertheless, there are findings on the OCT images that might suggest the presence of a mostly intact cone array. Between the F1P1 and F2P1 study eyes, OCT B scans revealed a consistent anatomical difference—in F1P1, the B scans showed a relatively preserved ELM overlying an HRZ where the IS/OS and PTOS would normally be seen (Figure 5.4A, white arrowheads), while in F2P1 they showed less evidence of an ELM where no IS/OS was visible (Figure 5.4B, white arrowheads). The ELM, which consists of zonular adherences between Müller cell processes and photoreceptor inner segments, is believed to play an integral role in maintaining photoreceptor orientation and alignment (Mitamura et al., 2013). Interestingly, the ELM band typically persists after IS/OS loss in other retinal degenerations such as retinitis pigmentosa (RP), choroideremia (CHM), and Stargardt disease (STGD) (Mitamura et al., 2013). Also, previous studies of postoperative recovery following macular hole (MH) closure as well as retinal detachment (RD) repair have found without exception that ELM restoration preceded that of the IS/OS junction and that no eyes experienced IS/OS restoration without complete ELM recovery (Ooka et al., 2011; Mitamura et al., 2013).

An intact ELM that is accompanied by a transparent HRZ could indicate intra-lesion regions where cones are present and retain most of their structure. Recent retinal imaging studies conducted with OCT support this idea: HRZs have been found in the central fovea of roughly 25-50% of patients with achromatopsia (Thiadens et al., 2010; Thomas et al., 2011; Sundaram et al., 2014). Interestingly, the presence of a foveal HRZ does not seem to correlate with visual acuity (Thomas et al., 2011; Sundaram et al., 2014), which suggests that viable cones may persist in these regions. More recently, split detector AOSLO imaging in one patient with

achromatopsia confirmed the presence of intact cone photoreceptor inner segments at retinal loci co-localized with an HRZ on OCT, despite the apparent absence of cones in the corresponding confocal AOSLO image (Scoles et al., 2014). Taken together, these retinal imaging findings—in combination with the AOMP results discussed in the following section—suggest that an HRZ may indicate the presence of viable cones within an apparent retinal lesion, in spite of the lack of commonly-adopted markers of cone integrity (IS/OS band, reflectivity on confocal AOSLO imaging) associated with high-resolution imaging modalities.

5.5.2   Cone Function

Further evidence of the presence of abnormal and non-visualizable cones is found in our microperimetry results. Visual sensitivity was found in both the **D** and **R** regions. In F1P1, the **R** site (locations 5, 6 and 9) values were only ~twofold higher than expected, suggesting relatively preserved visual sensitivity at those locations with visible RPE cell mosaics. In this eye, the AOMP test site with the most abnormal threshold value was located at a **D** site (location 2), indicating better visual sensitivity at **R** sites with visible RPE cells than **D** sites with dimly visible cones. In F2P1, the two **R** sites (locations 4 and 5) produced the most elevated thresholds observed but only location 4 had thresholds that exceeded the limits of the AOMP system (more than 8 times higher than expected). These findings contradict conventional beliefs that visualization of RPE cell mosaics and the loss of IS/OS and PTOS reflectivity indicate a complete absence of cones and a corresponding inability to perceive light (Roorda et al., 2007). While it is very likely that there are many cases where this is true, it does not apply to the examples shown in this study.

The AOMP data from F1P1 and F2P1 indicate that the structural scaffolding provided by an intact ELM may also be integral to preserving cones that maintain their visual sensitivity in regions where the IS/OS junction is disrupted. In other words, lesions with preserved ELM and corresponding inner segments may contain functional cones. The presence of measurable AOMP thresholds raises the possibility that rather than being truly absent, such intra-lesion cones may have abnormal scattering and/or waveguiding qualities that preclude their visibility on confocal AOSLO imaging.

It also is possible that the threshold values seen at AOMP **R** test sites (locations 5, 6 and 9 in F1P1) represent responses by more normal neighboring cones stimulated as a result of intra-retinal scatter. However, given that a **D** site in F1P1 (location 2) showed a high threshold in the immediate vicinity of two **N** regions and that **R** sites in F2P1 (locations 4 and 5) produced severely elevated thresholds despite being located at similar distances from normal-appearing cones, it is unlikely that scattered light contributed significantly to the relatively low threshold values observed in F1P1. Moreover, in a separate study using the same system on normal eyes, intra-retinal forward scattering did not appear to contribute to the observed changes in retinal sensitivity of cone-sized stimuli placed between versus on individual cones (Harmening et al., 2014).

5.6   Conclusions and Summary

In conclusion, we used a multi-modal approach to characterize structure and function in the parafoveal cone mosaics of three patients with MacTel type 2. Taken together, the confocal AOSLO images and OCT b-scans suggest focal lesions entirely devoid of cone photoreceptors; however, the high-resolution functional testing afforded by AOMP revealed measurable photopic sensitivity within their borders. In comparison to other disease states (see Chapter 4), this disconnect between structure and function was unexpected, but close examination of the cross-sectional OCT images revealed a correlation between the presence of an intact ELM with an underlying HRZ and areas of preserved visual sensitivity. Further, longitudinal imaging in patient F1P1 suggests that, over time, some intralesion cones may regain their normal scattering characteristics and once again become observable with AOSLO and OCT. In summary, the findings in this chapter highlight the utility of adding functional testing to advanced imaging methods when attempting to locate and assess regions of functional cones in diseased retinas, and could prove especially useful when the goal is to identify cones that may prove amenable to novel therapeutic interventions.

5.7   Acknowledgements

DISSERTATION SUMMARY

The primary aim of the studies described in this document was (1) to validate the tools developed in the Roorda laboratory to simultaneously image and stimulate the retina with cellular resolution and precision, and (2) to apply these methods to the study of cone-mediated vision in healthy subjects and patients with retinal disease. Using an adaptive optics scanning laser ophthalmoscope equipped with high-speed eye tracking and multi-wavelength stimulus delivery capabilities, we were able to reveal a sensitivity gradient that matches the spatial grain of the photoreceptor mosaic in the parafovea. This is the most direct evidence yet that studying vision on a cellular scale is indeed possible, and sets the stage for a host of interesting experiments aimed towards establishing the perceptual sequelae of stimulating individual receptors.

By measuring single-cone thresholds under polychromatic conditions, we were able to accurately identify long wavelength-sensitive cones residing in the interleaved trichromatic cone mosaic. Comparing our functional maps of the trichromatic cone mosaic to those obtained via established, image-based methods, we found a high level of agreement, and closer examination of our data suggested that cone thresholds may be influenced by elevated activity in nearby receptors. These results suggest that measuring thresholds under carefully-manipulated background conditions may be an avenue for unraveling the manner in which individual cone signals interact in the visual circuitry.

Lastly, we sought to translate these tools to the clinical environment by developing adaptive optics microperimetry. The benefit of imaging and stimulating the retina with high-resolution is that the functional correlates of cone structure can be established with improved confidence. In outer retinal disease, we found that visual function measured in and around retinal lesions generally agreed with the structural markers of cone integrity obtained via multi-modal high-resolution imaging. In another disease—macular telangiectasia type 2—we found evidence for functioning cones persisting within lesions entirely devoid of conventional image-based indicators of photoreceptor integrity. Despite their surprising nature, these results are supported by recent histological reports, as well as findings with new high-resolution imaging paradigms. Taken together, our efforts underscore the utility of adding functional testing to structural assessment in cases where retinal morphology is ambiguous.

REFERENCES

Adams DL, Horton JC (2002) Shadows cast by retinal blood vessels mapped in primary visual cortex. Science 298:572-576.

Aguilar M, Stiles WS (1954) Saturation of the Rod Mechanism of the Retina at High Levels of Stimulation. Optica Acta: International Journal of Optics 1:59-65.

Ahnelt PK, Kolb H, Pflug R (1987) Identification of a subtype of cone photoreceptor, likely to be blue sensitive, in the human retina. Journal of Comparative Neurology 255:18-34.

Aizawa S, Mitamura Y, Baba T, Hagiwara A, Ogata K, Yamamoto S (2008) Correlation between visual function and photoreceptor inner/outer segment junction in patients with retinitis pigmentosa. Eye 23:304-308.

Anderson SJ, Mullen KT, Hess RF (1991) Human peripheral spatial resolution for achromatic and chromatic stimuli: limits imposed by optical and retinal factors. J Physiol 442:47-64.

Arathorn DW, Yang Q, Vogel CR, Zhang Y, Tiruveedhula P, Roorda A (2007) Retinally stabilized cone-targeted stimulus delivery. Optics express 15:13731-13744.

Artes PH, Iwase A, Ohno Y, Kitazawa Y, Chauhan BC (2002) Properties of perimetric threshold estimates from Full Threshold, SITA Standard, and SITA Fast strategies. Invest Ophthalmol Vis Sci 43:2654-2659.

Atchison DA, Smith G (2005) Chromatic dispersions of the ocular media of human eyes. J Opt Soc Am A Opt Image Sci Vis 22:29-37.

Babcock HW (1953) The possibility of compensating astronomical seeing. Publications of the Astronomical Society of the Pacific 65:229-236.

Barlow HB (1953) Summation and inhibition in the frog's retina. J Physiol 119:69-88.

Barlow HB (1958) Temporal and spatial summation in human vision at different background intensities. J Physiol 141:337-350.

Baylor DA, Fuortes MG, O'Bryan PM (1971) Receptive fields of cones in the retina of the turtle. J Physiol 214:265-294.

Baylor DA, Nunn BJ, Schnapf JL (1987) Spectral sensitivity of cones of the monkey Macaca fascicularis. J Physiol 390:145-160.

Bedggood P, Metha A (2012a) Direct visualization and characterization of erythrocyte flow in human retinal capillaries. Biomedical optics express 3:3264-3277.

Bedggood P, Metha A (2012b) Variability in bleach kinetics and amount of photopigment between individual foveal cones. Invest Ophthalmol Vis Sci 53:3673-3681.

Bedggood P, Metha A (2013) Optical imaging of human cone photoreceptors directly following the capture of light. PLoS One 8:e79251.

Bedggood P, Daaboul M, Ashman R, Smith G, Metha A (2008) Characteristics of the human isoplanatic patch and implications for adaptive optics retinal imaging. Journal of biomedical optics 13:024008.

Birch DG, Sandberg MA, Berson EL (1982) The Stiles-Crawford effect in retinitis pigmentosa. Invest Ophthalmol Vis Sci 22:157-164.

Birch DG, Locke KG, Wen Y, Locke KI, Hoffman DR, Hood DC (2013) Spectral-domain optical coherence tomography measures of outer segment layer progression in patients with X-linked retinitis pigmentosa. JAMA ophthalmology 131:1143-1150.

Bland JM, Altman DG (1986) Statistical methods for assessing agreement between two methods of clinical measurement. Lancet 1:307-310.

Bölinger D, Gollisch T (2012) Closed-loop measurements of iso-response stimuli reveal dynamic nonlinear stimulus integration in the retina. Neuron 73:333-346.

Bowl W, Lorenz B, Jaeger M, Friedburg C (2013) Improving detection of mild loss of retinal light increment sensitivity at the posterior pole with the microperimeter MP1. Invest Ophthalmol Vis Sci 54:4666-4674.

Boynton RM, Clarke FJ (1964) Sources of Entoptic Scatter in the Human Eye. Journal of the Optical Society of America 54:110-119.

Boynton RM, Whitten DN (1970) Visual adaptation in monkey cones: recordings of late receptor potentials. Science 170:1423-1426.

Brainard DH, Williams DR, Hofer H (2008) Trichromatic reconstruction from the interleaved cone mosaic: Bayesian model and the color appearance of small spots. J Vis 8:15 11-23.

Brainard DH, Roorda A, Yamauchi Y, Calderone JB, Metha A, Neitz M, Neitz J, Williams DR, Jacobs GH (2000) Functional consequences of the relative numbers of L and M cones. J Opt Soc Am A Opt Image Sci Vis 17:607-614.

Brindley GS, Du Croz JJ, Rushton WA (1966) The flicker fusion frequency of the blue-sensitive mechanism of colour vision. J Physiol 183:497-500.

Bunker CH, Berson EL, Bromley WC, Hayes RP, Roderick TH (1984) Prevalence of retinitis pigmentosa in Maine. Am J Ophthalmol 97:357-365.

Burns SA, Marcos S, Elsner AE, Bara S (2002) Contrast improvement of confocal retinal imaging by use of phase-correcting plates. Optics letters 27:400-402.

Cai CX, Locke KG, Ramachandran R, Birch DG, Hood DC (2014) A Comparison of Progressive Loss of the Ellipsoid Zone (EZ) Band in Autosomal Dominant and X-linked Retinitis Pigmentosa. Invest Ophthalmol Vis Sci:IOVS-14-15013.

Campbell FW, Green DG (1965) Optical and retinal factors affecting visual resolution. J Physiol 181:576-593.

Campbell FW, Gubisch RW (1966) Optical quality of the human eye. J Physiol 186:558-578.

Campbell MC, Harrison EM, Simonet P (1990) Psychophysical measurement of the blur on the retina due to optical aberrations of the eye. Vision Res 30:1587-1602.

Carroll J, Neitz J, Neitz M (2002) Estimates of L:M cone ratio from ERG flicker photometry and genetics. J Vis 2:531-542.

Carroll J, Kay DB, Scoles D, Dubra A, Lombardo M (2013) Adaptive optics retinal imaging--clinical opportunities and challenges. Curr Eye Res 38:709-721.

Carroll J, Rossi EA, Porter J, Neitz J, Roorda A, Williams DR, Neitz M (2010) Deletion of the X-linked opsin gene array locus control region (LCR) results in disruption of the cone mosaic. Vision Res 50:1989-1999.

Chapanis A (1947) The Dark Adaptation of the Color Anomalous Measured with Lights of Different Hues. The Journal of general physiology 30:423-437.

Charbel Issa P, Gillies MC, Chew EY, Bird AC, Heeren TF, Peto T, Holz FG, Scholl HP (2013) Macular telangiectasia type 2. Progress in retinal and eye research 34:49-77.

Chen B, Makous W, Williams DR (1993) Serial spatial filters in vision. Vision Res 33:413-427.

Cicerone CM, Nerger JL (1989a) The relative numbers of long-wavelength-sensitive to middle-wavelength-sensitive cones in the human fovea centralis. Vision Res 29:115-128.

Cicerone CM, Nerger JL (1989b) The density of cones in the fovea centralis of the human dichromat. Vision Res 29:1587-1595.

Clemons TE, Gillies MC, Chew EY, Bird AC, Peto T, Figueroa M, Harrington MW (2008) The National Eye Institute Visual Function Questionnaire in the Macular Telangiectasia (MacTel) Project. Invest Ophthalmol Vis Sci 49:4340-4346.

Clemons TE, Gillies MC, Chew EY, Bird AC, Peto T, Figueroa MJ, Harrington MW (2010) Baseline characteristics of participants in the natural history study of macular telangiectasia (MacTel) MacTel Project Report No. 2. Ophthalmic Epidemiol 17:66-73.

Cohen J (1968) Weighted kappa: Nominal scale agreement provision for scaled disagreement or partial credit. Psychological bulletin 70:213.

Cole GR, Hine T (1992) Computation of cone contrasts for color vision research. Behavior Research Methods, Instruments, & Computers 24:22-27.

Coppola D, Purves D (1996) The extraordinarily rapid disappearance of entopic images. Proc Natl Acad Sci U S A 93:8001-8004.

Crook JD, Manookin MB, Packer OS, Dacey DM (2011) Horizontal cell feedback without cone type-selective inhibition mediates "red-green" color opponency in midget ganglion cells of the primate retina. The Journal of neuroscience : the official journal of the Society for Neuroscience 31:1762-1772.

Curcio CA, Allen KA (1990) Topography of ganglion cells in human retina. The Journal of comparative neurology 300:5-25.

Curcio CA, Medeiros NE, Millican CL (1996) Photoreceptor loss in age-related macular degeneration. Invest Ophthalmol Vis Sci 37:1236-1249.

Curcio CA, Sloan KR, Kalina RE, Hendrickson AE (1990) Human photoreceptor topography. The Journal of comparative neurology 292:497-523.

Curcio CA, Allen KA, Sloan KR, Lerea CL, Hurley JB, Klock IB, Milam AH (1991) Distribution and morphology of human cone photoreceptors stained with anti-blue opsin. The Journal of comparative neurology 312:610-624.

Dacey DM (1993) The mosaic of midget ganglion cells in the human retina. The Journal of neuroscience : the official journal of the Society for Neuroscience 13:5334-5355.

Dacey DM, Petersen MR (1992) Dendritic field size and morphology of midget and parasol ganglion cells of the human retina. Proc Natl Acad Sci U S A 89:9666-9670.

Dacey DM, Lee BB (1994) The 'blue-on' opponent pathway in primate retina originates from a distinct bistratified ganglion cell type. Nature 367:731-735.

Dacey DM, Packer OS (2003) Colour coding in the primate retina: diverse cell types and cone-specific circuitry. Curr Opin Neurobiol 13:421-427.

Dacey DM, Diller LC, Verweij J, Williams DR (2000) Physiology of L- and M-cone inputs to H1 horizontal cells in the primate retina. J Opt Soc Am A Opt Image Sci Vis 17:589-596.

Dacey DM, Lee BB, Stafford DK, Pokorny J, Smith VC (1996) Horizontal cells of the primate retina: cone specificity without spectral opponency. Science 271:656-659.

De Monasterio FM, Gouras P (1975) Functional properties of ganglion cells of the rhesus monkey retina. J Physiol 251:167-195.

de Monasterio FM, McCrane EP, Newlander JK, Schein SJ (1985) Density profile of blue-sensitive cones along the horizontal meridian of macaque retina. Invest Ophthalmol Vis Sci 26:289-302.

De Valois RL, De Valois KK (1993) A multi-stage color model. Vision Res 33:1053-1065.

De Valois RL, Abramov I, Jacobs GH (1966) Analysis of response patterns of LGN cells. Journal of the Optical Society of America 56:966-977.

De Vries H (1946) Luminosity curve of trichromats. Nature 157:736.

De Vries H (1949) The heredity of the relative numbers of red and green receptors in the human eye. Genetica 24:199-212.

Derrington AM, Krauskopf J, Lennie P (1984) Chromatic mechanisms in lateral geniculate nucleus of macaque. J Physiol 357:241-265.

DeVries SH, Qi X, Smith R, Makous W, Sterling P (2002) Electrical coupling between mammalian cones. Curr Biol 12:1900-1907.

Ditchburn RW, Ginsborg BL (1952) Vision with a stabilized retinal image. Nature 170:36-37.

Drasdo N, Millican CL, Katholi CR, Curcio CA (2007) The length of Henle fibers in the human retina and a model of ganglion receptive field density in the visual field. Vision Res 47:2901-2911.

Dreher AW, Bille JF, Weinreb RN (1989) Active optical depth resolution improvement of the laser tomographic scanner. Applied optics 28:804-808.

Dubis AM, Cooper RF, Aboshiha J, Langlo C, Sundaram V, Liu B, Collison F, Fishman GA, Moore AT, Webster AR, Dubra A, Carroll J, Michaelides M (2014) Genotype-Dependent Variability in Residual Cone Structure in Achromatopsia: Towards Developing Metrics for Assessing Cone Health. Invest Ophthalmol Vis Sci.

Dubra A, Sulai Y (2011) Reflective afocal broadband adaptive optics scanning ophthalmoscope. Biomedical optics express 2:1757-1768.

Dubra A, Sulai Y, Norris JL, Cooper RF, Dubis AM, Williams DR, Carroll J (2011) Noninvasive imaging of the human rod photoreceptor mosaic using a confocal adaptive optics scanning ophthalmoscope. Biomedical optics express 2:1864-1876.

Duncan JL, Zhang Y, Gandhi J, Nakanishi C, Othman M, Branham KE, Swaroop A, Roorda A (2007) High-resolution imaging with adaptive optics in patients with inherited retinal degeneration. Invest Ophthalmol Vis Sci 48:3283-3291.

Duncan JL, Talcott KE, Ratnam K, Sundquist SM, Lucero AS, Day S, Zhang Y, Roorda A (2011a) Cone structure in retinal degeneration associated with mutations in the peripherin/RDS gene. Invest Ophthalmol Vis Sci 52:1557-1566.

Duncan JL, Ratnam K, Birch DG, Sundquist SM, Lucero AS, Zhang Y, Meltzer M, Smaoui N, Roorda A (2011b) Abnormal Cone Structure in Foveal Schisis Cavities in X-Linked Retinoschisis from Mutations in Exon 6 of the RS1 Gene. Invest Ophthalmol Vis Sci 52:9614-9623.

Dunn FA, Lankheet MJ, Rieke F (2007) Light adaptation in cone vision involves switching between receptor and post-receptor sites. Nature 449:603-606.

Enoch JM (1961) Wave-guide modes in retinal receptors. Science 133:1353-1354.

Enoch JM, Hope GM (1973) Interferometric resolution determinations in the fovea and parafovea. Documenta ophthalmologica Advances in ophthalmology 34:143-156.

Enoch JM, Le D-A (2004) Comparison of the Canon CPP-1 and the New Nidek MP-1 45 Degree Fundus Camera Perimeters: Studies Around and On Top of the Optic Nerve Head in Myopia. Invest Ophthalmol Vis Sci 45:2772-.

Enoch JM, Tobey FL, Bedell HE (1981) Vertebrate photoreceptor optics.

Evans JN (1927) A Contribution to the Study of Angioscotometry. Br J Ophthalmol 11:369-384.

Field GD, Gauthier JL, Sher A, Greschner M, Machado TA, Jepson LH, Shlens J, Gunning DE, Mathieson K, Dabrowski W, Paninski L, Litke AM, Chichilnisky EJ (2010) Functional connectivity in the retina at the resolution of photoreceptors. Nature 467:673-677.

Finger RP, Charbel Issa P, Fimmers R, Holz FG, Rubin GS, Scholl HP (2009) Reading performance is reduced by parafoveal scotomas in patients with macular telangiectasia type 2. Invest Ophthalmol Vis Sci 50:1366-1370.

Fishman GA, Bozbeyoglu S, Massof RW, Kimberling W (2007) Natural course of visual field loss in patients with Type 2 Usher syndrome. Retina 27:601-608.

Flamant F (1955) Étude de la répartition de lumière dans l'image rétinienne d'une fente. Rev Opt 34:433-459.

Franssen L, Tabernero J, Coppens JE, van den Berg TJ (2007) Pupil size and retinal straylight in the normal eye. Invest Ophthalmol Vis Sci 48:2375-2382.

Franze K, Grosche J, Skatchkov SN, Schinkinger S, Foja C, Schild D, Uckermann O, Travis K, Reichenbach A, Guck J (2007) Muller cells are living optical fibers in the vertebrate retina. Proc Natl Acad Sci U S A 104:8287-8292.

Frome FS, MacLeod DI, Buck SL, Williams DR (1981) Large loss of visual sensitivity to flashed peripheral targets. Vision Res 21:1323-1328.

Gass JD, Oyakawa RT (1982) Idiopathic juxtafoveolar retinal telangiectasis. Archives of ophthalmology 100:769-780.

Gass JD, Blodi BA (1993) Idiopathic juxtafoveolar retinal telangiectasis. Update of classification and follow-up study. Ophthalmology 100:1536-1546.

Geller AM, Sieving PA (1993) Assessment of foveal cone photoreceptors in Stargardt's macular dystrophy using a small dot detection task. Vision Res 33:1509-1524.

Geller AM, Sieving PA, Green DG (1992) Effect on grating identification of sampling with degenerate arrays. J Opt Soc Am A 9:472-477.

Gilpin LB, Stewart WC, Hunt HH, Broom CD (1990) Threshold variability using different Goldmann stimulus sizes. Acta ophthalmologica 68:674-676.

Gouras P (1968) Identification of cone mechanisms in monkey ganglion cells. J Physiol 199:533-547.

Green DG (1970) Regional variations in the visual acuity for interference fringes on the retina. J Physiol 207:351-356.

Grieve K, Tiruveedhula P, Zhang Y, Roorda A (2006) Multi-wavelength imaging with the adaptive optics scanning laser Ophthalmoscope. Optics express 14:12230-12242.

Gubisch RW (1967) Optical Performance of Human Eye. Journal of the Optical Society of America 57:407-&.

Guizar-Sicairos M, Thurman ST, Fienup JR (2008) Efficient subpixel image registration algorithms. Optics letters 33:156-158.

Hardy JW, Lefebvre JE, Koliopoulos CL (1977) Real-Time Atmospheric Compensation. Journal of the Optical Society of America 67:360-369.

Harmening WM, Tiruveedhula P, Roorda A, Sincich LC (2012) Measurement and correction of transverse chromatic offsets for multi-wavelength retinal microscopy in the living eye. Biomedical optics express 3:2066-2077.

Harmening WM, Tuten WS, Roorda A, Sincich LC (2014) Mapping the perceptual grain of the human retina. The Journal of neuroscience : the official journal of the Society for Neuroscience 34:5667-5677.

Hartline HK, Ratliff F (1957) Inhibitory interaction of receptor units in the eye of Limulus. The Journal of general physiology 40:357-376.

Hartmann KI, Bartsch D-UG, Cheng L, Kim JS, Gomez ML, Klein H, Freeman WR (2011) Scanning laser ophthalmoscope imaging stabilized microperimetry in dry age-related macular degeneration. Retina 31:1323-1331.

Hartong DT, Berson EL, Dryja TP (2006) Retinitis pigmentosa. Lancet 368:1795-1809.

Hartridge H (1918) Chromatic aberration and resolving power of the eye. J Physiol 52:175-246.

He JC, Marcos S, Webb RH, Burns SA (1998) Measurement of the wave-front aberration of the eye by a fast psychophysical procedure. J Opt Soc Am A Opt Image Sci Vis 15:2449-2456.

Hecht S, Mintz EU (1939) The Visibility of Single Lines at Various Illuminations and the Retinal Basis of Visual Resolution. The Journal of general physiology 22:593-612.

Helmholtz Hv (1924) Helmholtz's treatise on physiological optics. Rochester, N.Y.: The Optical Society of America.

Hendry SH, Reid RC (2000) The koniocellular pathway in primate vision. Annu Rev Neurosci 23:127-153.

Hirsch J, Curcio CA (1989) The spatial resolution capacity of human foveal retina. Vision Res 29:1095-1101.

Hoang QV, Linsenmeier RA, Chung CK, Curcio CA (2002) Photoreceptor inner segments in monkey and human retina: mitochondrial density, optics, and regional variation. Vis Neurosci 19:395-407.

Hofer H, Singer B, Williams DR (2005a) Different sensations from cones with the same photopigment. J Vis 5:444-454.

Hofer H, Artal P, Singer B, Aragon JL, Williams DR (2001) Dynamics of the eye's wave aberration. J Opt Soc Am A Opt Image Sci Vis 18:497-506.

Hofer H, Carroll J, Neitz J, Neitz M, Williams DR (2005b) Organization of the human trichromatic cone mosaic. The Journal of neuroscience : the official journal of the Society for Neuroscience 25:9669-9679.

Holopigian K, Greenstein V, Seiple W, Carr RE (1996) Rates of change differ among measures of visual function in patients with retinitis pigmentosa. Ophthalmology 103:398-405.

Hood DC, Lazow MA, Locke KG, Greenstein VC, Birch DG (2011a) The transition zone between healthy and diseased retina in patients with retinitis pigmentosa. Invest Ophthalmol Vis Sci 52:101-108.

Hood DC, Lin CE, Lazow MA, Locke KG, Zhang X, Birch DG (2009) Thickness of receptor and post-receptor retinal layers in patients with retinitis pigmentosa measured with frequency-domain optical coherence tomography. Invest Ophthalmol Vis Sci 50:2328-2336.

Hood DC, Zhang X, Ramachandran R, Talamini CL, Raza A, Greenberg JP, Sherman J, Tsang SH, Birch DG (2011b) The inner segment/outer segment border seen on optical coherence tomography is less intense in patients with diminished cone function. Invest Ophthalmol Vis Sci 52:9703-9709.

Hornstein EP, Verweij J, Schnapf JL (2004) Electrical coupling between red and green cones in primate retina. Nature neuroscience 7:745-750.

Howland HC, Howland B (1977) A subjective method for the measurement of monochromatic aberrations of the eye. Journal of the Optical Society of America 67:1508-1518.

Hubel DH, Wiesel TN (1960) Receptive fields of optic nerve fibres in the spider monkey. J Physiol 154:572-580.

Hurvich LM, Jameson D (1957) An opponent-process theory of color vision. Psychological review 64, Part 1:384-404.

Ilardi V (2004) Renaissance vision from spectacles to telescopes. In: Frontiers in Optics, p FWW7: Optical Society of America.

Inui T, Mimura O, Kani K (1981) Retinal sensitivity and spatial summation in the foveal and parafoveal regions. Journal of the Optical Society of America 71:151-163.

Jacobson SG, Cideciyan AV (2010) Treatment possibilities for retinitis pigmentosa. The New England journal of medicine 363:1669-1671.

Jager RD, Mieler WF, Miller JW (2008) Age-related macular degeneration. N Engl J Med 358:2606-2617.

King-Smith PE, Carden D (1976) Luminance and opponent-color contributions to visual detection and adaptation and to temporal and spatial integration. Journal of the Optical Society of America 66:709-717.

King-Smith PE, Grigsby SS, Vingrys AJ, Benes SC, Supowit A (1994) Efficient and unbiased modifications of the QUEST threshold method: theory, simulations, experimental evaluation and practical implementation. Vision Res 34:885-912.

Klein R, Blodi BA, Meuer SM, Myers CE, Chew EY, Klein BE (2010) The prevalence of macular telangiectasia type 2 in the Beaver Dam eye study. Am J Ophthalmol 150:55-62 e52.

Krauskopf J (1962) Light Distribution in Human Retinal Images. Journal of the Optical Society of America 52:1046-&.

Krauskopf J, Williams DR, Heeley DW (1982) Cardinal directions of color space. Vision Res 22:1123-1131.

Labin AM, Safuri SK, Ribak EN, Perlman I (2014) Muller cells separate between wavelengths to improve day vision with minimal effect upon night vision. Nat Commun 5:4319.

Lamb TD, Simon EJ (1976) The relation between intercellular coupling and electrical noise in turtle photoreceptors. J Physiol 263:257-286.

Larsen JS (1971) The sagittal growth of the eye. II. Ultrasonic measurement of the axial diameter of the lens and the anterior segment from birth to puberty. Acta ophthalmologica 49:427-440.

Lee BB, Martin PR, Valberg A (1988) The physiological basis of heterochromatic flicker photometry demonstrated in the ganglion cells of the macaque retina. J Physiol 404:323-347.

Lee BB, Dacey DM, Smith VC, Pokorny J (2003) Dynamics of sensitivity regulation in primate outer retina: the horizontal cell network. J Vis 3:513-526.

Lennie P, Haake PW, Williams DR (1991) The design of chromatically opponent receptive fields. Computational models of visual processing:71-82.

Li KY, Roorda A (2007) Automated identification of cone photoreceptors in adaptive optics retinal images. J Opt Soc Am A Opt Image Sci Vis 24:1358-1363.

Li PH, Field GD, Greschner M, Ahn D, Gunning DE, Mathieson K, Sher A, Litke AM, Chichilnisky EJ (2014) Retinal representation of the elementary visual signal. Neuron 81:130-139.

Liang J, Williams DR (1997) Aberrations and retinal image quality of the normal human eye. J Opt Soc Am A Opt Image Sci Vis 14:2873-2883.

Liang J, Williams DR, Miller DT (1997) Supernormal vision and high-resolution retinal imaging through adaptive optics. J Opt Soc Am A Opt Image Sci Vis 14:2884-2892.

Liang J, Grimm B, Goelz S, Bille JF (1994) Objective measurement of wave aberrations of the human eye with the use of a Hartmann-Shack wave-front sensor. J Opt Soc Am A Opt Image Sci Vis 11:1949-1957.

Lie I (1980) Visual detection and resolution as a function of retinal locus. Vision Res 20:967-974.

Lim LS, Mitchell P, Seddon JM, Holz FG, Wong TY (2012) Age-related macular degeneration. Lancet 379:1728-1738.

MacLeod DI, Williams DR, Makous W (1992) A visual nonlinearity fed by single cones. Vision Res 32:347-363.

Mainster MA, Timberlake GT, Webb RH, Hughes GW (1982) Scanning laser ophthalmoscopy. Clinical applications. Ophthalmology 89:852-857.

Makiyama Y, Ooto S, Hangai M, Takayama K, Uji A, Oishi A, Ogino K, Nakagawa S, Yoshimura N (2013) Macular cone abnormalities in retinitis pigmentosa with preserved central vision using adaptive optics scanning laser ophthalmoscopy. PLoS One 8:e79447.

Makous W, Carroll J, Wolfing JI, Lin J, Christie N, Williams DR (2006) Retinal microscotomas revealed with adaptive-optics microflashes. Invest Ophthalmol Vis Sci 47:4160-4167.

Mangel SC (1991) Analysis of the horizontal cell contribution to the receptive field surround of ganglion cells in the rabbit retina. J Physiol 442:211-234.

Marchand EW (1964) Derivation of the Point Spread Function from the Line Spread Function. Journal of the Optical Society of America 54:915-919.

Martinez-Conde S, Macknik SL, Hubel DH (2004) The role of fixational eye movements in visual perception. Nat Rev Neurosci 5:229-240.

McAllister JT, Dubis AM, Tait DM, Ostler S, Rha J, Stepien KE, Summers CG, Carroll J (2010) Arrested development: high-resolution imaging of foveal morphology in albinism. Vision Res 50:810-817.

McMahon MJ, Packer OS, Dacey DM (2004) The classical receptive field surround of primate parasol ganglion cells is mediated primarily by a non-GABAergic pathway. The Journal of neuroscience 24:3736-3745.

Mendes HF, van der Spuy J, Chapple JP, Cheetham ME (2005) Mechanisms of cell death in rhodopsin retinitis pigmentosa: implications for therapy. Trends Mol Med 11:177-185.

Merigan WH, Maunsell JH (1993) How parallel are the primate visual pathways? Annu Rev Neurosci 16:369-402.

Merigan WH, Katz LM, Maunsell JH (1991) The effects of parvocellular lateral geniculate lesions on the acuity and contrast sensitivity of macaque monkeys. The Journal of neuroscience : the official journal of the Society for Neuroscience 11:994-1001.

Merino D, Duncan JL, Tiruveedhula P, Roorda A (2011) Observation of cone and rod photoreceptors in normal subjects and patients using a new generation adaptive optics scanning laser ophthalmoscope. Biomedical optics express 2:2189-2201.

Midena E (2007) Perimetry and the fundus : an introduction to microperimetry. Thorofare, NJ: SLACK Inc.

Midena E, Vujosevic S, Cavarzeran F, Microperimetry Study G (2010) Normal values for fundus perimetry with the microperimeter MP1. Ophthalmology 117:1571-1576, 1576 e1571.

Midena E, Vujosevic S, Convento E, Cavarzeran F, Pilotto E (2007) Microperimetry and fundus autofluorescence in patients with early age-related macular degeneration. British Journal of Ophthalmology 91:1499-1503.

Miller WH, Bernard GD (1983) Averaging over the foveal receptor aperture curtails aliasing. Vision Res 23:1365-1369.

Mitamura Y, Mitamura-Aizawa S, Katome T, Naito T, Hagiwara A, Kumagai K, Yamamoto S (2013) Photoreceptor impairment and restoration on optical coherence tomographic image. J Ophthalmol 2013:518170.

Mollon JD, Bowmaker JK (1992) The spatial arrangement of cones in the primate fovea. Nature 360:677-679.

Mrejen S, Sato T, Curcio CA, Spaide RF (2014) Assessing the cone photoreceptor mosaic in eyes with pseudodrusen and soft drusen in vivo using adaptive optics imaging. Ophthalmology 121:545-551.

Nathans J, Thomas D, Hogness DS (1986) Molecular genetics of human color vision: the genes encoding blue, green, and red pigments. Science 232:193-202.

Navarro R, Moreno E, Dorronsoro C (1998) Monochromatic aberrations and point-spread functions of the human eye across the visual field. J Opt Soc Am A Opt Image Sci Vis 15:2522-2529.

Neitz J, Neitz M (2011) The genetics of normal and defective color vision. Vision Res 51:633-651.

Neitz J, Carroll J, Yamauchi Y, Neitz M, Williams DR (2002) Color perception is mediated by a plastic neural mechanism that is adjustable in adults. Neuron 35:783-792.

Normann RA, Perlman I (1979) The effects of background illumination on the photoresponses of red and green cones. J Physiol 286:491-507.

Okada K, Yamamoto S, Mizunoya S, Hoshino A, Arai M, Takatsuna Y (2006) Correlation of retinal sensitivity measured with fundus-related microperimetry to visual acuity and retinal thickness in eyes with diabetic macular edema. Eye 20:805-809.

Ooka E, Mitamura Y, Baba T, Kitahashi M, Oshitari T, Yamamoto S (2011) Foveal microstructure on spectral-domain optical coherence tomographic images and visual function after macular hole surgery. Am J Ophthalmol 152:283-290 e281.

Ooto S, Hangai M, Takayama K, Arakawa N, Tsujikawa A, Koizumi H, Oshima S, Yoshimura N (2011) High-resolution photoreceptor imaging in idiopathic macular telangiectasia type 2 using adaptive optics scanning laser ophthalmoscopy. Invest Ophthalmol Vis Sci 52:5541-5550.

Ooto S, Hangai M, Takayama K, Ueda-Arakawa N, Tsujikawa A, Yamashiro K, Oishi A, Hanebuchi M, Yoshimura N (2013) Comparison of cone pathologic changes in idiopathic macular telangiectasia types 1 and 2 using adaptive optics scanning laser ophthalmoscopy. Am J Ophthalmol 155:1045-1057 e1044.

Otake S, Cicerone CM (2000) L and M cone relative numerosity and red-green opponency from fovea to midperiphery in the human retina. J Opt Soc Am A Opt Image Sci Vis 17:615-627.

Owsley C, Jackson GR, Cideciyan AV, Huang Y, Fine SL, Ho AC, Maguire MG, Lolley V, Jacobson SG (2000) Psychophysical evidence for rod vulnerability in age-related macular degeneration. Invest Ophthalmol Vis Sci 41:267-273.

Packer OS, Verweij J, Li PH, Schnapf JL, Dacey DM (2010) Blue-yellow opponency in primate S cone photoreceptors. The Journal of neuroscience : the official journal of the Society for Neuroscience 30:568-572.

Pallikaris A, Williams DR, Hofer H (2003) The reflectance of single cones in the living human eye. Invest Ophthalmol Vis Sci 44:4580-4592.

Parker AJ, Newsome WT (1998) Sense and the single neuron: probing the physiology of perception. Annu Rev Neurosci 21:227-277.

Pelli DG (1985) Uncertainty explains many aspects of visual contrast detection and discrimination. J Opt Soc Am A 2:1508-1532.

Poonja S, Patel S, Henry L, Roorda A (2005) Dynamic visual stimulus presentation in an adaptive optics scanning laser ophthalmoscope. Journal of refractive surgery 21:S575-580.

Porter J, Guirao A, Cox IG, Williams DR (2001) Monochromatic aberrations of the human eye in a large population. J Opt Soc Am A Opt Image Sci Vis 18:1793-1803.

Powner MB, Gillies MC, Zhu M, Vevis K, Hunyor AP, Fruttiger M (2013) Loss of Muller's cells and photoreceptors in macular telangiectasia type 2. Ophthalmology 120:2344-2352.

Prins N (2013) Kingdom, FAA (2009). Palamedes: Matlab routines for analyzing psychophysical data. See http://www.palamedestoolbox.org.

Pugh EN, Jr., Mollon JD (1979) A theory of the pi1 and pi3 color mechanisms of Stiles. Vision Res 19:293-312.

Purpura K, Tranchina D, Kaplan E, Shapley RM (1990) Light adaptation in the primate retina: analysis of changes in gain and dynamics of monkey retinal ganglion cells. Vis Neurosci 4:75-93.

Rangaswamy NV, Patel HM, Locke KG, Hood DC, Birch DG (2010) A comparison of visual field sensitivity to photoreceptor thickness in retinitis pigmentosa. Invest Ophthalmol Vis Sci 51:4213-4219.

Regan D, Tyler C (1971) Temporal summation and its limit for wavelength changes: An analog of Bloch's law for color vision. JOSA 61:1414-1421.

Reid RC, Shapley RM (1992) Spatial structure of cone inputs to receptive fields in primate lateral geniculate nucleus. Nature 356:716-718.

Remky A, Beausencourt E, Elsner AE (1996) Angioscotometry with the scanning laser ophthalmoscope. Comparison of the effect of different wavelengths. Invest Ophthalmol Vis Sci 37:2350-2355.

Rha J, Jonnal RS, Thorn KE, Qu J, Zhang Y, Miller DT (2006) Adaptive optics flood-illumination camera for high speed retinal imaging. Optics express 14:4552-4569.

Riggs LA, Ratliff F, Cornsweet JC, Cornsweet TN (1953) The disappearance of steadily fixated visual test objects. Journal of the Optical Society of America 43:495-501.

Rodieck R (1991a) Which cells code for color? In: From pigments to perception, pp 83-93: Springer.

Rodieck RW (1991b) The density recovery profile: a method for the analysis of points in the plane applicable to retinal studies. Vis Neurosci 6:95-111.

Rolfs M (2009) Microsaccades: Small steps on a long way. Vision Res 49:2415-2441.

Roorda A (2010) Applications of adaptive optics scanning laser ophthalmoscopy. Optometry and vision science : official publication of the American Academy of Optometry 87:260-268.

Roorda A (2011) Adaptive optics for studying visual function: a comprehensive review. J Vis 11.

Roorda A, Williams DR (1999) The arrangement of the three cone classes in the living human eye. Nature 397:520-522.

Roorda A, Williams DR (2002) Optical fiber properties of individual human cones. J Vis 2:404-412.

Roorda A, Zhang Y, Duncan JL (2007) High-resolution in vivo imaging of the RPE mosaic in eyes with retinal disease. Invest Ophthalmol Vis Sci 48:2297-2303.

Roorda A, Metha AB, Lennie P, Williams DR (2001) Packing arrangement of the three cone classes in primate retina. Vision Res 41:1291-1306.

Roorda A, Romero-Borja F, Donnelly Iii W, Queener H, Hebert T, Campbell M (2002) Adaptive optics scanning laser ophthalmoscopy. Optics express 10:405-412.

Rossi EA, Roorda A (2010) The relationship between visual resolution and cone spacing in the human fovea. Nature neuroscience 13:156-157.

Rossi EA, Weiser P, Tarrant J, Roorda A (2007) Visual performance in emmetropia and low myopia after correction of high-order aberrations. J Vis 7:14.

Rubin ML (1986) Spectacles: past, present, and future. Surv Ophthalmol 30:321-327.

Rushton WA, Baker HD (1964) Red--green sensitivity in normal vision. Vision Res 4:75-85.

Rushton WAH, Henry GH (1968) Bleaching and regeneration of cone pigments in man. Vision Res 8:617-631.

Sallo FB, Peto T, Egan C, Wolf-Schnurrbusch UE, Clemons TE, Gillies MC, Pauleikhoff D, Rubin GS, Chew EY, Bird AC (2012) The IS/OS junction layer in the natural history of type 2 idiopathic macular telangiectasia. Invest Ophthalmol Vis Sci 53:7889-7895.

Schiefer U, Benda N, Dietrich TJ, Selig B, Hofmann C, Schiller J (1999) Angioscotoma detection with fundus-oriented perimetry: A study with dark and bright stimuli of different sizes. Vision Res 39:1897-1909.

Schmidt BP, Neitz M, Neitz J (2014) Neurobiological hypothesis of color appearance and hue perception. J Opt Soc Am A Opt Image Sci Vis 31:A195-207.

Schmitz-Valckenberg S, Bultmann S, Dreyhaupt J, Bindewald A, Holz FG, Rohrschneider K (2004) Fundus autofluorescence and fundus perimetry in the junctional zone of geographic atrophy in patients with age-related macular degeneration. Invest Ophthalmol Vis Sci 45:4470-4476.

Schnapf JL, Kraft TW, Baylor DA (1987) Spectral sensitivity of human cone photoreceptors. Nature 325:439-441.

Schnapf JL, Nunn BJ, Meister M, Baylor DA (1990) Visual transduction in cones of the monkey Macaca fascicularis. J Physiol 427:681-713.

Scoles D, Sulai YN, Langlo CS, Fishman GA, Curcio CA, Carroll J, Dubra A (2014) In vivo imaging of human cone photoreceptor inner segments. Invest Ophthalmol Vis Sci 55:4244-4251.

Shack RV, Platt B (1971) Production and use of a lenticular Hartmann screen. In: J Opt Soc Am, pp 656-&: AMER INST PHYSICS CIRCULATION FULFILLMENT DIV, 500 SUNNYSIDE BLVD, WOODBURY, NY 11797-2999.

Shapley R, Enroth-Cugell C (1984) Visual adaptation and retinal gain controls. Progress in retinal research 3:263-346.

Shlaer S (1937) The Relation between Visual Acuity and Illumination. The Journal of general physiology 21:165-188.

Sincich LC, Zhang Y, Tiruveedhula P, Horton JC, Roorda A (2009) Resolving single cone inputs to visual receptive fields. Nature neuroscience 12:967-969.

Sjaarda RN, Frank DA, Glaser BM, Thompson JT, Murphy RP (1993) Assessment of vision in idiopathic macular holes with macular microperimetry using the scanning laser ophthalmoscope. Ophthalmology 100:1513-1518.

Smallman HS, MacLeod DI, He S, Kentridge RW (1996) Fine grain of the neural representation of human spatial vision. The Journal of neuroscience : the official journal of the Society for Neuroscience 16:1852-1859.

Smith VC, Pokorny J (1975) Spectral sensitivity of the foveal cone photopigments between 400 and 500 nm. Vision Res 15:161-171.

Smith VC, Pokorny J, Diddie KR (1988) Color matching and the Stiles-Crawford effect in observers with early age-related macular changes. J Opt Soc Am A 5:2113-2121.

Smith VC, Pokorny J, Lee BB, Dacey DM (2001) Primate horizontal cell dynamics: an analysis of sensitivity regulation in the outer retina. J Neurophysiol 85:545-558.

Snodderly DM, Weinhaus RS, Choi JC (1992) Neural-vascular relationships in central retina of macaque monkeys (Macaca fascicularis). The Journal of neuroscience : the official journal of the Society for Neuroscience 12:1169-1193.

Staurenghi G, Sadda S, Chakravarthy U, Spaide RF (2014) Proposed lexicon for anatomic landmarks in normal posterior segment spectral-domain optical coherence tomography: the IN*OCT consensus. Ophthalmology 121:1572-1578.

Stevenson SB, Roorda A (2005) Correcting for miniature eye movements in high resolution scanning laser ophthalmoscopy. In: Biomedical Optics 2005, pp 145-151: International Society for Optics and Photonics.

Stiles WS (1949) Increment thresholds and the mechanisms of colour vision. Documenta ophthalmologica Advances in ophthalmology 3:138-165.

Stiles WS (1959) Color vision: the approach through increment-threshold sensitivity. Proc Natl Acad Sci U S A 45:100.

Stiles WS, Crawford BH (1933) The luminous efficiency of rays entering the eye pupil at different points. P R Soc Lond B-Conta 112:428-450.

Stockman A, Sharpe LT (2000) The spectral sensitivities of the middle- and long-wavelength-sensitive cones derived from measurements in observers of known genotype. Vision Res 40:1711-1737.

Stockman A, MacLeod DI, Johnson NE (1993a) Spectral sensitivities of the human cones. J Opt Soc Am A Opt Image Sci Vis 10:2491-2521.

Stockman A, MacLeod DI, Vivien JA (1993b) Isolation of the middle-and long-wavelength-sensitive cones in normal trichromats. JOSA A 10:2471-2490.

Stromeyer CF, 3rd, Cole GR, Kronauer RE (1985) Second-site adaptation in the red-green chromatic pathways. Vision Res 25:219-237.

Sundaram V, Wilde C, Aboshiha J, Cowing J, Han C, Langlo CS, Chana R, Davidson AE, Sergouniotis PI, Bainbridge JW, Ali RR, Dubra A, Rubin G, Webster AR, Moore AT, Nardini M, Carroll J, Michaelides M (2014) Retinal structure and function in achromatopsia: implications for gene therapy. Ophthalmology 121:234-245.

Sunness JS, Schuchard RA, Shen N, Rubin GS, Dagnelie G, Haselwood DM (1995) Landmark-driven fundus perimetry using the scanning laser ophthalmoscope. Invest Ophthalmol Vis Sci 36:1863-1874.

Takamine Y, Shiraki K, Moriwaki M, Yasunari T, Miki T (1998) Retinal sensitivity measurement over drusen using scanning laser ophthalmoscope microperimetry. Graefe's archive for clinical and experimental ophthalmology = Albrecht von Graefes Archiv fur klinische und experimentelle Ophthalmologie 236:285-290.

Talcott KE, Ratnam K, Sundquist SM, Lucero AS, Lujan BJ, Tao W, Porco TC, Roorda A, Duncan JL (2011) Longitudinal study of cone photoreceptors during retinal degeneration and in response to ciliary neurotrophic factor treatment. Invest Ophthalmol Vis Sci 52:2219-2226.

Tam J, Martin JA, Roorda A (2010) Noninvasive visualization and analysis of parafoveal capillaries in humans. Invest Ophthalmol Vis Sci 51:1691-1698.

Tamura T, Nakatani K, Yau KW (1991) Calcium feedback and sensitivity regulation in primate rods. The Journal of general physiology 98:95-130.

Tessier-Lavigne M, Attwell D (1988) The effect of photoreceptor coupling and synapse nonlinearity on signal:noise ratio in early visual processing. Proc R Soc Lond B Biol Sci 234:171-197.

Thiadens AA, Somervuo V, van den Born LI, Roosing S, van Schooneveld MJ, Kuijpers RW, van Moll-Ramirez N, Cremers FP, Hoyng CB, Klaver CC (2010) Progressive loss of cones in achromatopsia: an imaging study using spectral-domain optical coherence tomography. Invest Ophthalmol Vis Sci 51:5952-5957.

Thomas MG, Kumar A, Kohl S, Proudlock FA, Gottlob I (2011) High-resolution in vivo imaging in achromatopsia. Ophthalmology 118:882-887.

Tuten WS, Tiruveedhula P, Roorda A (2012) Adaptive optics scanning laser ophthalmoscope-based microperimetry. Optometry and vision science : official publication of the American Academy of Optometry 89:563-574.

Tyler CW, Chen CC (2000) Signal detection theory in the 2AFC paradigm: attention, channel uncertainty and probability summation. Vision Res 40:3121-3144.

Valeton JM, van Norren D (1983) Light adaptation of primate cones: an analysis based on extracellular data. Vision Res 23:1539-1547.

Van den Berg T, Franssen L, Coppens J (2010) Ocular media clarity and straylight. Encyclopedia of the Eye 3:173-183.

van den Berg TJ, Franssen L, Kruijt B, Coppens JE (2013) History of ocular straylight measurement: A review. Z Med Phys 23:6-20.

van den Brink G (1962) Measurements of the geometrical aberrations of the eye. Vision Res 2:233-244.

Van Norren D, Tiemeijer LF (1986) Spectral reflectance of the human eye. Vision Res 26:313-320.

Vargas-Martin F, Prieto PM, Artal P (1998) Correction of the aberrations in the human eye with a liquid-crystal spatial light modulator: limits to performance. J Opt Soc Am A Opt Image Sci Vis 15:2552-2562.

Vingrys AJ, Pianta MJ (1999) A new look at threshold estimation algorithms for automated static perimetry. Optometry and vision science : official publication of the American Academy of Optometry 76:588-595.

Vislisel JM, Doyle CK, Johnson CA, Wall M (2011) Variability of rarebit and standard perimetry sizes I and III in normals. Optometry and vision science : official publication of the American Academy of Optometry 88:635-639.

Vitale S, Ellwein L, Cotch MF, Ferris FL, 3rd, Sperduto R (2008) Prevalence of refractive error in the United States, 1999-2004. Arch Ophthalmol 126:1111-1119.

Vogel CR, Arathorn DW, Roorda A, Parker A (2006) Retinal motion estimation in adaptive optics scanning laser ophthalmoscopy. Optics express 14:487-497.

Vohnsen B (2007) Photoreceptor waveguides and effective retinal image quality. J Opt Soc Am A Opt Image Sci Vis 24:597-607.

Vohnsen B, Rativa D (2011) Absence of an integrated Stiles–Crawford function for coherent light. J Vis 11:19.

Volbrecht VJ, Shrago EE, Schefrin BE, Werner JS (2000) Spatial summation in human cone mechanisms from 0 degrees to 20 degrees in the superior retina. J Opt Soc Am A Opt Image Sci Vis 17:641-650.

Vos JJ, Bouman MA (1964) Contribution of the Retina to Entoptic Scatter. Journal of the Optical Society of America 54:95-100.

Vos JJ, Walraven PL (1971) On the derivation of the foveal receptor primaries. Vision Res 11:799-818.

Vos JJ, Walraven J, van Meeteren A (1976) Light profiles of the foveal image of a point source. Vision Res 16:215-219.

Wald G (1945) Human Vision and the Spectrum. Science 101:653-658.

Wald G (1964) The Receptors of Human Color Vision. Science 145:1007-1016.

Walraven PL (1974) A closer look at the tritanopic convergence point. Vision Res 14:1339-1343.

Walsh G, Charman WN, Howland HC (1984) Objective technique for the determination of monochromatic aberrations of the human eye. J Opt Soc Am A 1:987-992.

Wang B, Ciuffreda KJ (2006) Depth-of-focus of the human eye: theory and clinical implications. Surv Ophthalmol 51:75-85.

Watson AB, Pelli DG (1983) QUEST: a Bayesian adaptive psychometric method. Perception & psychophysics 33:113-120.

Webb RH, Hughes GW, Pomerantzeff O (1980) Flying spot TV ophthalmoscope. Applied optics 19:2991-2997.

Webb RH, Hughes GW, Delori FC (1987) Confocal scanning laser ophthalmoscope. Applied optics 26:1492-1499.

Webb RH, Penney CM, Thompson KP (1992) Measurement of ocular local wavefront distortion with a spatially resolved refractometer. Applied optics 31:3678-3686.

Wen Y, Klein M, Hood DC, Birch DG (2012) Relationships among multifocal electroretinogram amplitude, visual field sensitivity, and SD-OCT receptor layer thicknesses in patients with retinitis pigmentosa. Invest Ophthalmol Vis Sci 53:833-840.

Wesner MF, Pokorny J, Shevell SK, Smith VC (1991) Foveal cone detection statistics in color-normals and dichromats. Vision Res 31:1021-1037.

Westheimer G (1967) Spatial interaction in human cone vision. J Physiol 190:139-154.

Westheimer G (2003) Entoptic phenomena. In: Adler's Physiology of the Eye: Clinical Application, 10th Edition (Kaufman PLA, Albert, ed), pp 441-452. St. Louis: Mosby.

Westheimer G (2006) Specifying and controlling the optical image on the human retina. Prog Retin Eye Res 25:19-42.

Westheimer G (2013) Retinal light distributions, the Stiles–Crawford effect and apodization. JOSA A 30:1417-1421.

Westheimer G, Campbell FW (1962) Light distribution in the image formed by the living human eye. Journal of the Optical Society of America 52:1040-1045.

Wiesel TN, Hubel DH (1966) Spatial and chromatic interactions in the lateral geniculate body of the rhesus monkey. J Neurophysiol 29:1115-1156.

Williams DR (2011) Imaging single cells in the living retina. Vision Res 51:1379-1396.

Williams DR, Coletta NJ (1987) Cone spacing and the visual resolution limit. J Opt Soc Am A 4:1514-1523.

Williams DR, Porter J (2006) Development of adaptive optics in vision science and ophthalmology. In: Adaptive optics for vision science: Principles, practices, design and applications (Porter J, Queener H, Lin J, Thorn K, Awwal AA, eds), pp 3-29: John Wiley & Sons.

Williams DR, MacLeod DI, Hayhoe MM (1981) Punctate sensitivity of the blue-sensitive mechanism. Vision Res 21:1357-1375.

Wilson ME (1970) Invariant features of spatial summation with changing locus in the visual field. J Physiol 207:611-622.

Wolfing JI, Chung M, Carroll J, Roorda A, Williams DR (2006) High-resolution retinal imaging of cone-rod dystrophy. Ophthalmology 113:1019 e1011.

Woods RL, Vera-Diaz FA, Lichtenstein L, Peli E (2007) Spatial Alignment of Microperimeters. Invest Ophthalmol Vis Sci 48:144-.

Wright AF, Chakarova CF, Abd El-Aziz MM, Bhattacharya SS (2010) Photoreceptor degeneration: genetic and mechanistic dissection of a complex trait. Nat Rev Genet 11:273-284.

Xiao M, Hendrickson A (2000) Spatial and temporal expression of short, long/medium, or both opsins in human fetal cones. The Journal of comparative neurology 425:545-559.

Yang Q, Arathorn DW, Tiruveedhula P, Vogel CR, Roorda A (2010) Design of an integrated hardware interface for AOSLO image capture and cone-targeted stimulus delivery. Optics express 18:17841-17858.

Yannuzzi LA, Bardal AM, Freund KB, Chen KJ, Eandi CM, Blodi B (2006) Idiopathic macular telangiectasia. Archives of ophthalmology 124:450-460.

Yeh T, Smith VC, Pokorny J (1989) The effect of background luminance on cone sensitivity functions. Invest Ophthalmol Vis Sci 30:2077-2086.

Yeh T, Lee BB, Kremers J (1996) The time course of adaptation in macaque retinal ganglion cells. Vision Res 36:913-931.

Yoon G (2006) Wavefront sensing and diagnostic uses. In: Adaptive optics for vision science: Principles, practices, design and applications (Porter J, Queener H, Lin J, Thorn K, Awwal AA, eds), pp 63-82: John Wiley & Sons.

Yoon GY, Williams DR (2002) Visual performance after correcting the monochromatic and chromatic aberrations of the eye. J Opt Soc Am A Opt Image Sci Vis 19:266-275.

Yoon MK, Roorda A, Zhang Y, Nakanishi C, Wong LJ, Zhang Q, Gillum L, Green A, Duncan JL (2009) Adaptive optics scanning laser ophthalmoscopy images in a family with the mitochondrial DNA T8993C mutation. Invest Ophthalmol Vis Sci 50:1838-1847.

Young T (1801) The Bakerian Lecture: on the mechanism of the eye. Philosophical Transactions of the Royal Society of London:23-88.

Young T (1802) The Bakerian lecture: On the theory of light and colours. Philosophical Transactions of the Royal Society of London:12-48.

Yuodelis C, Hendrickson A (1986) A qualitative and quantitative analysis of the human fovea during development. Vision Res 26:847-855.

Zayit-Soudry S, Duncan JL, Syed R, Menghini M, Roorda AJ (2013) Cone structure imaged with adaptive optics scanning laser ophthalmoscopy in eyes with nonneovascular age-related macular degeneration. Invest Ophthalmol Vis Sci 54:7498-7509.

Zhang Y, Roorda A (2006) Evaluating the lateral resolution of the adaptive optics scanning laser ophthalmoscope. Journal of biomedical optics 11:014002.

Zhang Y, Poonja S, Roorda A (2006) MEMS-based adaptive optics scanning laser ophthalmoscopy. Optics letters 31:1268-1270.

Threshold Intensity (au)	Visual Sensitivity (dB)	Stimulus Intensity (logQuanta/pixel)*
0.000	–	1.79
0.001	30	1.80
0.002	27	1.82
0.004	24	1.84
0.008	21	1.89
0.016	18	1.97
0.032	15	2.09
0.063	12	2.27
0.126	9	2.49
0.251	6	2.75
0.501	3	3.02
1.000	0	3.31

*following Chapter 2: assumes 543 nm light with an AOM leak of 0.45 nW and full stimulus power of 15 nW, both measured at 100% duty cycle (see calculations below)

Background calculation example (AOM voltage = zero):

1. Measure power at 100% duty cycle: $0.45 \text{ nW} = 4.5 \times 10^{-10} \text{ W} = 4.5 \times 10^{-10} \text{ J/sec}$

2. Convert to ergs per second: $(4.5 \times 10^{-10} \text{ J/sec}) \times (10^7 \text{ erg/J}) = 4.5 \times 10^3 \text{ erg/sec}$

3. Compute ergs per quanta for λ (543 nm): $E_{quantum} = hc/\lambda$

   where c = speed of light = 3×10^8 m/sec

   and where h = Planck's constant = 6.6261×10^{-27} erg·sec

   $E_{quantum} = [(6.6261 \times 10^{-27} \text{ erg·sec}) \times (3 \times 10^8 \text{ m/sec})]/(543 \times 10^{-9} \text{ m}) = 3.66 \times 10^{-12} \text{ erg/quanta}$

4. Convert (2) to quanta per second: $(4.5 \times 10^3 \text{ erg/sec})/(3.66 \times 10^{-12} \text{ erg/quanta})$

   $= 1.23 \times 10^9 \text{ quanta/sec}$

5. Compute quanta per pixel, Q_{pmin}: $Q_p = (1.23 \times 10^9 \text{ quanta/sec}) \times (5 \times 10^{-8} \text{ sec/pixel})$

   $= 61 \text{ quanta/pixel}$

   $= 1.79 \text{ logQuanta/pixel}$

Stimulus intensity calculation (AOM voltage = max):

1. Follow steps 1-5 above to calculate the quanta per pixel at maximum modulation, Q_{pmax}

2. Compute quanta per stimulus based on its size, duration, and modulation:

$$\mathbf{Q_{stim} = [(Q_{pmax} - Q_{pmin}) \times I_{stim} \times N_p \times t_{stim}] + Q_{pmin}}$$

where, Q_{pmax} = quanta per pixel for maximum modulation

I_{stim} = stimulus intensity, in linearized arbitrary units

N_p = number of pixels per stimulus

t_{stim} = number of frames per stimulus